A　　　　S　–N　I

S　　　　L　　Q

P　　　　　　　Y

P　　　(A　　O　　)

vorgelegt von

Wolfgang Schmitt

06. März 2007

Y   ’

’   .

Z

Die Ozeane speichern und transportieren enorme Mengen an Sonnenwärme und spielen so eine entscheidende Rolle für das Klima unseres Planeten. Indem sie überschüssige Energie aus den Tropen in höhere Breiten transportieren, tragen Meeresströmungen dazu bei die Temperaturunterschiede zwischen dem Äquator und den Polen auszugleichen. Ein großer Teil dieser Energie wird durch den sogenannten 'Ocean Conveyor Belt' (Broecker, 1991) transportiert. Dieses 'Förderband' ist ein weltumspannendes Strömungssystem, angetrieben durch thermohaline Konvektion. Veränderungen der Strömungsmuster wirken sich auf die Verteilung von Wärme aus und beeinflussen so das Klima auf verschiedenen Maßstäben von lokal bis global.

Auf Grund der Bedeutung von Meeresströmungen für das Klimageschehen ist die Rekonstruktion von Paläoströmungen seit jeher von großem Interesse für die Klimaforschung und die Paläoozeanographie. Unter den verschiedenen Werkzeugen, die zur Strömungsrekonstruktion verwendet werden, erfährt das Sm–Nd Isotopensystem zunehmende Aufmerksamkeit. Dieses System wurde erstmals durch O'Nions et al. (1978) in einem ozeanographischen Kontext angewandt. Mittlerweile ist es als Standardmethode etabliert, wie eine Fülle kürzlich erschienener Publikationen zeigt (z.B. Rutberg et al., 2000; Tütken et al., 2002; Weldeab et al., 2002; Benson et al., 2003; Farmer und Barber, 2003; Piotrowski et al., 2004; Bayon et al., 2002, 2003, 2004; Lacan und Jeandel, 2001, 2004, 2005, und viele mehr). In der Anwendung des Sm–Nd Isotopensystems auf ozeanographische und paläoozeanographische Fragestellungen können zwei Ansätze unterschieden werden.

Der erste Ansatz beruht auf den Isotopenzusammensetzungen von im Kristallgitter detritischer Minerale gebundenem Sm und Nd. Mit deren Hilfe kann die kontinentale Herkunft klastischer Sedimente bestimmt werden, um so Rückschlüsse auf Transportrichtung und -distanz zu ziehen (z.B. Revel et al., 1996; Tütken et al., 2002). Im zweiten Ansatz wird die Isotopenzusammensetzung von in Meerwasser gelöstem Nd als 'Fingerabdruck' zur Unterscheidung verschiedener Wassermassen benutzt. Diese Methode beruht auf der im Vergleich zur globalen Umwälzrate der Ozeane (ca. 1000 Jahre) kürzeren Verweildauer von gelöstem Nd in Meerwasser (500-1000 Jahre; Tachikawa et al., 2003). Dieser Umstand führt zu charakteristischen Unterschieden in den Isotopenzusammensetzungen verschiedener Wassermassen, die jeweils durch den Eintrag von gelöstem Nd gesteuert werden. Mit Hilfe dieser isotopischen Unterschiede kann die Verteilung rezenter Wassermassen bestimmt werden (z.B. Lacan und Jeandel, 2001, 2004). Zusätzlich ermöglicht diese Methode unter Verwendung geeigneten Probenmaterials die Rekonstruktion verschiedener Wasser-

massen in der Vergangenheit. Hierfür kommt theoretisch jegliches Material in Frage, dessen Nd-Gehalt sich von ehemals in Meerwasser gelöstem Nd ableitet. Verwendung finden fossile Überreste mariner Organismen (z.B. Foraminiferen; Vance und Burton, 1999; Burton und Vance, 2000), oder, vor allem für die nähere geologische Vergangenheit, Eisen-Mangan Knollen (z.B. Frank et al., 2002). Jedoch sind Eisen-Mangan Knollen nicht auf das für die Klimaforschung besonders interessante Spätquartär anwendbar. Dies liegt an deren niedrigen Wachstumsraten (mm/Ma), die eine nur unzureichende zeitliche Auflösung erlauben. Um diesen Nachteil zu umgehen, wird in den letzten Jahren verstärkt die Verwendbarkeit von in der Sedimentsäule fein verteilten Eisen-Mangan Phasen untersucht (z.B. Rutberg et al., 2000; Bayon et al., 2002, 2003, 2004; Piotrowski et al., 2004).

Im Rahmen dieser Arbeit wurden beide Ansätze, d.h. die Verwendung von im Kristallgitter detritischer Minerale gebundenem Sm und Nd, und Nd in fein verteilten, authigenen Eisen-Mangan Phasen, verfolgt. Die verwendeten Proben stammen aus einem Sedimentkern vom Yermak Plateau aus der nordöstlichen Fram Straße. Zwischen Grönland und dem Spitzbergen Archipel gelegen, stellt die Fram Straße die einzige Tiefenwasserverbindung zwischen dem Arktischen Ozean und, über die Grönland-Island-Norwegen See, dem Nordatlantik dar. Im Bereich der Grönland-Island-Norwegen See findet für die globale thermohaline Zirkulation wichtige Tiefenwasserbildung statt. Dieser Prozess befindet sich in einem empfindlichen Gleichgewicht, das vor allem durch den Salzgehalt des Oberflächenwassers bestimmt wird. Der Salzgehalt des Oberflächenwassers in dieser Region wiederum wird maßgeblich durch den Ausstrom niedrigsalinen Wassers aus dem Arktischen Ozean beeinflusst. Aus diesem Grund ist die Rekonstruktion des Wasseraustausches zwischen dem Arktischen Ozean und dem Atlantik durch die Fram Straße von großem Interesse für die Klimaforschung.

In der vorliegenden Arbeit wurde die Herkunft der im Laufe der letzten 129 000 Jahre am westlichen Yermak Plateau abgelagerten Sedimente untersucht. Hierzu wurden neben den Proben des untersuchten Sedimentkernes auch Proben aus potenziellen Liefergebieten auf ihre Sm–Nd-Isotopie hin analysiert. Nach weitverbreiteter Meinung wird unter rezenten Bedingungen Sedimentmaterial sowohl per Eisdrift aus den sibirischen Schelfgebieten, als auch durch aus dem Süden einströmendes Oberflächen- und Tiefenwasser angeliefert. Um diese unterschiedlichen Transportmechanismen und Herkunftsgebiete aufzulösen, wurde der Großteil der verwendeten Proben in die Korngrößenfraktionen Ton, Feinsilt, Grobsilt und Sand aufgetrennt.

Durch die Lage des untersuchten Sedimentkernes ist die Anlieferung von Material in Sandgröße (oder gröber) eindeutig auf Eisdrift beschränkt. Dieses eistransportierte Material (IRD) dient damit als Hinweis auf die Veränderungen der Oberflächenströmungen. Das Sedimentmaterial in Ton- bis Siltgröße hingegen liefert ein Mischsignal von Eis- und Strömungstransport (IRD und Schwebefracht). Durch Vergleich der Isotopenzusammen-

setzungen der einzelnen Proben untereinander und mit denen der potenziellen Liefergebiete, läßt sich unter Einbeziehung isotopenunabhängiger Literaturdaten (z.B. mineralogische Sedimentzusammensetzung, Korngrößenverteilung, Faunenzusammensetzung, etc.) eine Reihe von Aussagen treffen. Die verschiedenen Korngrößenfraktionen einzelner Kernproben weisen in der Regel nur geringe Unterschiede in ihrer Isotopenzusammensetzung auf (größtenteils unterhalb der analytischen Nachweisgrenze). Die größten Abweichungen zeigen die Sandfraktionen. Bis auf wenige Ausnahmen kann dies vermutlich auf den Umstand zurückgeführt werden, dass die Sandfraktionen auf Grund der geringen Probenmenge im Verhältnis zur groben Korngröße nicht repräsentativ sind.

Die generell geringen isotopischen Unterschiede deuten auf eine gemeinsame Herkunft von IRD und Schwebefracht hin. Da ein Transport von Schwebefracht von den sibirischen Schelfgebieten der Laptev- und Kara See zum Yermak Plateau ausgeschlossen werden kann, ist auch eine solche Herkunft des IRD unwahrscheinlich. Hingegen erscheint, unter rezenten interglazialen Bedingungen, eine gemeinsame Herkunft von IRD und Schwebefracht aus dem Bereich von Spitzbergen und der westlichen Barents See wahrscheinlich.

Die zeitliche Entwicklung der Isotopenkurve für den untersuchten Sedimentkern legt nahe, dass die rezenten Sedimentationsverhältnisse trotz wiederholter großräumiger Vergletscherungen der Spitzbergen-Barents See Region auch während der letzten 129 000 Jahre im Wesentlichen unverändert bestanden haben. Die größten Abweichungen von den rezenten Verhältnissen zeigen sich während der Hauptphase des letzten Glazials vor ca. 20 000 Jahren. Zu diesem Zeitpunkt wurden beträchtliche Mengen IRD durch vom Skandinavischen Eisschild stammende Eisberge bis in die Fram Straße transportiert. Darüber hinaus konnte an Hand von Schreibkreidefragmenten eine während des letzten Glazials bis in die südliche Fram Straße (Spielhagen, 1991) reichende Eisbergdrift aus der Nordsee auch für das Yermak Plateau nachgewiesen werden.

Im Rahmen des zweiten analytischen Ansatzes, d.h. der Untersuchung der Nd-Isotopie von fein verteilten Eisen-Mangan Phasen, wurde zunächst an der Umsetzung der experimentellen Methode gearbeitet. Die Methode der chemischen Extraktion der Eisen-Mangan Phasen durch ein Mischreagenz (bestehend aus Essigsäure und Hydroxylamin-Hydrochlorid) beruht im Wesentlichen auf der Arbeit von Chester und Hughes (1967). Im Laufe der Jahre wurden verschiedene auf deren Arbeit beruhende Modifikationen der Methode vorgeschlagen (Tessier et al., 1979; Chao und Zhou, 1983; Hall et al., 1996), und zuletzt durch Bayon et al. (2002) einem umfassenden Vergleich unterzogen. In Anlehnung an das von Bayon et al. (2002) beschriebene Extraktionsprotokoll (das vor allem auf die Vermeidung von Kontamination durch andere Sedimentkomponenten abzielt) wurden zunächst fünf Kernproben bearbeitet, und mit großzügiger Unterstützung der EU an der European Union Large Scale Geochemical Facility an der Universität Bristol, England, per ICP-MS auf ihre Seltenerdmuster untersucht. Zusätzlich wurde in München die Nd-Isotopie von

aus neun Proben des untersuchten Sedimentkernes extrahierten Eisen-Mangan Phasen bestimmt. Die in England bestimmten Seltenerdmuster weisen eine für Eisen-Mangan Phasen untypische Anreicherung der mittleren Seltenen Erden auf. Auch die Isotopenuntersuchungen ergaben ein ungewöhnliches Bild. Über die Zeit gesehen verlaufen die Isotopenkurven der Eisen-Mangan Phasen und der detritischen Phasen weitgehend parallel, was auf das Bestehen einer systematischen genetischen Beziehung zwischen den analysierten Nd-Fraktionen hindeutet. Eine ähnliche Beziehung scheint auch für einen in mehreren Publikationen bearbeiteten Sedimentkern aus dem südöstlichen Atlantik zu bestehen (Rutberg, 2000; Rutberg et al., 2000; Piotrowski et al., 2004).

Zur Beantwortung der aufgeworfenen Fragen bezüglich der generellen Anwendbarkeit der Methode wurde daraufhin eine Experimentreihe durchgeführt. Mehrere Aliquote ein und der selben Kernprobe wurden mit unterschiedlichen Einwirkzeiten und Konzentrationen der verwendeten Reagenzien bearbeitet und in möglichst vielen Zwischenschritten auf ihre Sm- und Nd-Isotopie analysiert. Die Ergebnisse dieser Experimentreihe weisen auf eine konzeptionelle Schwäche der Methode hin. Zur Vermeidung von Kontamination (d.h. des Herauslösens von kristallgebundenem Nd) beschränken sich alle in der Literatur beschriebenen Methoden auf eine Variation der Konzentration des zur Reduktion der Eisen-Mangan Phasen verwendeten Hydroxylamin-Hydrochlorids. Dabei wird jedoch die korrosive Wirkung der beigemischten Essigsäure außer Acht gelassen, die in allen Fällen bei $4.4 \ mol \cdot l^{-1}$ liegt. Bei den typischerweise verwendeten Einwirkzeiten ist der durch eine derartige Konzentration von Essigsäure bedingte niedrige pH-Wert ausreichend, um leicht lösliche Mineralphasen anzugreifen und kristallgebundenes Nd freizusetzen (Hannigan und Sholkovitz, 2001; Dubinin und Strekopytov, 2001). Hierbei sind vor allem phosphatische Mineralphasen in Betracht zu ziehen, was mit den oben erwähnten Anreicherungen der mittleren Seltenen Erden übereinstimmen würde. Verschiedene phosphatische Mineralphasen, z.B. Apatit, sind häufige Nebenbestandteile vieler klastischer Sedimentgesteine und können mit ihren hohen Seltenerdkonzentrationen jegliches Meerwassersignal maskieren. Dies alles deutet darauf hin dass die verwendeten Methoden zur Bestimmung der Paläomeerwasserisotopie mit Hilfe fein verteilter Eisen-Mangan Phasen noch bei weitem nicht ausgereift genug sind um standardmäßig angewendet zu werden.

S

By storing and transporting vast amounts of energy derived from solar insolation, the oceans play an important role in shaping Earth's climate. On the largest scale, ocean currents smooth the temperature gradients between the equator and the poles by redistributing excess energy from the tropics to higher latitudes. Much of this excess heat is transported by the so-called Ocean Conveyor Belt (Broecker, 1991), a global network of ocean currents driven by thermohaline convection. Changes in the pattern and strength of thermohaline circulation affect the redistribution of heat, and thereby significantly influence climate on local to global scales.

The reconstruction of paleocurrents has long been a subject of paleoceanographic research. Among the various methods employed in tracing paleocurrents (and modern currents), the Sm–Nd isotope system is experiencing ever increasing attention. First applied in an oceanographic context by O'Nions et al. (1978), it is by now established as a standard tool, as shown by numerous recent publications (e.g. Rutberg et al., 2000; Tütken et al., 2002; Weldeab et al., 2002; Benson et al., 2003; Farmer and Barber, 2003; Piotrowski et al., 2004; Bayon et al., 2002, 2003, 2004; Lacan and Jeandel, 2001, 2004, 2005, and many more). Two lines of application of the Sm–Nd isotope system to oceanography/paleoceanography can be distinguished, both of which were followed for this thesis.

The first approach uses the isotopic composition of Sm and Nd hosted in detrital minerals to infer the provenance of terrigenous sediments. This information can be used to draw conclusions about the direction and distance of sediment delivery. The second approach uses the isotopic signature of Nd as a tracer of different water masses. Due to the oceanic residence time of Nd being shorter than the global turnover rate of seawater (500-1000 years vs ~1000 years; Tachikawa et al., 2003), different bodies of water acquire distinct Nd isotopic signatures as a function of the age of adjacent continents. Apart from directly analyzing the Nd isotopic compositions of water samples to trace the modern distribution of different water masses (e.g. Lacan and Jeandel, 2001, 2004), suitable archives of seawater-derived Nd can be employed to study paleocurrents. Possible archives are fossil remains of marine organisms (e.g. foraminifers; Burton and Vance, 2000), or, most widely used for the recent geological past, Fe-Mn nodules and crusts (e.g. Frank et al., 2002). With slow growth rates on the order of mm/Ma, however, Fe-Mn nodules do not offer the high temporal resolution necessary to study Late Quaternary climate change. Attention has therefore recently turned to authigenic Fe-Mn oxyhydroxides finely dispersed throughout the sediment column (e.g. Rutberg et al., 2000; Bayon et al., 2002, 2003, 2004; Piotrowski et al., 2004).

For this thesis, both lines of application of the Sm–Nd isotope system to paleoceanography were followed. The samples were taken from a sediment core collected from the Yermak Plateau in the north-eastern Fram Strait. Situated between Greenland and the Svalbard Archipelago, the Fram Strait is the only deep connection between the Arctic Ocean and, via the Greenland-Iceland-Norwegian (Nordic) Seas, the North Atlantic. The Nordic Seas are an area of deep-water formation important for the global thermohaline circulation. There, the processes of deep-water formation are in a state of equilibrium that is most sensitive to changes in surface water salinity, which, in turn, is strongly influenced by the outflow of water of low salinity from the Arctic Ocean. This makes the history of water exchange between the Atlantic and the Arctic Ocean through the Fram Strait a subject of key interest for climate research.

In particular, it was attempted to reconstruct the provenance of sediments deposited on the western Yermak Plateau over the last 129 000 years. This was done by analyzing samples from the sediment core and from potential source areas for their Sm–Nd isotopic compositions. The current understanding is that under present interglacial conditions sediment is delivered to the Yermak Plateau by ice drift from the Siberian shelf areas (Kara- and Laptev Sea) and as suspended load of Atlantic water advected from the south. To resolve these assumed differences in provenance and transport mechanism, the majority of the samples was split into the grain-size fractions clay, fine silt, coarse silt, and sand for Sm–Nd analyses.

The position of the investigated core on the upper slope of the western Yermak Plateau limits delivery of sand-size (or coarser) material to ice rafting. The sand fractions of the core samples were therefore interpreted to be exclusively of ice rafted origin, and thus used as an indicator of changes in the pattern of surface currents. Clay- to silt-size material, on the other hand, yields a mixed signal of ice rafting and suspended-load delivery. Based on a comparison of the isotopic compositions of the core samples with those of the samples from potential source areas, a number of conclusions can be drawn: Most core sample show only little isotopic variation between their constituent size fractions (mostly less than analytical uncertainty). Only sand fractions show considerable differences. This can probably be explained by the sand samples' small sample size relative to their coarse grain size; as a result, most sand fractions probably are not representative.

The generally good agreement between the isotopic compositions suggests a common origin of ice rafted detritus (IRD) and suspended load. The possibility of suspended particulate matter transport from the Siberian shelf areas of the Kara- and Laptev Seas to the Yermak Plateau in significant amounts can be excluded. An origin of IRD in the Kara- and Laptev Sea is therefore equally unlikely. Instead, a common provenance of IRD and suspended particulate matter from the Svalbard/Barents Sea area is a plausible scenario, supported by isotope-independent data from the literature (e.g. grain-size distribution, mineralogical composition, faunal abundance, etc.).

The moderate downcore Nd isotopic variation suggests that, despite repeated large-scale glaciations in the Svalbard/Barents Sea area, the general modern-type circulation in the Fram Strait area has been active for most of the last 129 000 years. The largest deviation from modern conditions is indicated for the peak of the last glacial phase, approximately 20 000 years ago. Then, large amounts of IRD were delivered to the Yermak Plateau by icebergs calving from the Scandinavian ice sheet. Moreover, the occurrence of chalk fragments confirms iceberg drift from as far south as the North Sea. A similar finding has previously been reported for samples from the southern Fram Strait by Spielhagen (1991).

Regarding the second analytical approach, i.e. the Nd isotopic analysis of finely dispersed authigenic Fe-Mn oxyhydroxides, implementation of the experimental technique was targeted first. The method of Fe-Mn oxyhydroxide extraction by means of leaching with a mixed reagent (acetic acid and hydroxylamine-hydrochloride) largely is based on the work of Chester and Hughes (1967). Modifications of their method have been reported in Tessier et al. (1979), Chao and Zhou (1983), and Hall et al. (1996), and have recently been compared by Bayon et al. (2002). Based on the experimental protocol described by Bayon et al. (2002), five core samples were processed and analyzed for their rare earth element (REE) concentrations by ICP-MS at the European Union Large Scale Geochemical Facility at the University of Bristol, England, financed by the EU. In addition, nine core samples were processed and the leachates analyzed for their Nd isotopic composition in Munich.

The REE patterns of the leachates show an enrichment of the middle REE that is atypical for authigenic Fe-Mn phases. The isotopic analysis also yielded controversial results: downcore, the Nd isotope curves for the leachates and the detrital phases run approximately parallel, suggesting a systematic genetic relationship between the analyzed Nd fractions. A similar relationship appears to exist between data reported in Rutberg (2000), Rutberg et al. (2000), and Piotrowski et al. (2004) for a sediment core from the south-eastern Atlantic.

To answer the questions raised by these controversial results, a sequential leaching experiment was designed. Several aliquots of one core sample were treated for different durations with different concentrations of the leaching reagents, and at intermediate steps were analyzed for their Sm–Nd isotopic composition. The results of this leaching experiment point towards a conceptual weakness of the method. In order to avoid contamination by non-authigenic sediment components, all experimental methods described in the literature focus on adjusting the concentration of the hydroxylamine-hydrochloride used to reduce Fe and Mn to their soluble states. This approach, however, does not take into account the dissolution of acid-soluble phases by acetic acid, which in all cases is used at a strength of 4.4 mol·l^{-1}. Consequently, the leaching reagent is sufficiently corrosive to attack easily-soluble detrital minerals and release non-seawater-derived Nd (Hannigan and Sholkovitz, 2001; Dubinin and Strekopytov, 2001). Phosphatic phases are therefore a likely source of non-seawater-derived Nd. Apatite, for instance, is a common component of clastic sedimentary

rocks, is easily dissolved by weak acids, and can account for the middle REE enrichment in the leachates. Its high Nd concentrations would mask any seawater signal. To conclude, it appears as though the available extraction techniques are not yet sufficiently refined to reliably determine the Nd isotopic composition of finely dispersed Fe-Mn oxyhydroxides as a proxy for paleoseawater composition.

C

L   F

L   T

I

Being the largest reservoir of heat derived from solar insolation (Cronin, 1999), the oceans play an important role in shaping Earth's climate. Fundamentally, climate is driven by temperature gradients across the surface of the Earth, causing atmospheric and oceanic motion that, on the largest scale, transfers excess heat from low to high latitudes. Much of this heat is transported by the so-called Ocean Conveyor Belt (Broecker, 1991), a global network of ocean currents driven by thermohaline convection (Fig. 1). Changes in the pattern and strength of thermohaline circulation affect the redistribution of heat, and thereby significantly influence climate on local to global scales.

A key site of global thermohaline circulation is the North Atlantic, where, under present-day interglacial conditions, deep-water is formed by sinking of dense (cold and salty) water in the Greenland-Iceland-Norwegian (Nordic) Seas and in the Labrador Sea (Fig. 1). Heat delivered by the compensating northward flow of warm surface water is responsible for the mild climate of Europe. The mechanism of deep-water formation is particularly sensitive to changes in salinity. Paleoceanographic research has shown that input of large amounts of freshwater has repeatedly slowed down, or entirely interrupted, deep-water formation in the North Atlantic in the past (e.g. Rahmstorf, 2002, and references therein). Freshwater in
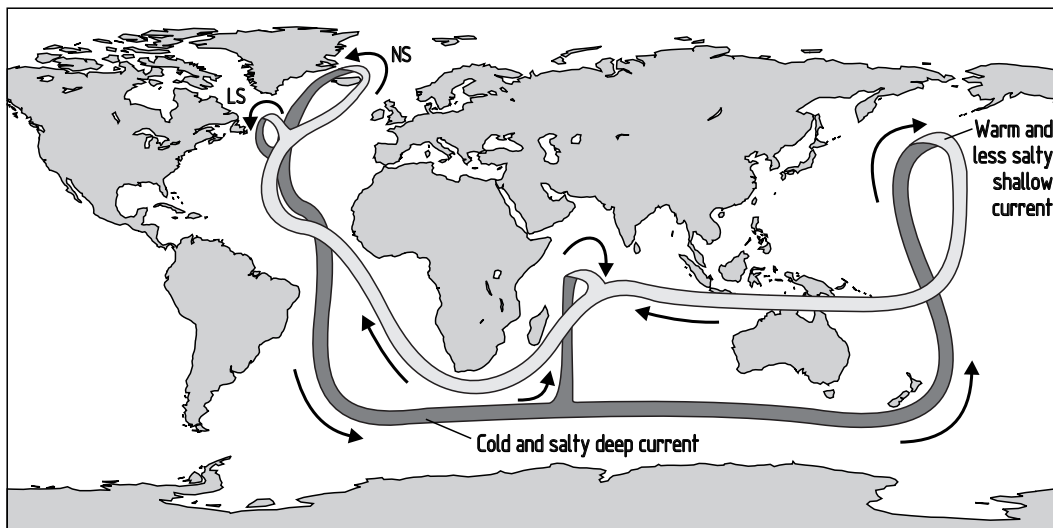
Figure 1 : Simplified illustration of the global Ocean Conveyor Belt (present-day situation). One overturn of the water masses takes about 1000 years. LS = Labrador Sea, NS = Nordic Seas. Redrawn from Alley (2000).

large quantities can be released by melting of ice sheets, by drainage of ice-dammed lakes (e.g. Svendsen et al., 2004), or large-volume discharge of rivers. In addition to controlling the freshwater budget, large ice sheets can directly influence oceanic conditions by blocking pathways of ocean currents(e.g. shelf-based ice sheets) or changing atmospheric conditions (e.g. katabatic winds influencing sea ice conditions).

With the circum-Arctic area being drained by some of the worlds largest rivers, and having repeatedly experienced large-scale glaciations, the history of exchange of water between the Arctic Ocean and the North Atlantic is of much interest for paleoclimate research. An area exceptionally well suited to study this history is the Fram Strait between Greenland and the Svalbard Archipelago, the only deep connection between the Arctic Ocean and the North Atlantic. Located in the north-eastern Fram Strait, the submarine Yermak Plateau (Fig. 2) provides ideal conditions to retrieve undisturbed sedimentary records of high temporal resolution, such as core PS2837-5 investigated in this study (see Chapter 2).

Paleoceanographic research employs many tools, among which provenance analyses are particularly useful for the reconstruction of ocean currents. Increasingly, provenance studies are conducted by means of Sm–Nd isotopic investigations. Shortly after its introduc-
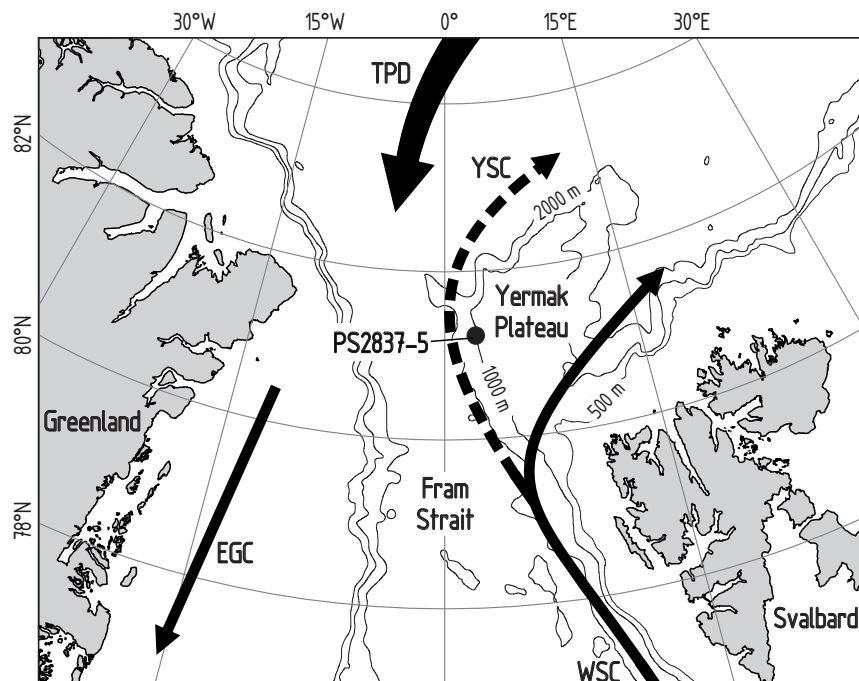
Figure 2 : Map of the Fram Strait region, showing the location of the investigated sediment core PS2837-5. Arrows depict simplified features of water circulation; WSC = West Spitsbergen Current, YSC = Yermak Slope Current, TPD = Trans Polar Drift, EGC = East Greenland Current.

tion to the earth sciences in the mid-1970s, the Sm–Nd isotope system was first applied to questions of oceanography by O'Nions et al. (1978). Ever since, it has been used in oceanographic and paleoceanographic studies and by now is well established as a standard tool, as shown by the large number of recent papers (e.g. Rutberg et al., 2000; Tütken et al., 2002; Weldeab et al., 2002; Benson et al., 2003; Farmer and Barber, 2003; Piotrowski et al., 2004; Bayon et al., 2002, 2003, 2004; Lacan and Jeandel, 2001, 2004, 2005).

Two applications of the Sm–Nd isotope system to oceanography/paleoceanography can be distinguished. The first application employs the Nd isotopic composition of particulate matter (i.e. continental detritus) to trace the provenance of sediments (e.g. Revel et al., 1996; Tütken et al., 2002), thereby inferring the pattern of oceanic circulation. In order to trace the Late Quaternary history of sediment delivery to the Yermak Plateau, samples from sediment core PS2837-5 and from potential source areas were analyzed for their Sm–Nd systematics (see Chapter 2).

The second application is based on seawater-dissolved Nd. The oceanic residence time of Nd is shorter than the global turnover rate of water in the oceans (500-1000 years vs ~1000 years; Tachikawa et al., 2003), leading to isotopic differences between different water masses as a function of the average age of the surrounding land masses. These isotopic differences can be used as a tracer of inter- and intra-oceanic circulation. Since the work of O'Nions et al. (1978), Mn nodules have been used as an archive of seawater Nd. As a nodule grows layer by layer by precipitation of Fe-Mn phases from the surrounding seawater, a time series of the Nd isotopic composition of the seawater becomes recorded in the nodule. Since Mn nodules have high REE concentrations of up to several hundred $\mu g \cdot g^{-1}$, very small sample sizes can be analyzed. However, the slow growth rates of Mn nodules (on the order of mm/Ma), and the minimum mass of sample material that can physically be removed from the nodule, limit the temporal resolution. Mn nodules are therefore best suited to study events occurring over long timescales, such as the closure of the Central American Isthmus (Burton et al., 1997).

A solution to the problem of poor temporal resolution has been found in Fe-Mn oxyhydroxides distributed throughout the sediment column, mainly as coatings on foraminifers (Palmer, 1985; Haley and Klinkhammer, 2002) or detrital particles (Sholkowitz et al., 1994). Here, the difficulty lies in the extraction of these Fe-Mn phases without contamination from other sedimentary components. A method for the extraction of Fe-Mn phases from pelagic sediments by means of chemical leaching has first been published by Chester and Hughes (1967), and various refined extraction methods have been proposed since (Tessier et al., 1979; Chao and Zhou, 1983; Hall et al., 1996). None of these studies, however, investigated the Nd isotopic compositions of the extracted Fe-Mn phases. This was first done in a study of North Atlantic Deep Water export to the South Atlantic during the Late Quaternary by Rutberg et al. (2000).

Finely dispersed Fe-Mn phases as an archive of seawater Nd were investigated within this thesis in a first attempt to apply the method to Arctic paleoceanography. Samples from sediment core PS2837-5 were subjected to various leaching procedures (see Chapters 2.2.3 and 2.2.4), and the leachates were analyzed for their REE concentrations and Nd isotopic compositions. As can be seen below, the results raised questions about the general applicability of the method (discussed in Chapter 4.4).

.   S

Although the focus of this study lies on the Yermak Plateau, the area of investigation includes potential source areas of sediments deposited at the location of core PS2837-5. The main source areas can be expected to lie within the Arctic, although sediment delivery during the Last Glacial Maximum from as far south as the North Sea has been reported (Spielhagen, 1991).

Following the definition used in the Arctic Monitoring and Assessment Programme (AMAP, 1998), the marine Arctic area (Fig. 3) includes the Arctic Ocean, the adjacent shelf seas (Beaufort, Chukchi, East Siberian, Laptev, Kara, and Barents Seas), the Nordic Seas (Greenland, Norwegian, and Iceland Seas), the Labrador Sea, Baffin Bay, Hudson Bay, the Canadian Arctic Archipelago, and the Bering Sea. The Arctic Ocean is connected with the Pacific Ocean via the shallow Bering Strait and the Bering Sea. Exchange of water with the Atlantic Ocean occurs through the Canadian Arctic Archipelago and the Barents Sea (both shallow), and the deep Fram Strait with a sill depth of approximately 2600 meters (Johnson, 1990). The Lomonosov Ridge divides the deep Arctic Ocean into two main basins: the Canadian Basin (subdivided into the Canada Basin and the Makarov Basin by the Alpha/Mendeleev Ridge) and the Eurasian Basin (subdivided into the Amundsen Basin and the Nansen Basin by the Gakkel Ridge). The active Gakkel Ridge, spreading at rates of 2-20 mm/a (Johnson, 1990; Fütterer, 1992), is connected to the Mid-Atlantic ridge system through the Fram Strait transform fault system.

.   H

The hydrography of the Arctic Ocean will be described here only briefly, and, where necessary, will be dealt with later in more detail (for details see AMAP, 1998, and references therein). Generally, the Arctic Ocean can be characterized by a stable stratification of three layers of different water masses with different circulation patterns: the surface layer, the Atlantic layer, and the Arctic deep-water.

The surface of the Arctic Ocean is characterized by a near-complete permanent sea ice cover, and is dominated by two large-scale features of circulation: the Trans Polar Drift
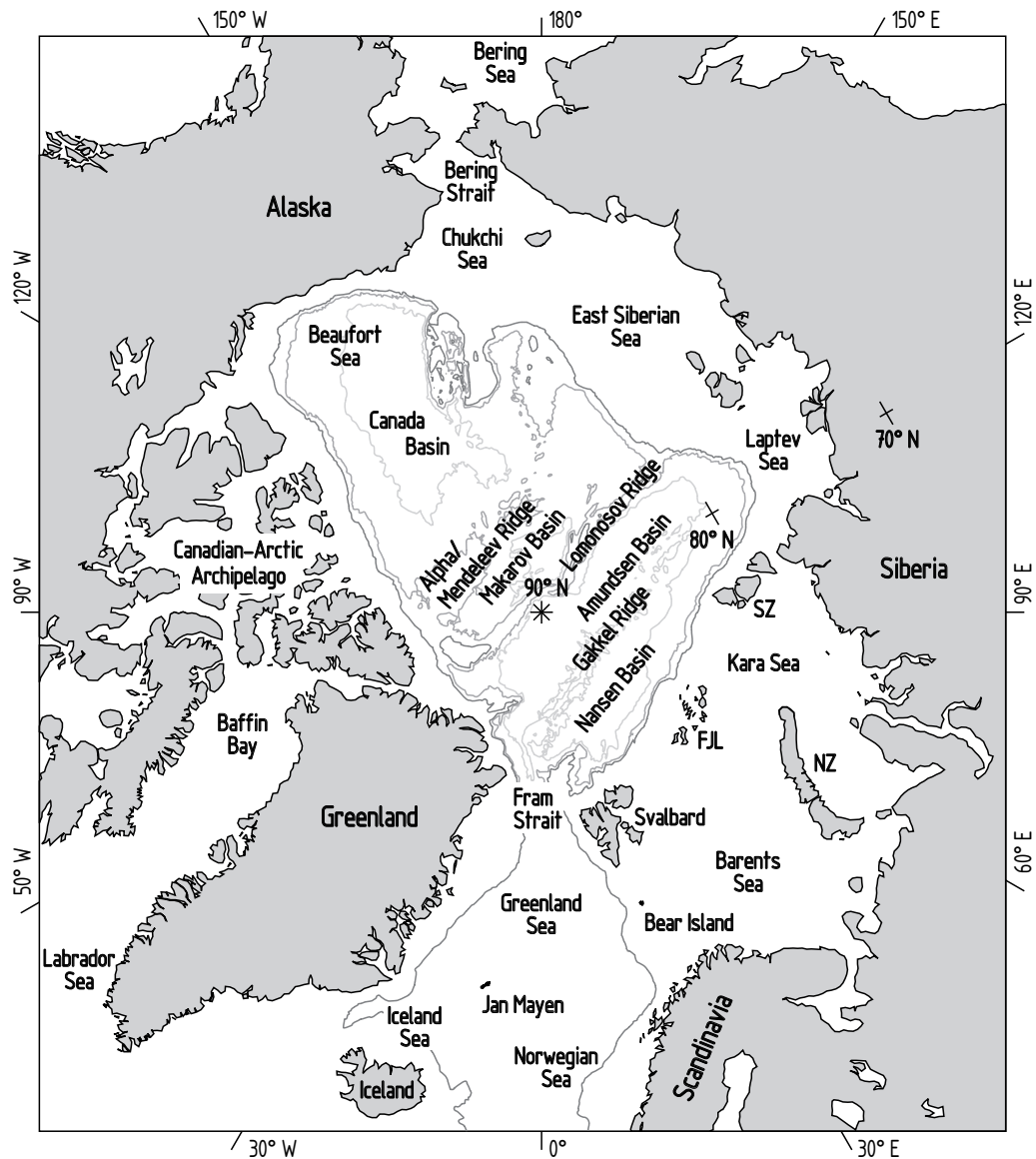
Figure 3 : Map of the Arctic Ocean and adjacent areas. Morphological features of the central Arctic Ocean are illustrated by the 1000 m, 2000 m, and 3500 m isobaths. In the Nordic Seas (Greenland Sea, Norwegian Sea, and Iceland Sea) only the 1000 m isobath is shown. FJL = Franz Josef Land, NZ = Novaya Zemlya, SZ = Severnaya Zemlya.

(TPD) and the Beaufort Gyre (BG). The Trans Polar Drift (TPD) extends from the Siberian shelves to the western Fram Strait (Fig. 4), each year carrying approximately 2850 km^3 of sea ice out of the Arctic Ocean (Vinje et al., 1998). Sea ice formed in the Laptev Sea, for instance, takes about three years to travel to the Fram Strait (Rigor, 1992), and, after leaving the Arctic Ocean, is transported south along the coast of Greenland by the East Greenland Current. The BG, rotating in a clockwise direction, extends over the entire Canadian Basin.

Sea ice formed in the Beaufort, Chukchi, and East Siberian Seas may circulate within the BG for more than five years (Thorndike, 1986) before being destroyed or leaving the Arctic Ocean through the Canadian Arctic Archipelago. Limited exchange between the TPD and the BG occurs along the Lomonosov Ridge. The surface layer is fed by inflow of Atlantic water through Fram Strait and the Barents Sea, Pacific water through the Bering Strait, and by continental run-off. Outflow occurs through the Canadian Arctic Archipelago, the Fram Strait, and, to a lesser degree, through the Barents Sea. The amount and routing of freshwater exported from the Arctic Ocean is thought to at least in part control deep-water formation processes in the Labrador Sea and the Nordic Seas (Aagaard and Carmack, 1989).

The intermediate depths of the Arctic Ocean are occupied by water of Atlantic origin. Warm and saline Atlantic water enters the Nordic Seas with the Norwegian Atlantic Current, following the western Scandinavian margin northwards (Fig. 4). Some of this water is deflected to the east and enters the Arctic Ocean via the Barents Sea. The remaining Atlantic water continues northward along the western Barents Sea margin as the West Spitsbergen Current (WSC), and partly recirculates to the west into the Greenland Sea. North of Svalbard, the upper part of the WSC is deflected eastwards by Coriolis forcing. The lower part continues northward as the Yermak Slope Current (YSC), and is deflected eastwards north of the submarine Yermak Plateau (Fig. 2). Upon entering the Arctic Ocean, the Atlantic water submerges below the surface layer and follows the continental slope eastwards. Flowing in a generally anticlockwise direction, the Atlantic water circulates through the different basins of the Arctic Ocean in several loops (Fig. 5). Along the way it is modified by diffusion and mixing with surrounding water masses, before eventually leaving the Arctic Ocean through the western Fram Strait.

In the deep Arctic Ocean, Canadian Basin Deep Water and Eurasian Basin Deep Water can be distinguished (AMAP, 1998). Canadian Basin Deep Water is relatively warm and saline (-0.5 °C, 34.955), whereas Eurasian Basin Deep Water is colder and fresher (-0.95 °C, 34.945). Communication between the two basins across the Lomonosov Ridge is limited. While the Canadian Basin is largely cut off from the global deep-water circulation, the Eurasian Basin receives Norwegian Deep Sea Water through the Fram Strait. The major source of deep-water in both basins, however, is thought to be highly saline water formed during sea ice formation in various places on the shelves (Anderson et al., 1994). Circulation is anticlockwise in both basins (Fig. 6). Outflow of deep-water from the Arctic Ocean occurs exclusively through the western Fram Strait.
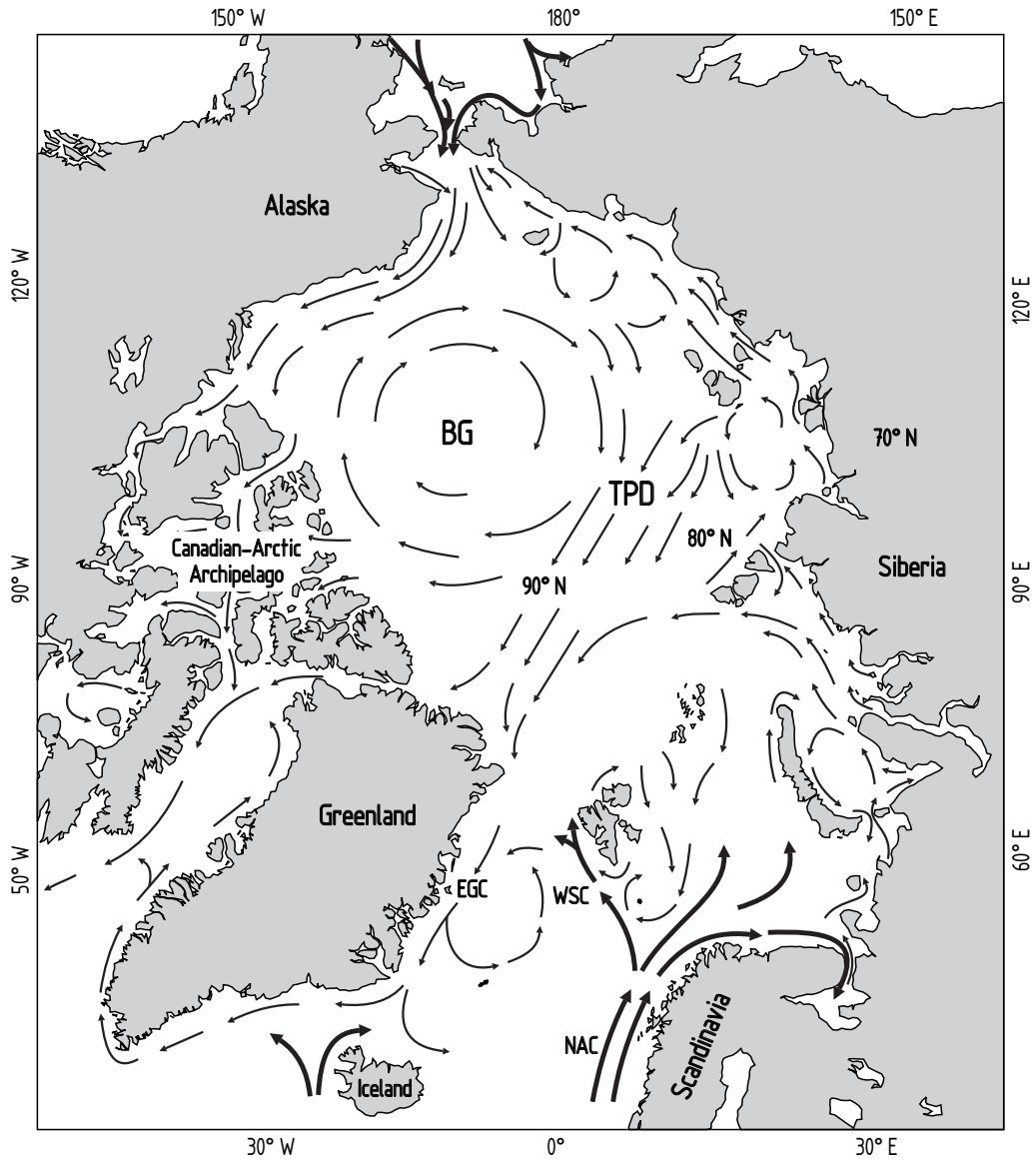
Figure 4: Simplified pattern of surface circulation in the Arctic Ocean and adjacent areas. Inflow of temperate waters is represented by thick arrows; thin arrows depict cold waters of Arctic origin. BG = Beaufort Gyre, TPD = Trans Polar Drift, EGC = East Greenland Current, WSC = West Spitsbergen Current, NAC = Norwegian Atlantic Current. After AMAP (1998).
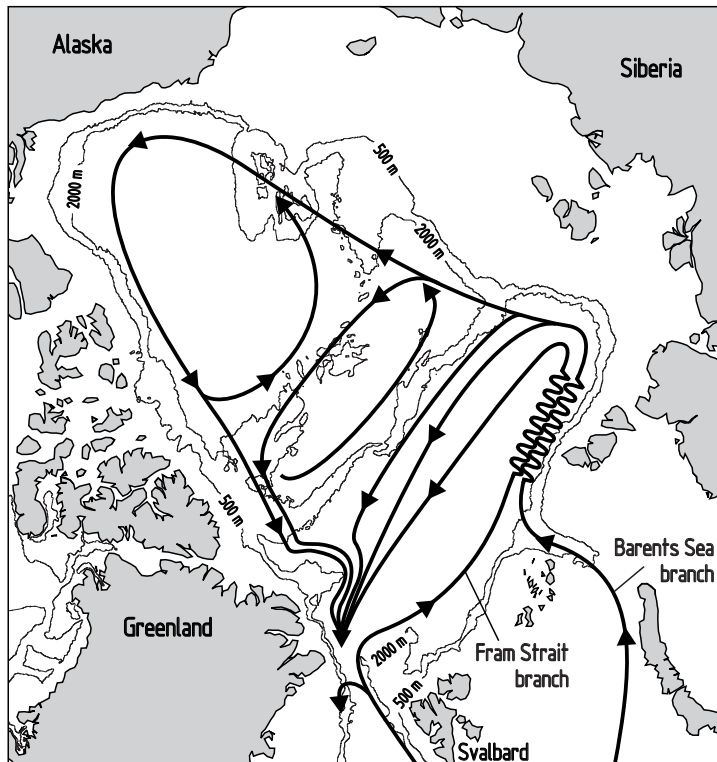
Figure 5: Schematic illustration of intermediate water circulation in the Arctic Ocean. After Rudels et al. (1994).
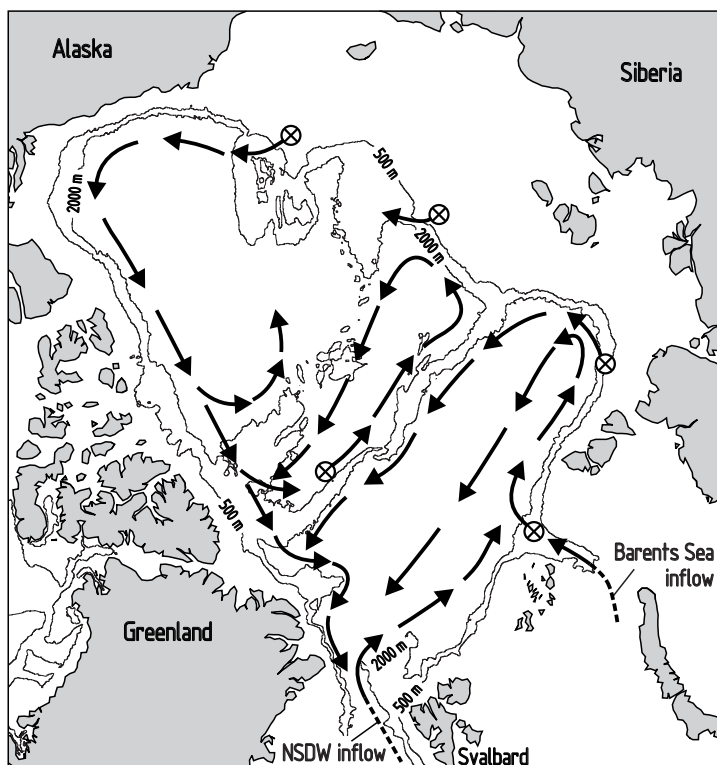
Figure 6: Schematic illustration of deep-water circulation in the Arctic Ocean. ⊗: regions where dense shelf waters are thought to intrude deeper water masses. NSDW = Norwegian Sea Deep Water. After Jones et al. (1995).

.   S

Marine sediments potentially are mostly heterogeneous multi-component mixtures result-
ing from a variety of processes and sources (summarized in Fig. 7). Of primary interest for
provenance studies is the terrigenous detritus. It may be transported as atmospheric dust
(aeolian input), by gravitational down-slope movements (turbidity currents), as suspended
load of ocean currents, and, unique to high latitudes, as ice rafted detritus (IRD).

Particles of wind-blown dust can represent a valuable source of information for the re-
construction of atmospheric conditions, but may hamper provenance analysis with regard
to current-transported material. Biscaye et al. (1997) studied dust particles extracted from
the Greenland Ice Sheet Project (GISP 2) ice core, and found them to have a mean grain
size of 1.2 µm. Atmospheric dust would therefore only be found in the clay fraction of the
sediment samples. Mass accumulation rates of dust in the GISP 2 samples range from 1.7 to
14.4 mg$\times$cm$^{-2}\times$ka^{-1}, two to three orders of magnitude lower than the minimum sediment
accumulation rate of ~2 g$\times$cm$^{-2}\times$ka^{-1} for the sediment core investigated in this study (C.
Hass, personal communication). Biscaye et al. (1997) also found the Nd isotopic compo-
sitions of the dust samples to scatter around ε_{Nd} -10. As shown below, these values are
similar to those determined for the investigated core samples from the Yermak Plateau. It
can therefore be assumed that a wind-blown-dust component would not significantly alter
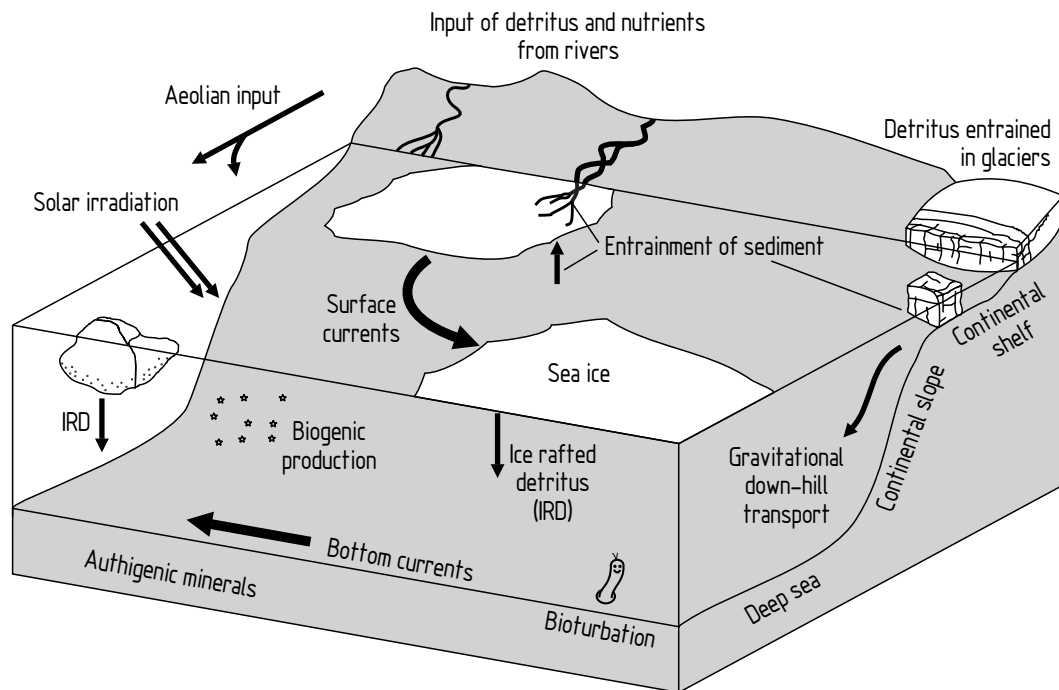
Figure 7 : Cartoon illustrating sedimentary processes at high latitudes.
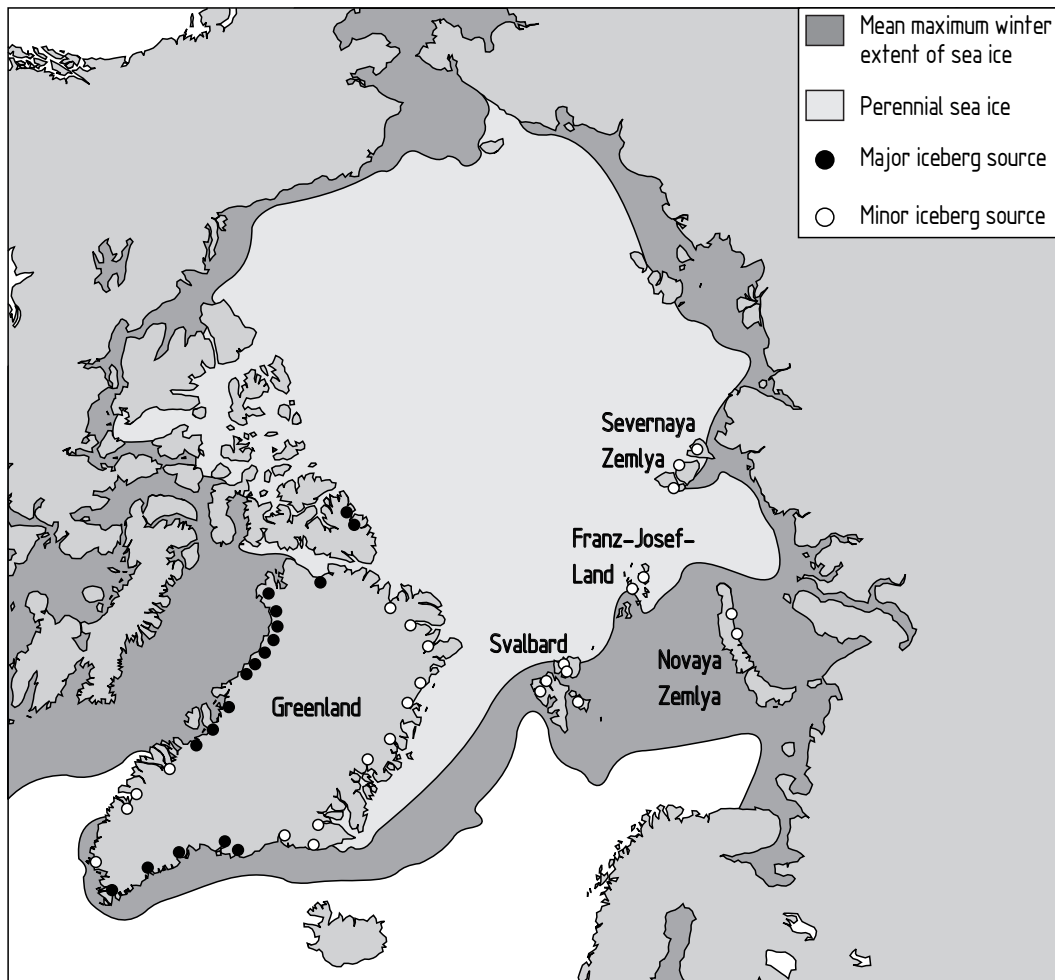
Figure 8 : Extent of sea ice in the Arctic Ocean, and major/ minor sources of icebergs. Modified from Grantz et al. (1990). Iceberg sources from Vogt (1997).

the Sm-Nd characteristics of the analyzed samples.

Currents in the open ocean rarely have velocities high enough to keep grains > 63 μm in suspension (McCave et al., 1995b). Transport of grains > 63 μm is therefore largely restricted to gravitational down-slope movements and ice rafting. The position of the investigated sediment core on the upper slope of the Yermak Plateau (see Fig. 2 in Chapter 2.1) was chosen as to minimize the risk of disturbance by turbidity currents, and careful examination of the core revealed no signs of disturbance (C. Hass, personal communication, see also core description in Appendix C, pp. 103-105). All detritus > 63 μm is therefore assumed to by exclusively ice rafted.

Floating ice can transport large amounts of terrigenous material over long distances. While icebergs may carry material of all grain sizes (up to boulder size), sea ice-rafted

sediments are mainly composed of silty clay, with generally low contents of (mainly fine) sand (Wollenburg, 1993). The restriction to finer grain sizes, as compared to icebergs, reflects suspension freezing as the major mechanism of sediment entrainment into sea ice (Reimnitz et al., 1994; Dethleff, 1995). This mechanism mainly occurs in shallow shelf areas, where suspended (or resuspended) sediment particles become trapped in growing ice crystals floating to the surface. Sediments can also be deposited on top of ice floes, when, during the break up of rivers in spring, sediment-laden river water flows onto the sea ice where it looses its sediment load.

Sediment transport by icebergs is of minor importance under modern interglacial conditions, but in some areas has been the dominant mechanism during times of large-scale glaciations. During Heinrich events, for instance, IRD layers up to one meter thick were deposited in the North Atlantic within a few hundred years by armadas of icebergs released from circum-North Atlantic ice sheets (Cronin, 1999). Today, icebergs are released only from the Greenland ice sheet and minor ice caps on Svalbard, Franz Josef Land, Novaya Zemlya, Severnaya Zemlya, and some islands of the Canadian Arctic Archipelago (Fig. 8). Sea ice rafting, on the other hand, is supposed to be the main mechanism of sediment transport to the modern deep Arctic Ocean (Nürnberg et al., 1994; Eicken et al., 2000), and may also be a significant factor at the Yermak Plateau. Approximately 14 million km^2 of the Arctic Ocean are covered with sea ice at the peak of winter (Fig. 8). Intense summer melting reduces the ice cover to ca. 7 million km^2, releasing huge amounts of sediment in the process. Other mechanisms of sediment release are subsurface melting of ice in warm water, and mechanical destruction of ice floes (e.g. during build-up of pressure ridges; Wollenburg, 1993).

S

. S

. . L Q — PS -

Kastenlot core PS2837-5 (81° 13.99´ N, 2° 22.85´ E, 1042 m water depth, 8.76 m recovery) and its companion boxcore PS2837-6 (recovery 0.49 m) were collected during the expedition ARK XIII/2 of *RV Polarstern* (Stein and Fahl, 1997). The core location on the western slope shoulder of the Yermak Plateau (Fig. 2), north of the modern summer ice margin, was chosen on the basis of shipboard PARASOUND echosounding data, suggesting high sediment accumulation at the site (C. Hass, personal communication). The sediments are dominantly clayey silts and silty clays, with sand (> 63 µm) contents ranging from 0 wt % to 29 wt % (see Fig. 9, and core descriptions in Appendix C). Individual samples represent slices of 1 cm thickness, and are named after their depth in the core; e.g. PS2837-5/55 is a slice of sediment between 55 cm and 56 cm below the core top.

According to the age model (see next section) the sediment record covers the last 129 ka, corresponding to MIS 1-5 (Marine Isotope Stages, after Martinson et al., 1987). In the following, all ages are given as calendar years BP (before present, 0 BP = AD 1950) unless otherwise stated.

. . . A - PS -

Age-depth models usually are constructed from a combination of absolute age determinations (e.g. ^{14}C dates) and correlation of proxy records (e.g. foraminiferal δ^{18}O) with other well dated records, such as ice cores. 15 AMS (accelerator mass spectrometry) ^{14}C dates and several proxy parameters are available for core PS2837-5. Of these proxies, only the record of grain-size composition covers the whole length of the core with high sampling density. However, in the case of core PS2837-5 the grain-size record does not allow a straightforward interpretation[†], and can therefore not be used to establish an age-depth model.

Age-depth information for core PS2837-5 has been published by Hass (2002), Levitan et al. (2002a), Nørgaard-Pedersen (2002), Nørgaard-Pedersen et al. (2003), Vogelsang and Sarnthein (2003), Birgel and Hass (2004), and Wollenburg et al. (2004). The age-depth

---

[†]The mean grain size of the sortable silt fraction (10-63 µm) can be used as a proxy for current strength, if the material in this grain-size range is exclusively transported as suspended load (Bianchi and McCave, 1999; McCave et al., 1995a,b). This criterion, however, is not met in the case of core PS2837-5.
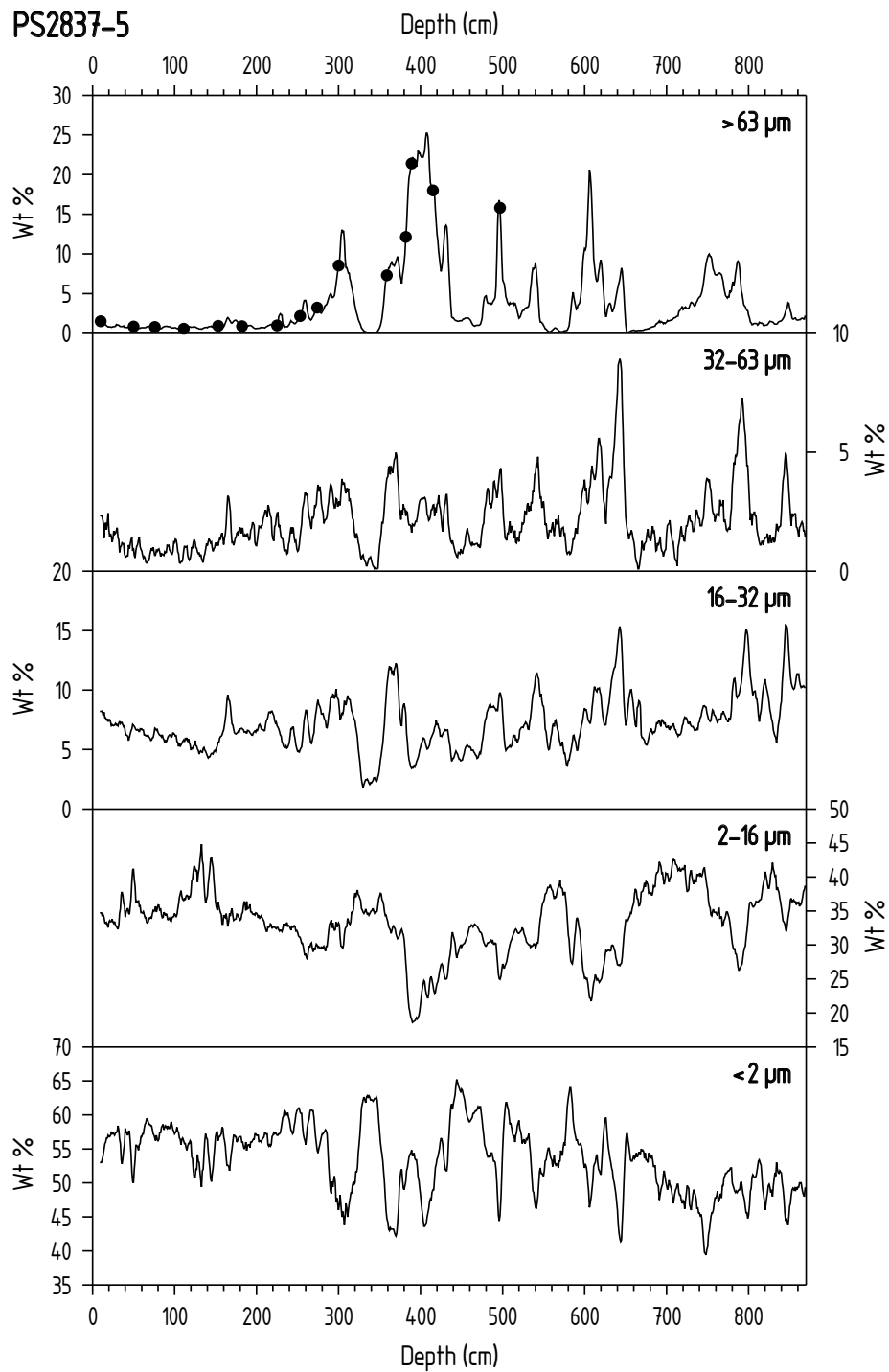
Figure 9 : Downcore abundance variations (5 point running averages of wt % vs depth in core) of five grain-size classes in core PS2837-5. Grain-size data from Hass (2000). Filled circles in the uppermost panel represent samples with ^{14}C ages from Nørgaard-Pedersen et al. (2003).

models in these studies are all based on the same AMS ^{14}C measurements performed at the AMS facility at the Leibniz Laboratory, Kiel University, Germany. The conversion of ^{14}C years to calendar years was in all cases performed with the INTCAL98 calibration data set (Stuiver et al., 1998). However, the calibrated ages show marked differences. As the cited studies provide neither detailed information about the calibration process, nor uncertainties of the calibrated calendar ages, these differences are difficult to explain. Also, only Levitan et al. (2002a) presented an age-depth model for the entire length of the core, although they do not explicitly explain how the model is constructed beyond the limit of ^{14}C dating. For the sake of transparency, a new age-depth model was constructed in this study from recalibrated ^{14}C dates from Nørgaard-Pedersen et al. (2003), and linear interpolation between age tie points (Table 1). This new age-depth model is described in the following paragraphs, and shown in Fig. 10.

Down to 389 cm core depth the new model is based on 13 AMS ^{14}C dates from Nørgaard-Pedersen et al. (2003), converted to calendar years with revision 5.10 beta of the CALIB software (Stuiver and Reimer, 1993) and the Marine04 calibration data set of Hughen et al. (2004b). In addition to gaining full control over the calibration process, and obtaining uncertainties of the calibrated ages, the recalibration benefits from an extended calibration data set and an improved calibration algorithm that has been developed for the Marine04 calibration (Blackwell et al., 2006).

The construction of an age-depth model for the core section below 389 cm was more difficult. Although there are AMS ^{14}C dates for samples at 415 cm (23.83 ^{14}C ka) and 497 cm (48.76 ^{14}C ka) depth (Nørgaard-Pedersen et al., 2003), these ages are of limited use for the model; the ages > 21.7 ^{14}C ka are beyond the limit of the Marine04 calibration. Calendar age estimates, or rather age range estimates, for samples older than 21.7 ^{14}C ka can be derived from ^{14}C year–calendar year curves, such as the ones of Voelker et al. (1998), Hughen et al. (2004a), and Fairbanks et al. (2005). According to the data presented in these studies, the samples at 415 cm and 497 cm have ages of between ca. 26 ka and 30 ka, and ca. 43 ka and 60 ka, respectively. Due to the large uncertainties, these two dates were not considered. Instead, the age-depth model for this part of the core was constructed by linear interpolation between the oldest reliable ^{14}C date at 389 cm and an age estimate for the core bottom.

No reasonable minimum age estimate can be given for the core bottom, but the maximum age can be constrained with some confidence. Given the absence of a prominent peak in the abundance of coarse-grained material in the lowest part of the core (see Fig. 9), it can plausibly be assumed that the core does not extend to the penultimate glacial maximum (MIS 6). The maximum age of the core bottom can therefore be confined to the MIS 5/6 boundary at 129 ka. From this age for the core bottom follows a linear sedimentation rate of 4.40 cm·ka^{-1} for the core section below 389 cm, which is well within the range of observed

sedimentation rates in other cores from the Yermak Plateau (Levitan et al., 2002a). Using this sedimentation rate of 4.40 cm·ka^{-1}, the ages of the samples at 415 cm and 497 cm can be calculated to be 26.07 ka and 44.70 ka, respectively, falling within the possible calendar year ranges determined for the ^{14}C dates.
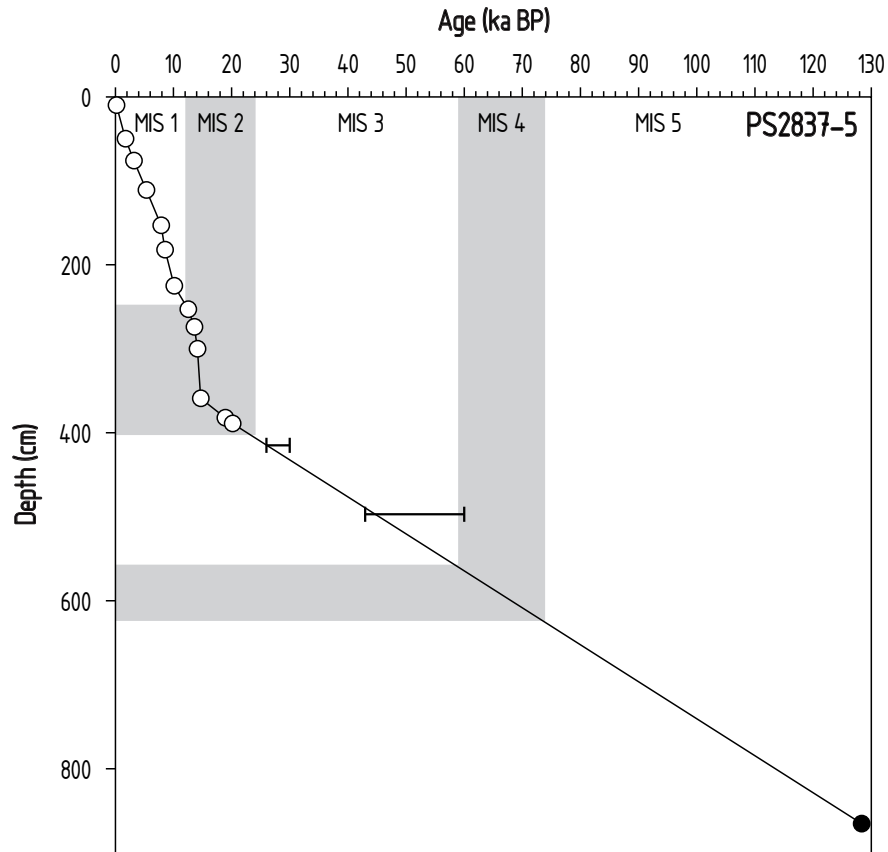
Figure 10 : Age-depth model for core PS2837-5, based on linear interpolation between age tie points. Open circles: ^{14}C dates from Nørgaard-Pedersen et al. (2003), converted to calendar years with revision 5.10 beta of the CALIB software (Stuiver and Reimer, 1993) and the Marine04 calibration data set (Hughen et al., 2004b). Black bars: possible calendar age ranges for AMS ^{14}C dated samples at 415 cm and 497 cm from Nørgaard-Pedersen et al. (2003), based on data from Voelker et al. (1998), Hughen et al. (2004a), and Fairbanks et al. (2005). Filled circle: age estimate for core bottom based on sedimentological parameters; see text for details. MIS 1-5 are Marine Isotope Stages after Martinson et al. (1987).

Table 1 : AMS ^{14}C data from cores PS2837-5 and PS2837-6.

Core	Depth (cm)	^{14}C years ± 1σ [a]	Lab. code	Calendar years BP [b] 2σ range	Weighted avg [c]
PS2837-6	10	135 ± 25	KIA 7570	69 – 260	170
PS2837-5	50	1730 ± 40	KIA 4652	1594 – 1828	1720
PS2837-5	76	2940 ± 35	KIA 8927	3079 – 3316	3200
PS2837-5	111	4565 ± 45	KIA 8928	5139 – 5454	5320
PS2837-5	153	7005 ± 45	KIA 8929	7761 – 7962	7870
PS2837-5	182	7670 ± 60	KIA 4653	8388 – 8694	8530
PS2837-5	225	8890 ± 60	KIA 8930	9913 – 10 239	10 110
PS2837-5	253	10 540 ± 50	KIA 7571	12 339 – 12 751	12 530
PS2837-5	274	11 755 ± 60	KIA 10863	13 439 – 13 747	13 600
PS2837-5	300	12 255 ± 60	KIA 7572	13 924 – 14 420	14 130
PS2837-5	359	12 540 ± 70	KIA 10864	14 250 – 15 024	14 670
PS2837-5	382	15 640 ± 80	KIA 10865	18 760 – 19 008	18 890
PS2837-5	389	17 040 ± 110	KIA 4654	19 917 – 20 409	20 160
PS2837-5	415	23 830 ± 180	KIA 7573	ca. 26-30 ka [d]	
PS2837-5	497	48 760 +4810/-2990	KIA 4655	ca. 43-60 ka [d]	
PS2837-5	869				129 ka [e]

[a] From Nørgaard-Pedersen et al. (2003), reservoir corrected by minus 400 years.

[b] This study. ^{14}C years converted to calendar years with revision 5.10 beta of the CALIB software (Stuiver and Reimer, 1993) and the Marine04 calibration data set (Hughen et al., 2004b).

[c] Age tie points used for the construction of the continuous age-depth model. Weighted averages are calculated from probability distributions.

[d] These are not calibrated 2σ ranges, but possible calendar year ranges derived from ^{14}C year–calendar year curves from Voelker et al. (1998), Hughen et al. (2004a), and Fairbanks et al. (2005).

[e] Age estimate for the core bottom based on sedimentological parameters; see text for details.

Although the age estimate for the core bottom is uncertain, and the sedimentation rate is unlikely to have remained constant for more than 100 ka, the chosen approach to the construction of the age-depth model appears to be the most objective, involving a minimum of untestable assumptions. It should, however, be kept in mind that the age model below 389 cm can at best be a rough approximation that may at any given depth be wrong by several thousand years.

. . M S

. . . R

L17, L18, L20, L21, and L22—supplied by V. Rachold (Alfred Wegener Institute for Polar and Marine Research (AWI), Bremerhaven)—are river-bed surface sediments from dif-

ferent localities along the major outflow of the Lena River in the eastern part of its delta (Rachold et al., 1995). L18, L20, and L21 consist of sand-size material only. L17 contains 3.7 wt % clay, 18.2 wt % silt, and 78.1 wt % sand, and L22 is composed of 8.7 wt % clay, 54.2 wt % silt, and 37.1 wt % sand. See Fig. 11 for a map, Fig. 12 for a satellite image, and Table 11 for coordinates.

BP01/72—supplied by F. Schoster (AWI, Bremerhaven)—was collected from the Ob River estuary during the Kara Sea expedition SIRRO 2001 of *RV Akademik Boris Petrov* (Stein and Stepanets, 2002). It is a river-bed surface sediment, composed of 19.5 wt % clay, 26.4 wt % silt, and 54.1 wt % sand (F. Schoster, personal communication). See Fig. 11 for a map, Fig. 13 for a satellite image, and Table 11 for coordinates.

BP00/15—supplied by F. Schoster (AWI, Bremerhaven)—was collected from the Yenisei River estuary during the Kara Sea expedition SIRRO 2000 of *RV Akademik Boris Petrov* (Stein and Stepanets, 2001). It is a river-bed surface sediment composed of 9.0 wt % clay, 85.7 wt % silt, and 5.3 wt % sand (F. Schoster, personal communication). See Fig. 11 for a map, Fig. 13 for a satellite image, and Table 11 for coordinates.

. . .   B

WoA, WoF, WoG (Kongsfjorden, West Spitsbergen) and WoC, WoD, and WoE (Isfjorden, West Spitsbergen)—supplied by C. Hass (AWI, Bremerhaven)—are beach deposits collected during the expedition ARK-XVI/2 of *RV Polarstern* (Krause and Schauer, 2001). WoA, made up of shale fragments, can be related to outcrops of the Late Paleozoic Gipsdalen Group on the Brøggerhalvøya peninsula (Dallmann, 1999). WoF and WoG are coarse crystalline sands, derived from pre-Old Red basement rocks outcropping north of Kongsfjorden (Dallmann, 1999). WoC, WoD, and WoE consist of fragments of shales and siltstones that can be related to the Mesozoic Adventdalen, Kapp Toscana, and Sassendalen groups outcropping on the southern and northern shores of Isfjorden (Dallmann, 1999). See Fig. 11 for a map, Fig. 41 in Appendix B (p. 97) for a satellite image, and Table 11 for coordinates. No photographs of the sampling sites are available, but Figs. 42 and 43 in Appendix B (p. 98) provide a general impression of the area.

. . .   I   (IRD)

K3-1, K5-2, K6-1, and K6-2—supplied by C. Kierdorf (AWI, Bremerhaven)—are samples of ice-rafted detritus (IRD) from sediment-laden sea ice in the central Fram Strait. The samples were collected during expedition ARK-XVIII/1 of *RV Polarstern* (Lemke, 2003). See Fig. 11 for a map, and Appendix B (pp. 99-102) for color photographs and descriptions of the sampling sites.

Ice80-30—supplied by C. Hass (AWI, Bremerhaven)—is a very fine-grained IRD sample from the Fram Strait at ~80° 30´ N, 02° E, collected from sediment laden sea ice during expedition ARK-XIII/2 of *RV Polarstern* (Stein and Fahl, 1997). See Fig. 11 for a map.
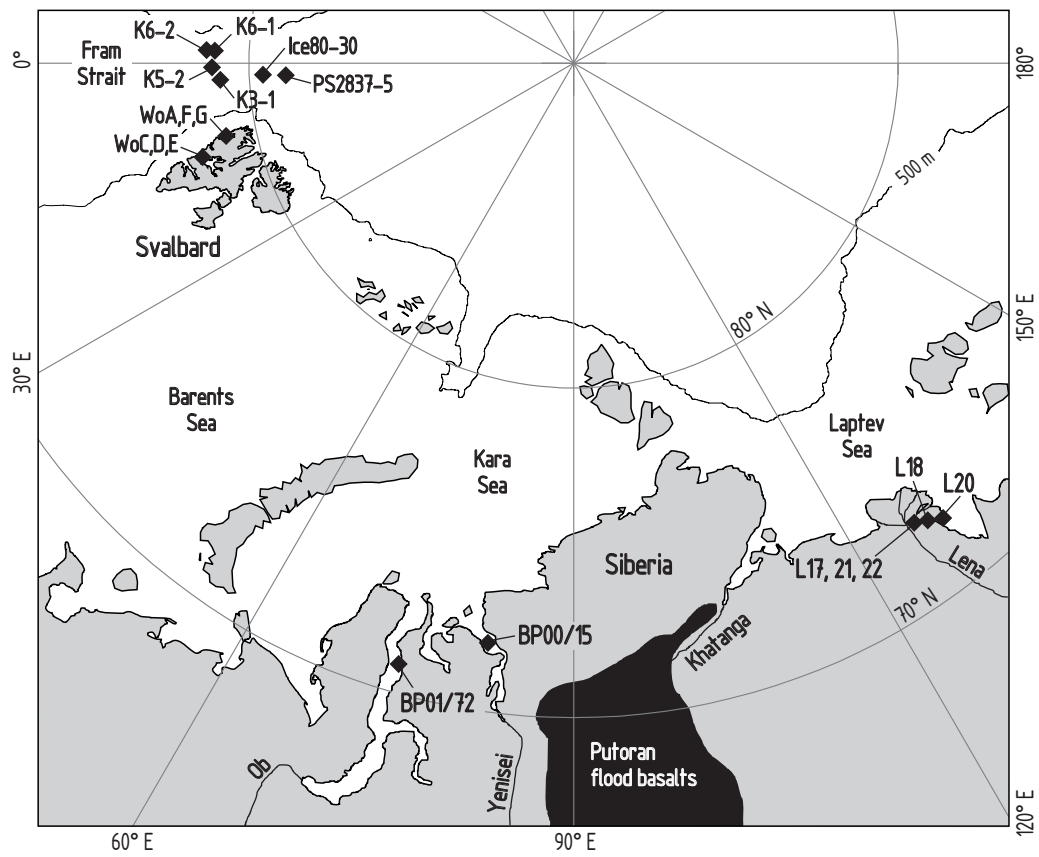
Figure 11 : Sampling locations of modern samples from the central Fram Strait, Svalbard, and Siberia. See Table 11 for coordinates.
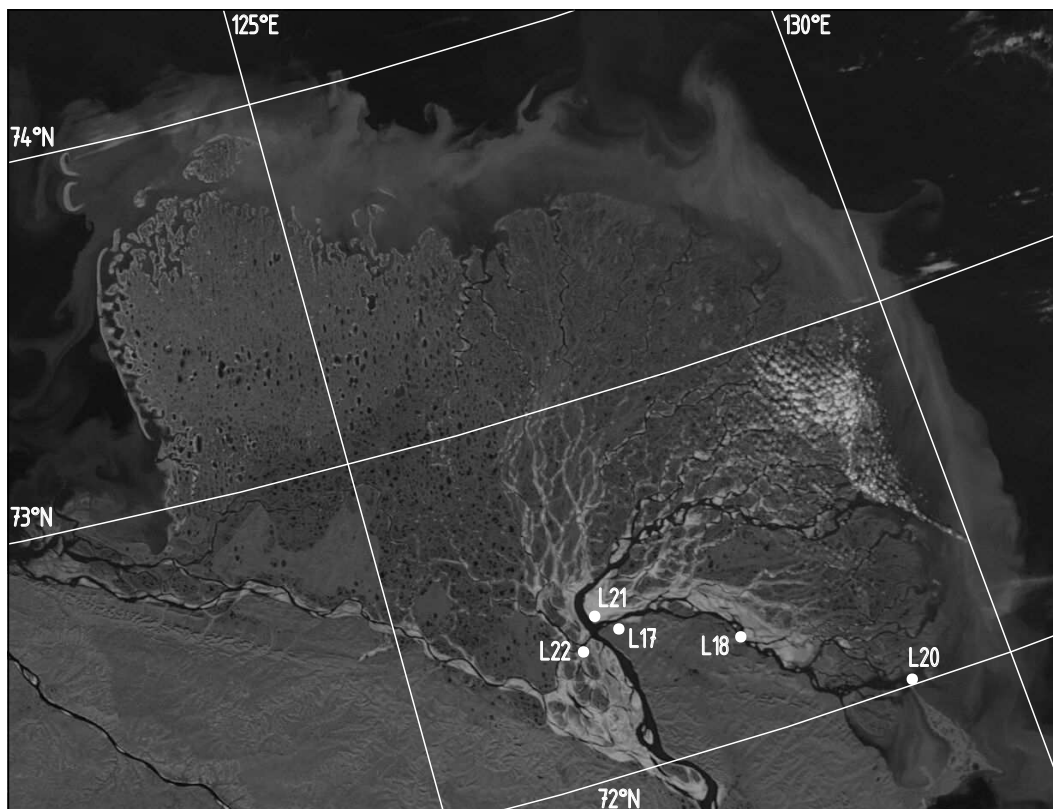
Figure 12 : Satellite image of the Lena River delta, including sampling sites of river sediments. Image courtesy of MODIS Rapid Response Project at NASA/GSFC (2002/238-08/26, 4:40 UTC, satellite Terra, pixel size 250 m, center of image 72.5° N, 125° E).
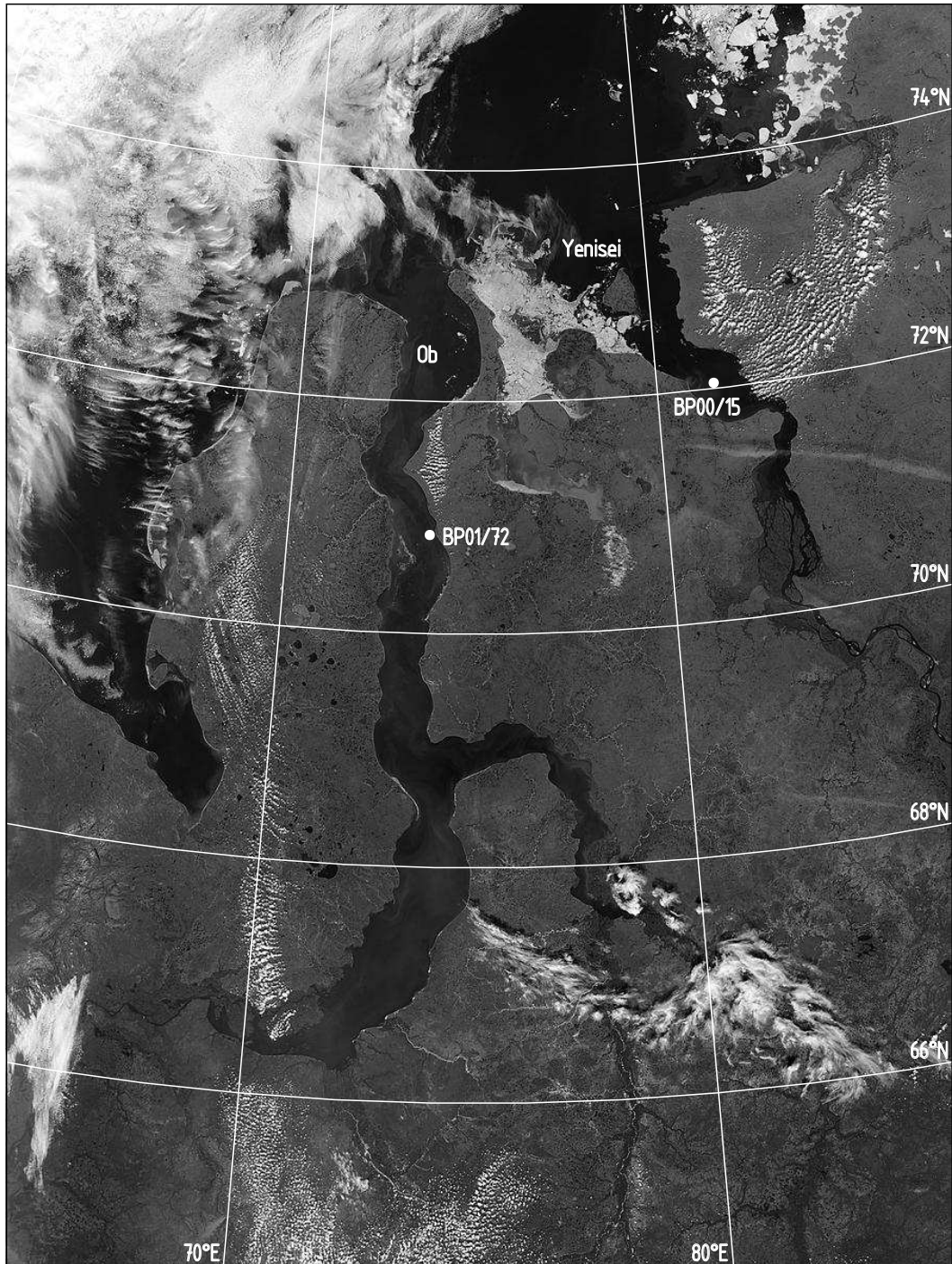
Figure 13 : Satellite image covering the Ob and Yenisei River estuaries, including sampling sites
of river sediments. Image courtesy of MODIS Rapid Response Project at NASA/GSFC
(2004/201-07/19, 6:55 UTC, satellite Aqua, pixel size 1km, center of image 70° N, 75° E).

.   S

. .   S

Most of the sample preparation at the pretreatment stage has been carried out prior to this study by members of AWI, Bremerhaven. Samples, after being collected, were stored at 4 °C until further processing. In a first step, they were freeze dried for the determination of dry mass. To remove organic material, the samples were suspended in a 3.3 mol·l^{-1} solution of H_2O_2 and left to react for several days, followed by repeated cycles of washing with deionized water. The sand fractions were separated by passing the material through a 63 μm screen. After drying, the sand fractions were split into sub-fractions of 63-250 μm, 250-500 μm, and > 500 μm by dry sieving. Biogenic carbonate, present in significant amounts in some sand samples, was removed from the samples chosen for isotopic analyses by leaching with HCl (0.1 mol·l^{-1}), followed by threefold rinsing with deionized water. The fractions < 63 μm were either dried, or kept in suspension for further processing.

. .   G   -   <   μ

The material < 63 μm of most samples was split into the sub-fractions clay (< 2 μm), fine silt (2-10 μm), and coarse silt (10-63 μm), or clay and silt (2-63 μm). The separation of samples into different grain-size fractions was performed with settling tubes in Bremerhaven and Munich. The settling tube method is based on Stokes's law, which describes the behavior of an ideal spherical particle in a liquid medium under the influence of gravity (with restriction to laminar flow). It allows the calculation of the time it takes for a spherical particle of known diameter and density to settle a given vertical distance in a liquid of known viscosity and density.

$$t = \left(174.85^2 \times \eta \times h\right) / \left(\left(D_1 - D_2\right) \times d^2\right)$$

t = settling time [min]

h = settling height [cm]

D_1 = density of the settling grain [g·cm^{-3}]

D_2 = density of the liquid [g·cm^{-3}]

η = viscosity of the liquid [g·cm^{-1}·s^{-1}]

d = equivalent diameter of the settling grain [μm]

The term equivalent diameter accounts for the non-spherical shape of sediment particles, i.e. a sediment particle with a certain equivalent diameter behaves like a sphere of the same diameter.
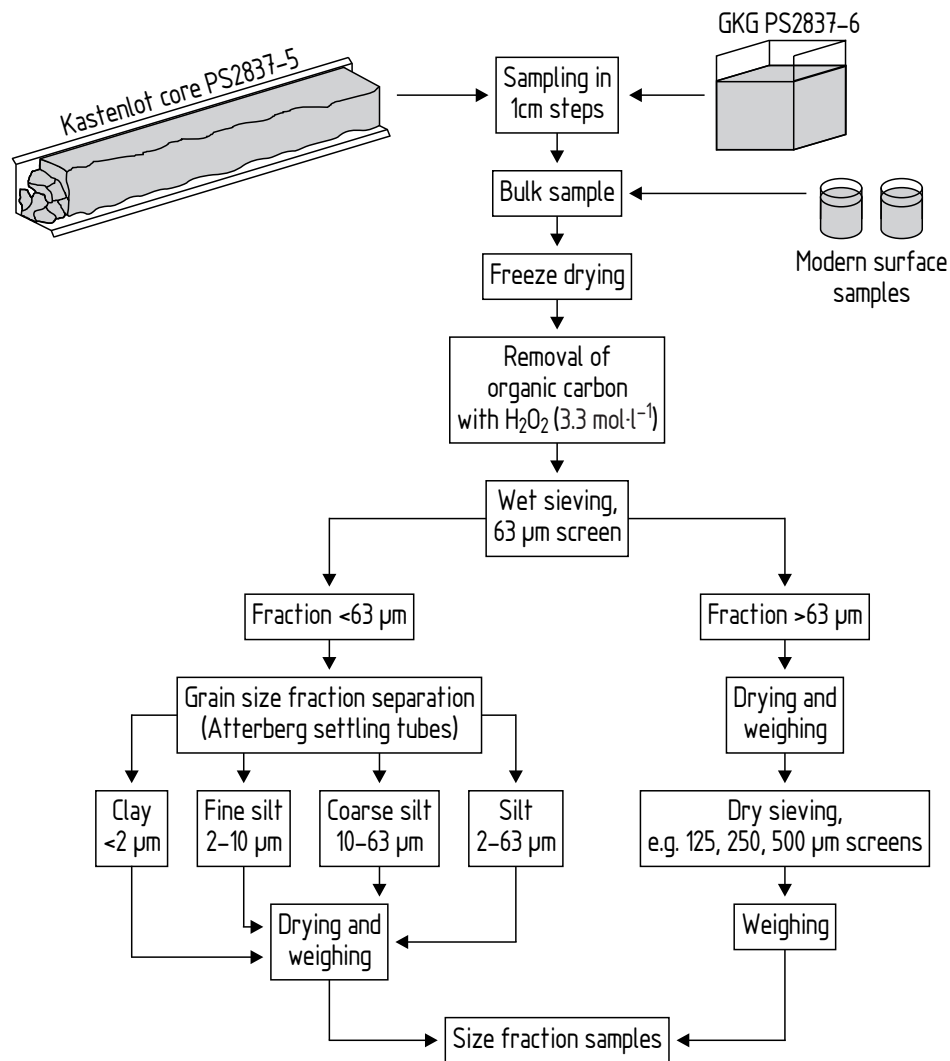
Figure 14: Flowchart of the sample preparation protocol applied at AWI, Bremerhaven, and Munich. GKG: Gross Kasten Greifer.

Grain-size separation was performed with glass cylinders, with upper and lower marks indicating the settling distance (**Fig. 15**). A suspension of the fraction < 63 μm in water was mixed with a pinch of sodiumpolyphosphate, placed on an orbital shaker for 24 hours to achieve complete disaggregation, and filled into a settling tube. The settling tube was then filled to the upper mark with an aqueous solution of ammonia (1.3 mmol·l^{-1}), which prevents reaggregation of cohesive particles. After the sediment had settled for the appropriate time the water column above the lower mark was drained and collected. The settling tube was refilled with the ammonia solution, the sediment suspension was thoroughly agitated, and allowed to settle again. This cycle was repeated until the water above the lower mark was clear after settling. Note that this method allows only near quantitative grain-size

Figure 15: Schematic illustration of the settling tubes in Bremerhaven (left) and Munich (right).

separation. Wollenburg (1993), for instance, reported 3-9 % of clay remaining in the silt fraction, even after numerous repetitions of the separation cycle. The Ob and Yenisei River samples were split into separate grain-size fractions by F. Schoster at AWI, Bremerhaven.

. . E   F -M   /
(HH)

The experimental procedure for the extraction of authigenic Fe-Mn oxides/hydroxides hosting a seawater Nd signal is based on a method first introduced by Chester and Hughes (1967). They suggested the use of an acidic-reducing solution of hydroxylamine hydrochloride (NH_2OH-HCl) in acetic acid (4.4 mol·l^{-1}, 25 %), hereafter referred to as HH, to reduce Fe and Mn to their soluble states.

In a first step, five samples (PS2837-5/213, 390, 623, 668, and 789) were chosen to be analyzed by ICP-MS for their rare earth element (REE) abundances in bulk sample, the extracted Fe-Mn component, and the leaching residue. The applied leaching protocol using 1 mol·l^{-1} HH closely follows a method presented in Bayon et al. (2002). 1 mol·l^{-1} HH solution was prepared by mixing 69.49 g hydroxylamine hydrochloride salt with 250 ml glacial acetic acid and purified water (18 MΩ resistivity, hereafter referred to as 18 MΩ water) to make one liter of solution. Aliquots of approximately 200 mg freeze-dried bulk sample were accurately weighed and transferred to precleaned 15 ml PP centrifuge tubes. To these, 10 ml of the 1 mol·l^{-1} HH solution were added, resulting in a reagent-to-solid sample ratio of 50 ml : 1 g. Two samples were additionally leached with a reagent-to-solid

sample ratio of 100 ml : 1 g (213/2 and 623/2). For this, second aliquots of approximately 40 mg were mixed with 4 ml of 1 mol·l^{-1} HH. Following a thorough mixing of sample and reactive agent with a vortex mixer, the centrifuge tubes were placed in a drying cabinet set to 90 °C. After three hours, during which they had been manually agitated every 30 minutes, the tubes were removed from the drying cabinet and centrifuged for seven minutes at 3000 r.p.m.. The clear supernatants were decanted into 15 ml teflon vessels, the centrifuge tubes were filled with 4 ml of 18 MΩ water, thoroughly shaken, centrifuged as above, and decanted into the same teflon vessels. To destroy excess HH, 1 ml of HNO$_3$ (16 mol·l^{-1}) was added to the leachates, which were left to react for a few minutes, taken to dryness under an infrared (IR) lamp, and dissolved in 1 ml of HCl (2.5 mol·l^{-1}). The solid residues of the leaching procedure were repeatedly washed with 18 MΩ water, taken to dryness, and weighed.

At first it was attempted to determine the mass of the extracted Fe-Mn component, necessary for the calculation of absolute REE abundances, by weighing the dried leachate and subtracting the excess mass related to the dried residue of the reagent. This, however, yielded inconsistent results. Instead, the mass differences between unleached bulk samples and solid residues were used. As this approach includes all possible loss of material during the leaching process, the determined leachate masses are maximum estimates.

Different sequential sediment leaching methods (see Bayon et al., 2002, and references therein) aim at the extraction of a pure detrital component. To achieve this, these methods employ a leaching procedure of a strength and duration sufficient to quantitatively remove the authigenic Fe-Mn component. This, however, entails the possibility of attacking detrital minerals, which would render the Fe-Mn leachate useless as a proxy of seawater composition. In contrast, no quantitative leaching is necessary for the determination of the isotopic composition of the authigenic Fe-Mn component. The leaching can therefore be split into a first step, weak enough so that no attacking of detrital minerals occurs, and, if desired, a second step strong enough to quantitatively remove all Fe-Mn oxides/hydroxides.

The 'weak leach' approach was used for the nine samples chosen to be analyzed for the Nd isotopic compositions of their leachable Fe-Mn components (PS2837-5/133, 213, 337, 374, 390, 447, 601, 623, and 789). Buffered 0.87 mol·l^{-1} acetic acid and 0.2 mol·l^{-1} HH were used as reagents. 0.87 mol·l^{-1} acetic acid buffered to pH 5 was made by mixing 50 ml of glacial acetic acid with 124 g of sodium acetate salt and 18 MΩ water to a volume of one liter. 0.2 mol·l^{-1} HH solution was prepared by mixing 13.90 g hydroxylamine hydrochloride salt with 250 ml glacial acetic acid and 18 MΩ water to make one liter of solution. To yield sufficient Nd for mass spectrometric analyses, aliquots of approximately 1 g of freeze dried bulk sample were used. The samples were mixed with 5 ml of buffered acetic acid in precleaned 15 ml PP centrifuge tubes, agitated with a vortex mixer, left to react for 12 hours, and centrifuged for 20 minutes at 1200 r.p.m., after which the supernatants were

discarded. Remaining acetic acid was removed from the solid residues by three cycles of rinsing with 18 MΩ water and centrifuging. The samples were then mixed with 6 ml of 0.2 mol·l^{-1} HH (equivalent to a reagent-to-solid sample ratio of 1.2 ml : 1 g with 1 mol·l^{-1} HH), agitated with a vortex mixer, and placed in an ultrasonic bath (with additional agitation every 30 minutes). After two and a half hours, the samples were centrifuged for 30 minutes at 2000 r.p.m. and the supernatants were transferred to weighed 15 ml teflon vessels. The centrifuge tubes were refilled with 2 ml of 18 MΩ water, agitated with a vortex mixer, centrifuged as above, and the supernatants added to the first extracts. Excess HH was destroyed by reaction with 0.5 ml HNO$_3$ (16 mol·l^{-1}). The leachates were taken to dryness, dissolved in 1 ml HCl (2.5 mol·l^{-1}), transferred to 1.5 ml PP centrifuge tubes, centrifuged for 10 minutes at 15 000 r.p.m., and were then ready for chemical separation as described in Chapter 2.2.5.

. .   S

A sequential leaching experiment was performed to explore questions raised by the analytical results for samples that were leached as described in the previous Chapter.

Four aliquots of freeze dried bulk sample PS2837-5/712 (#2, #3, #4, #6, approximately 100 mg each) were weighed into cleaned 15 ml PP centrifuge tubes. Aliquots #2, #3, and #4 were mixed with 5 ml of buffered 0.87 mol·l^{-1} acetic acid and left to react for 18 hours at 40 °C. Aliquot #6 was mixed with 5 ml of unbuffered 1.7 mol·l^{-1} acetic acid and left to react for 18 hours at room temperature. All centrifuge tubes were occasionally agitated with a vortex mixer. After 18 hours, the samples were centrifuged for 20 minutes at 1200 r.p.m. and the supernatants were pipetted into Savillex beakers. The supernatant from aliquot #6 (labeled #6/1st HOAc) was dried and stored for analysis by isotope dilution TIMS. The solid residues of aliquots #2, #3, and #4 were washed with 18 MΩ water (and centrifuged) three times. The solid residue of aliquot #2 was dried, weighed, and stored for analysis, while the solid residues of aliquots #3 and #4 were put aside for further leaching. The solid residue of aliquot #6 was subjected to a second acetic acid leaching identical to the first one. It was then centrifuged as above, and the supernatant was transferred to a Savillex beaker, dried, and stored for analysis (labeled #6/2nd HOAc). The solid residue was washed three times and put aside for further leaching.

In a second step, the solid residues of aliquots #3, #4, and #6 were mixed with 5 ml of 0.2 mol·l^{-1} HH and left to react for two hours at room temperature, with occasional agitation. They were then centrifuged for 30 minutes at 1200 r.p.m. and the supernatants were pipetted into Savillex beakers. The leachates were first taken to dryness, and then dissolved in 1 ml HNO$_3$ (16 mol·l^{-1}) to destroy excess HH. The leachates from aliquots #4 and #6 (labeled #4/1st HH and #6/1st HH) were dried again and stored for analysis. The

solid residue from aliquot #6 was washed three times, dried, weighed, and stored for analysis. The solid residues from aliquots #3 and #4 were subjected to a second cycle of HH leaching as described above, but lasting for 5:45 hours. They were then centrifuged and the supernatants were transferred to Savillex beakers, dried, and redissolved in 16 mol·l⁻¹ HNO₃. The leachate from aliquot #4 (labeled #4/2ⁿᵈ HH) was dried and stored for analysis. The solid residue from aliquot #3 was washed three times, dried, weighed, and stored for analysis. The solid residue from aliquot #4 was subjected to a third HH leaching, lasting for 20 hours. The leachate was treated as above, labeled as #4/3ʳᵈ HH, and stored for analysis. The solid residue was washed three times, dried, weighed, and stored for analysis. All leachates stored for analysis were spiked with a mixed ^{149}Sm − ^{150}Nd tracer solution for the determination of Sm and Nd concentrations by isotope dilution (see below), dissolved in 1 ml HCl (2.5 mol·l⁻¹), transferred to 1.5 ml PP centrifuge tubes, centrifuged for 10 minutes at 15 000 r.p.m., and were then ready for chemical separation as described in Chapter 2.2.5.

. . S TIMS

Sample digestion: All acids were either of Suprapur® grade (HClO₄, H₃PO₄) or purified by sub-boiling distillation (HCl, HF, HNO₃). Between 25 mg and 100 mg of finely ground sample were spiked with an adequate amount (see discussion in Chapter 2.3.1) of a mixed ^{149}Sm − ^{150}Nd tracer solution for the determination of Sm and Nd concentrations by isotope dilution. The samples were digested in closed Savillex® teflon vessels placed on a hot plate, using a mixture of 1 ml HF (23 mol·l⁻¹) and approx. 0.1 ml HClO₄ (12 mol·l⁻¹). Upon complete dissolution, SiF₄ and excess HClO₄ were fumed off at high temperature. The resulting sample cakes were repeatedly dissolved in HCl (6.1 mol·l⁻¹) and evaporated to dryness (2-3×), dissolved in 1 ml HCl (2.5 mol·l⁻¹), transferred to 1.5 ml PP centrifuge tubes, and centrifuged for 10 minutes at 15 000 r.p.m. to remove solid particles from the sample solution. These sample solutions were ready for chemical separation of the elements by ion exchange chromatography.

During the course of this study it became obvious that the aforementioned removal of organic matter with a 3.3 mol·l⁻¹ solution of H₂O₂ was not in all cases complete. In particular, several clay samples contained trace amounts of organic matter, visible as minute black specks after the first uptake in HCl (6.1 mol·l⁻¹). The presence of these organic particles presents two problems. First, they hinder the formation of a uniform sample cake during evaporation (Fig. 16). Propelled by electrostatic forces, sample material can then 'jump' out of the teflon vessel, leading to a loss of sample and a possible contamination of other samples. Second, the organic particles tend to get 'burned' into the teflon vessel, making an abrasive cleaning procedure necessary that is time consuming and potentially hazardous to the smooth inner surface of the beaker.
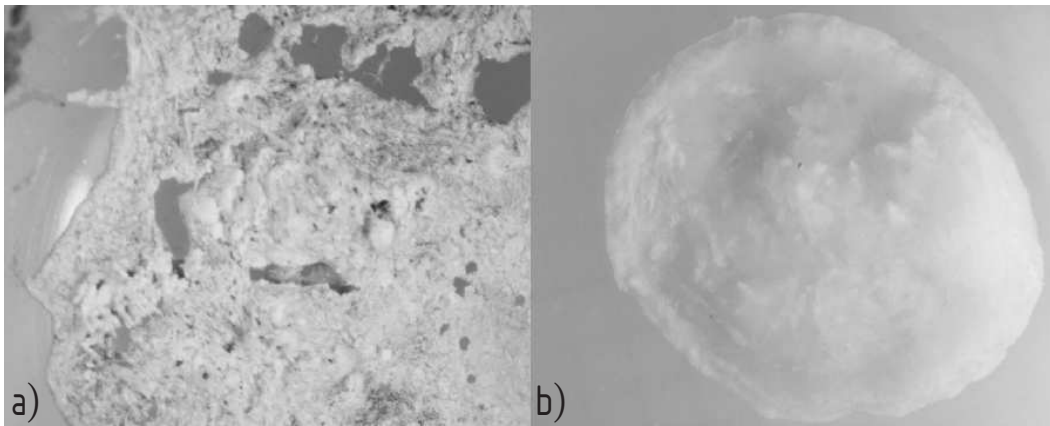
Figure 16 : Two aliquots of sample 390 c in teflon beakers after digestion in a HF - HClO$_4$ mixture and drying on a hot plate. Prior to digestion aliquot **a**) had been treated with H$_2$O$_2$ to destroy organic components; aliquot **b**) had additionally been baked for one hour at 650 °C. Horizontal field of view is 9 mm each.

A solution to this problem is the complete removal of organic matter by baking at high temperature, as has been experimentally verified. An aliquot of sample PS2837-5/390 c ('c' = clay fraction) was baked in a muffle furnace at 650 °C for one hour, resulting in a weight loss of 9.4 %. This baked aliquot was then subjected to the normal digestion procedure, parallel to an unbaked aliquot. Fig. 16 shows both aliquots after the first evaporation; the success of the baking procedure is clearly visible. Upon uptake in HCl (6.1 mol·l^{-1}), the unbaked aliquot contained several black particles, while the beaker with the baked aliquot contained a perfectly clear solution. Routine baking of samples expected to contain organic material should therefore be considered for the sample preparation protocol.

Chemical separation: The separation of the light REE (LREE) from the sample matrix was performed on 5 ml quartz glass columns filled with Dowex® AG 50W 12X cation exchange resin (2.5 mol·l^{-1} HCl and 6.1 mol·l^{-1} HCl as eluents, see Table 2a for the elution protocol). Minor traces of the resin, washed out of the column during the elution process, were destroyed by reacting the dried LREE cut with HNO$_3$ (16 mol·l^{-1}). Nd and Sm were separated from the LREE with the so called reverse phase method, where the REE are eluted in the order of increasing atomic number (Richard et al., 1976). This order of elution, in combination with the sharp elution fronts (Fig. 17), is very effective at removing the isobaric Sm interference on ^{144}Nd. Ce, which, due to the long elution tails, can be present in the Nd cut, presents a problem only if ^{142}Nd is to be accurately measured. Nd and Sm cuts were obtained with 2 ml quartz glass columns filled with HDEHP (hexyl di-ethyl hydrogen phosphate) coated teflon powder, using 0.18 mol·l^{-1} and 0.4 mol·l^{-1} HCl as eluents (see

Table 2b). 2 µl of H_3PO_4 (0.21 mol·l^{-1}) were added to the Nd and Sm cuts, which, after drying, were ready for mass spectrometric analysis.
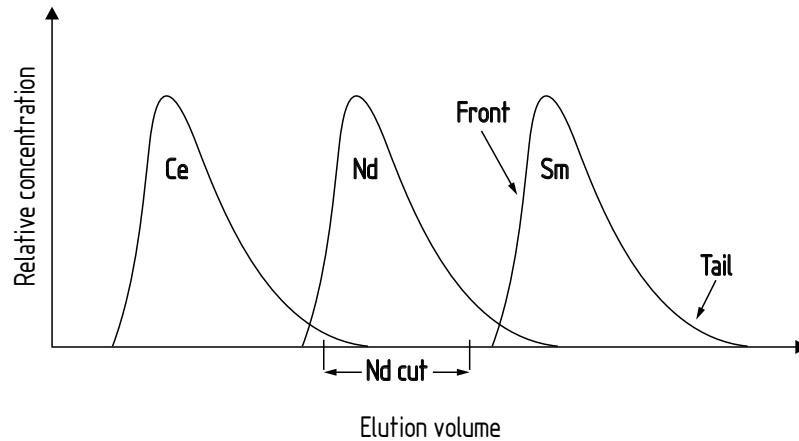
Figure 17 : Schematic elution profiles of LREE from a reverse phase HDEHP column, showing sharp fronts and long tails. Redrawn from Dickin (1995).

Table 2 : Elution protocols for (**a**) 5 ml columns and (**b**) 2 ml columns.

(**a**) 5 ml columns

Equilibrate	5 ml	HCl (2.5 mol·l^{-1})
Equilibrate	5 ml	
Equilibrate	5 ml	
Load sample	1 ml	
Rinse	1 ml	
Rinse	1 ml	
Discard	38 ml	
Collect Sr	7 ml	
Discard	5 ml	HCl (6.1 mol·l^{-1})
Collect LREE	15 ml	
Wash	15 ml	
Wash	15 ml	
Wash	15 ml	

(**b**) 2 ml columns

Equilibrate	2 ml	HCl (0.18 mol·l^{-1})
Equilibrate	2 ml	
Equilibrate	2 ml	
Load sample	0.3 ml	
Rinse	0.2 ml	
Rinse	0.2 ml	
Rinse	0.2 ml	
Rinse	0.2 ml	
Discard	10 ml	
Collect Nd	8 ml	
Discard	4 ml	HCl (0.4 mol·l^{-1})
Collect Sm	4 ml	
Wash	15 ml	HCl (6.1 mol·l^{-1})
Wash	15 ml	
Wash	15 ml	

. .   S   ICP-MS

For the determination of REE abundances at the European Union Large Scale Geochemical Facility at the University of Bristol, England, three types of samples were prepared: untreated bulk sample, leached Fe-Mn oxides/hydroxides, and solid residue from the leaching procedure. All samples were prepared at Bristol, following their ICP-MS laboratory protocol using Aristar-grade acids.

For the bulk samples, 200 mg aliquots were digested in a mixture of 5 ml HF (23 $mol \cdot l^{-1}$), 2.5 ml HNO_3 (16 $mol \cdot l^{-1}$), and 1 ml $HClO_4$ (12 $mol \cdot l^{-1}$) in open 50 ml teflon beakers on a hot plate set to 150 °C. Upon complete dissolution, the temperature was raised to 230 °C and the contents of the beakers were taken to near dryness. The sample cakes were then dissolved in 20 ml HNO_3 (0.16 $mol \cdot l^{-1}$), transferred to a volumetric flask, and diluted with HNO_3 (0.16 $mol \cdot l^{-1}$) to a total volume of 100 ml.

The residues of the leaching procedure described above were prepared in a similar fashion, only that all available sample material was used (ranging between 37 and 202 mg), and that they were diluted to a total volume of 50 ml.

The leachable Fe-Mn oxides/hydroxides, dissolved in 1 ml HCl (2.5 $mol \cdot l^{-1}$), were taken to dryness on a hot plate, dissolved in 20 ml HNO_3 (0.16 $mol \cdot l^{-1}$), and diluted with HNO_3 (0.16 $mol \cdot l^{-1}$) to a total volume of 50 ml.

For analysis, 5 ml of sample solution were mixed with 5 ml of a 20 $ng \cdot g^{-1}$ Re-Ru solution, resulting in sample dilution factors of 1000 for the bulk samples, between 500 and 5000 for the leaching residues, and between 1800 and 17000 for the leachate samples. At a sample dilution factor of e.g. 1000, 1 $ng \cdot g^{-1}$ in the measured solution equals 1 $\mu g \cdot g^{-1}$ in the solid sample.

.   D

. .   TIMS

Data collection: Sm and Nd isotope ratios were determined on two different Finnigan MAT 261 thermal ionization mass spectrometers (TIMS 1 and 2) at the Department of Earth- and Environmental Sciences, Ludwig-Maximilians-University, Munich, using double Re filament assemblies. Nd isotope ratios were determined in dynamic quadruple mass collection mode (recording a minimum of 100 cycles per run, peak integration time 8 seconds, internal normalization to $^{146}Nd/^{144}Nd = 0.7219$). Within-run precision on $^{143}Nd/^{144}Nd$ ratios was better than 12×10^{-6} ($2\sigma_m$) in most cases, and better than external precision (see below) in all cases. Sm isotope ratios were recorded in dynamic single cup mode, and were normalized to $^{147}Sm/^{152}Sm = 0.56081$.

Data reduction: Sm and Nd concentrations were determined by isotope dilution. With a highly enriched spike, such as the Munich mixed ^{149}Sm – ^{150}Nd tracer solution, it is possible to determine element concentration and isotope ratios from a single mass spectrometric analysis of a sample–spike mixture (hereafter referred to as IC-ID analysis). For this, a so-called double isotope dilution is performed, which includes a correction of the natural isotope ratios for spike contribution. The levels of precision and accuracy that can be achieved in an IC-ID analysis largely depend on the composition of the spike, the knowledge thereof, and the sample-to-spike ratio in the analyzed mixture.

Ideal conditions for IC-ID analysis would be met with a truly monoisotopic spike, with the spike isotope being one that is of no interest for the determination of relevant isotope ratios. However, since truly monoisotopic spikes are not available, the addition of spike to the sample introduces added uncertainty to the determination of isotope ratios. This added uncertainty has two sources. The first source is the uncertainty in the determination of the isotopic composition of the spike itself, because, due to the lack of a known natural isotope ratio, mass fractionation during the mass spectrometric analysis of the pure spike can generally not be accurately corrected. Note, however, that the so-called 'critical mixture' method allows to circumvent the problem of mass fractionation under certain conditions (see Roddick et al., 1992, and references therein).

The second source of uncertainty is the mass fractionation correction of the analyzed sample–spike mixture. In the case of Nd, the true ^{146}Nd/^{144}Nd ratio of the mixture is unknown at the time of mass spectrometric analysis. Instead, the natural ^{146}Nd/^{144}Nd ratio of 0.7219 is used for correction, resulting in an incorrect normalization. This incorrect normalization—which may be named 'fractionation offset'—has to be accounted for in a second-order correction. Since the accuracy of all commonly used normalization laws (based on empiric evidence, e.g. linear, exponential, etc.) is inversely related to the magnitude of fractionation, it is desirable to keep the fractionation offset at a minimum. Depending on the isotopic composition of the spike, the magnitude of the fractionation offset is proportional to the amount of spike in the analyzed mixture (Fig. 18). For the determination of isotope ratios, the amount of spike in the mixture should therefore be as small as possible.

In contrast, optimum precision on the determination of the Nd concentration is attained at a significantly different amount of spike in the mixture. The precision on the concentration is determined by the precision with which the amount of spike in the mixture, i.e. the ^{150}Nd/^{144}Nd ratio of the mixture, can be determined. The statistic, mass spectrometric uncertainty on an isotope ratio is increased by a magnification factor depending on the total sample–to–spike number of atoms ratio q (De Bievre and Debus, 1965). For a given isotopic composition of the spike, this magnification factor can be calculated as a function of the sample–spike ratio. Fig. 19 shows the result of this calculation for the

Figure 18: The ^{146}Nd/^{144}Nd ratio of a sample–spike mixture as a function of its ^{150}Nd/^{144}Nd ratio (calculated for the Munich ^{150}Nd tracer solution). The true ^{146}Nd/^{144}Nd ratio of the mixture is unknown at the time of the mass spectrometric analysis. Instead, the natural ^{146}Nd/^{144}Nd ratio of 0.7219 is used for correction, resulting in an incorrect normalization. This incorrect normalization—which may be named 'fractionation offset'—has to be accounted for in a second-order correction. It can be seen that the fractionation offset is small for the chosen ^{150}Nd/^{144}Nd ratio of 0.6, keeping the extra uncertainty introduced by the second-order mass fractionation correction small. See text for discussion.

Munich mixed ^{149}Sm – ^{150}Nd spike; as can be seen, error magnification is low for a wide range of ^{150}Nd/^{144}Nd ratios in the mixture. Although the absolute uncertainty cannot be determined mathematically, a suitable compromise between error magnification and fractionation offset can be found by choosing an appropriate sample–spike ratio.

Data presentation: Nd isotopic compositions, i.e. ^{143}Nd/^{144}Nd ratios, are expressed as ε_{Nd} values (DePaolo and Wasserburg, 1976), representing the ' in parts per 10^4 ' deviation of a sample's ^{143}Nd/^{144}Nd ratio from the chondritic uniform reservoir (CHUR) at time t, calculated as:

$$\varepsilon_{Nd}(t) = \left(\left[\left(^{143}Nd/^{144}Nd \right)_{Sample}(t) \middle/ \left(^{143}Nd/^{144}Nd \right)_{CHUR}(t) \right] - 1 \right) \times 10^4$$
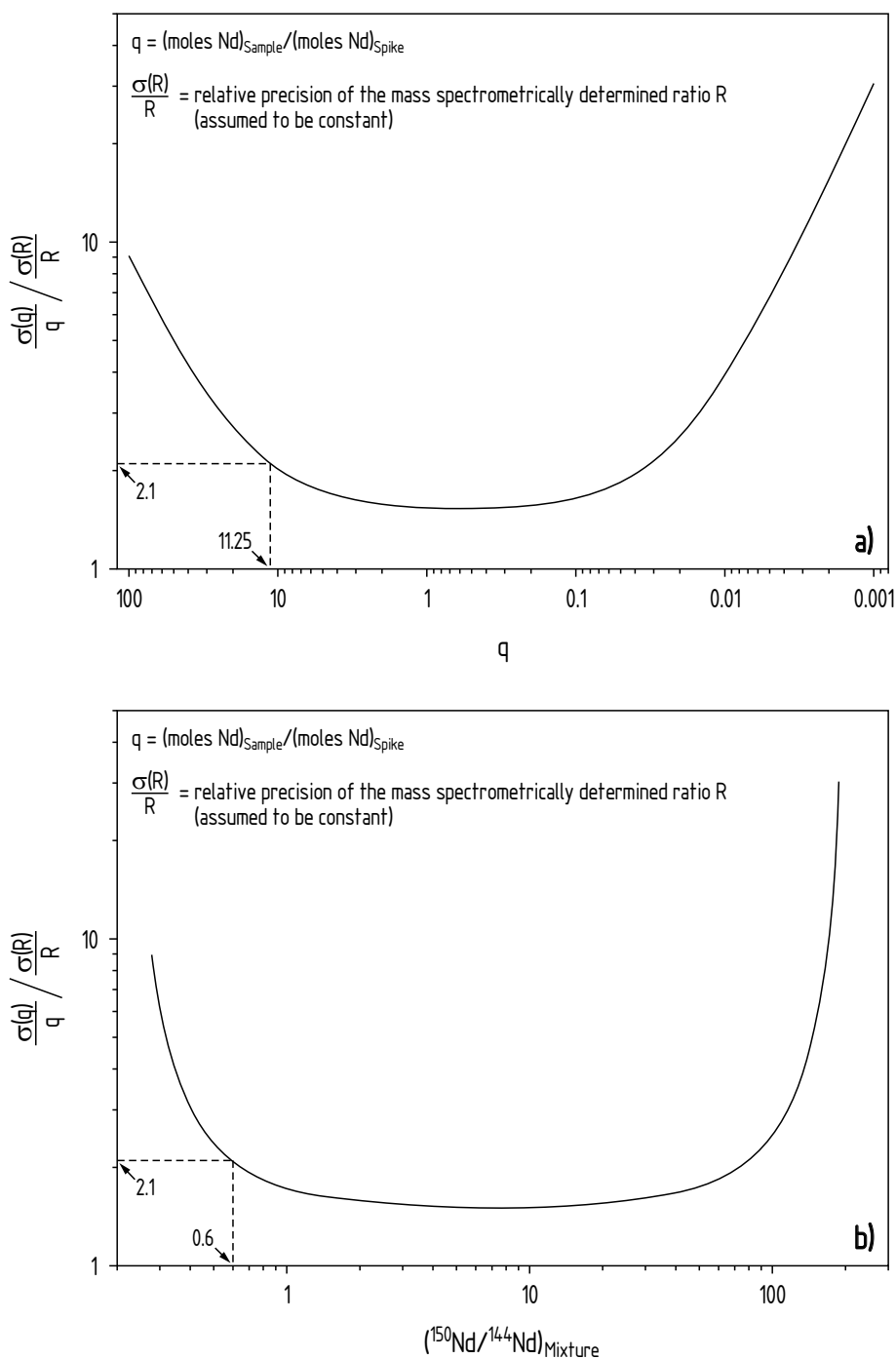
Figure 19: Magnification of the relative uncertainty on the sample–to–spike number of atoms ratio q as a function of q (**a**), and the ^{150}Nd/^{144}Nd ratio (**b**) of the mixture. Calculated for the Munich ^{150}Nd tracer solution, after De Bievre and Debus (1965). Although the error magnification is at a minimum for $q = 0.6$ (^{150}Nd/^{144}Nd$_{mixture}$ = 7), we aim at $q = 11.25$ (^{150}Nd/^{144}Nd$_{mixture}$ = 0.6). See text for discussion.

All given ε_{Nd} values were calculated for $t = 0$, with present-day $^{143}Nd/^{144}Nd_{CHUR} = 0.512638$ (Jacobsen and Wasserburg, 1980).

Depleted mantle model ages T_{DM} were calculated according to the model of Goldstein et al. (1984), based on linear evolution of the depleted mantle from a CHUR composition at 4.5 Ga.

$$T_{DM} = \left(\frac{1}{\lambda}\right) \times \ln \left(1 + \left[\left(^{143}Nd/^{144}Nd\right)_{Sample} - \left(^{143}Nd/^{144}Nd\right)_{DM}\right. \right./ $$
$$\left.\left. \left(^{147}Sm/^{144}Nd\right)_{Sample} - \left(^{147}Sm/^{144}Nd\right)_{DM}\right]\right)$$

with $^{147}Sm/^{144}Nd_{DM} = 0.2136$, $^{143}Nd/^{144}Nd_{DM} = 0.513151$, and $\lambda^{147}Sm = 6.54 \times 10^{-12}$ (Goldstein and Jacobsen, 1988).

. .   ICP-MS

REE abundances in bulk samples, leached Fe-Mn oxides/hydroxides, and solid leaching residues were determined at the European Union Large Scale Geochemical Facility at the University of Bristol, England, using a VG Elemental Plasma Quad II ICP-MS. The analyses were carried out by T. Kemp and C. Choi. Re and Ru (10 ng·g^{-1}) were used as internal standards to correct for instrument drift. Analytical blanks and silicate reference materials (see Table 8) were analyzed with the natural samples.

.   Q   TIMS

. .   B

Measured whole-procedure blanks for Nd (Table 3) show a tenfold increase over the period of this study, pointing to deteriorating quality of the elution columns. However, blank levels are at least three orders of magnitude lower than Nd contents in the analyzed aliquots of the natural samples under investigation, and are therefore negligible.

Table 3: Procedure Nd blanks determined during this study.

Date	$^{149}Sm-^{150}Nd$ tracer	measured $^{150}Nd/^{144}Nd$	Nd blank
2000/12/21	23.36 mg	165.59	70 pg
2003/02/22	13.63 mg	74.10	360 pg
2004/03/17	25.29 mg	74.11	660 pg

. . I - N

Repeated measurements of the Munich in-house isotope standard Ames Nd metal yielded means of ^{143}Nd/^{144}Nd = 0.512 138 ± 23×10^{-6} (2σ, n = 11, TIMS 1, Table 4) and ^{143}Nd/^{144}Nd = 0.512 141 ± 15×10^{-6} (2σ, n = 34, TIMS 2, Table 5), corresponding to ^{143}Nd/^{144}Nd values of 0.511 850 and 0.511 853, respectively, for the La Jolla Nd standard. For reasons of consistency the higher value of ± 23×10^{-6}, corresponding to ± 0.5 ε_{Nd} values, is applied to all data as external reproducibility.

Table 4 : Reproducibility of the Nd isotopic composition of the Munich in-house standard Ames Nd metal with TIMS 1.

^{143}Nd/^{144}Nd [†]	Operator	Date		^{143}Nd/^{144}Nd [†]	Operator	Date
1.	0.512 130 ± 09	WOS	2000/12/18	7.	0.512 124 ± 10	WOS	2001/02/26
2.	0.512 143 ± 12	WOS	2000/12/19	8.	0.512 137 ± 14	WOS	2001/02/27
3.	0.512 161 ± 15	WOS	2001/01/10	9.	0.512 121 ± 11	WOS	2001/02/28
4.	0.512 139 ± 15	MWI	2001/01/11	10.	0.512 143 ± 22	WOS	2001/03/20
5.	0.512 135 ± 10	WOS	2001/01/12	11.	0.512 148 ± 11	WOS	2001/03/21
6.	0.512 132 ± 11	WOS	2001/01/19	Mean:	0.512138 ± 23 (2σ)		

^{143}Nd/^{144}Nd ratios are normalized to ^{146}Nd/^{144}Nd = 0.7219. [†] Within-run precision (2σ$_m$) refers to the last significant digits. WOS: W. Schmitt, MWI: M. Willbold.

. . R

Repeated measurements of the United States Geological Survey (USGS) reference materials BCR-1 and BCR-2 (Table 6)—which have been shown to be very similar in composition (Raczek et al., 2001, 2003)—yielded combined means of 6.43 µg·g^{-1} Sm, 28.3 µg·g^{-1} Nd, and ^{143}Nd/^{144}Nd = 0.512 633 ± 17×10^{-6} (2σ, n = 4). These results correspond well to published values (Raczek et al., 2001, 2003, and references therein).

. . R

Replicate measurements, using separate sample aliquots, have been performed for twelve natural samples from this study (Table 7). Eight samples have been repeated as unspiked runs (PS2837-5/487 sa, BP01/72 c, and the six Spitsbergen samples). Their ^{143}Nd/^{144}Nd ratios agree with the results from the original measurements to within ± 18.5×10^{-6}, which is better than the assumed external reproducibility of ± 23×10^{-6}. Four samples from core PS2837-5, comprising two clays, one coarse silt, and one sand, have been repeated as spiked runs. The ^{143}Nd/^{144}Nd ratios of three of these replicates agree with the original results to within ± 17×10^{-6}. The replicate of the sand from PS2837-5/623, however, differs by

Table 5 : Reproducibility of the Nd isotopic composition of the Munich in-house standard Ames
Nd metal with TIMS 2.

	^{143}Nd/^{144}Nd [†]	Operator	Date		^{143}Nd/^{144}Nd [†]	Operator	Date
1.	0.512 143 ± 15	WOS	2002/11/14	18.	0.512 144	HEG	2004/03/25
2.	0.512 144 ± 16	WOS	2003/02/20	19.	0.512 128	HEG	2004/03/25
3.	0.512 140 ± 18	WOS	2003/04/07	20.	0.512 143	HEG	2004/03/26
4.	0.512 140 ± 12	MWI	2003/08/25	21.	0.512 147	HEG	2004/03/26
5.	0.512 144 ± 11	MWI	2003/08/26	22.	0.512 149	HEG	2004/03/26
6.	0.512 148 ± 10	MWI	2003/08/28	23.	0.512 144	HEG	2004/03/27
7.	0.512 138 ± 10	HEG	2003/12/26	24.	0.512 149	HEG	2004/03/27
8.	0.512 142 ± 15	WOS	2004/02/19	25.	0.512 147	HEG	2004/03/27
9.	0.512 141 ± 09	WOS	2004/02/22	26.	0.512 129	HEG	2004/03/28
10.	0.512 141 ± 10	WOS	2004/03/18	27.	0.512 140	HEG	2004/03/28
11.	0.512 149	HEG	2004/03/23	28.	0.512 142 ± 13	WOS	2004/04/25
12.	0.512 146	HEG	2004/03/23	29.	0.512 129 ± 10	ARO	2004/09/14
13.	0.512 144	HEG	2004/03/23	30.	0.512 130 ± 10	ARO	2004/09/20
14.	0.512 146	HEG	2004/03/23	31.	0.512 153 ± 13	ARO	2004/09/21
15.	0.512 136	HEG	2004/03/24	32.	0.512 138 ± 08	ARO	2004/09/21
16.	0.512 129	HEG	2004/03/24	33.	0.512 135 ± 13	ARO	2004/09/22
17.	0.512 124	HEG	2004/03/24	34.	0.512 155 ± 11	WOS	2005/01/17
				Mean:	0.512141 ± 15 (2σ)		

^{143}Nd/^{144}Nd ratios are normalized to ^{146}Nd/^{144}Nd = 0.7219. [†] Within-run precision ($2\sigma_m$) refers to the last significant digits. WOS: W. Schmitt, MWI: M. Willbold, HEG: E. Hegner, ARO: A. Rocholl.

Table 6 : Sm and Nd concentrations and isotopic compositions of USGS reference materials BCR-1 and BCR-2.

Sample	Sm ($\mu g \cdot g^{-1}$)	Nd ($\mu g \cdot g^{-1}$)	Sm/Nd	^{143}Nd/^{144}Nd [†]	ε_{Nd}	T_{DM} (Ga)	Date
BCR-1, 60/20	6.56	28.7	0.2286	0.512 637 ± 11	0.0	1.04	2003/04/11
BCR-1, 46/16	6.51	28.4	0.2292	0.512 639 ± 12	0.0	1.04	2003/04/12
BCR-2	6.41	28.0	0.2289	0.512 618 ± 12	-0.4	1.08	2004/03/17
BCR-2	6.43	28.1	0.2288	0.512 638 ± 16	0.0	1.04	2004/12/13
Mean	6.48	28.3	0.2289	0.512 633	-0.1	1.05	
2σ	0.12	0.5	0.0004	0.000017	0.3	0.03	

^{143}Nd/^{144}Nd ratios are normalized to ^{146}Nd/^{144}Nd = 0.7219. [†] Within-run precision ($2\sigma_m$) refers to the last significant digits. ε_{Nd} calculated according to DePaolo and Wasserburg (1976), with present-day ^{143}Nd/^{144}Nd$_{CHUR}$ = 0.512 638 (Jacobsen and Wasserburg, 1980). T_{DM} calculated according to the depleted mantle model of Goldstein et al. (1984), using ^{147}Sm/^{144}Nd$_{DM}$ = 0.2136, ^{143}Nd/^{144}Nd$_{DM}$ = 0.513 151, and λ^{147}Sm = 6.54×10^{-12} (Goldstein and Jacobsen, 1988).

Table 7 : Results of replicate measurements of natural samples.

Sample	Size fraction (μm)	Sm (μg·g⁻¹)	Nd (μg·g⁻¹)	Sm/Nd	^{143}Nd/^{144}Nd [†]	ε_{Nd}	T_{DM} (Ga)
487 sa	63-250	2.54	13.5	0.1881	0.512 098 ± 11	-10.5	1.60
487 sa re.					0.512 061 ± 13	-11.3	
					Δ = 0.000 037		
BP01/72 c	< 2	6.15	30.8	0.1997	0.512 281 ± 11	-7.0	1.42
BP01/72 c re.					0.512 273 ± 26	-7.1	
					Δ = 0.000 008		
WoA	< 63	6.09	32.6	0.1868	0.511 732 ± 12	-17.7	2.14
WoA re.					0.511 727 ± 13	-17.8	
					Δ = 0.000 005		
WoF	< 500	3.05	15.8	0.1930	0.511 876 ± 13	-14.9	2.00
WoF re.					0.511 888 ± 13	-14.6	
					Δ = 0.000 012		
WoG	< 500	1.63	8.76	0.1861	0.511 840 ± 12	-15.6	1.98
WoG re.					0.511 862 ± 13	-15.1	
					Δ = 0.000 022		
WoC	< 63	7.88	40.2	0.1960	0.511 987 ± 12	-12.7	1.86
WoC re.					0.512 000 ± 12	-12.4	
					Δ = 0.000 013		
WoD	< 63	8.68	47.0	0.1847	0.511 929 ± 12	-13.8	1.82
WoD re.					0.511 949 ± 14	-13.4	
					Δ = 0.000 020		
WoE	< 63	7.82	41.3	0.1893	0.511 966 ± 12	-13.1	1.82
WoE re.					0.511 986 ± 10	-12.7	
					Δ = 0.000 020		
55 c	< 2	7.11	37.9	0.1876	0.512 032 ± 10	-11.8	1.70
55 c re.		6.93	36.9	0.1878	0.512 022 ± 10	-12.0	1.72
					Δ = 0.000 010		
390 c	< 2	7.82	42.8	0.1827	0.511 887 ± 10	-14.6	1.87
390 c re.		7.99	43.7	0.1828	0.511 893 ± 11	-14.5	1.85
					Δ = 0.000 006		
623 sa	63-250	2.13	11.2	0.1902	0.512 103 ± 10	-10.4	1.61
623 sa re.		1.54	8.87	0.1736	0.511 909 ± 11	-14.2	1.74
					Δ = 0.000 194		
668 cs	10-63	5.39	27.3	0.1974	0.511 946 ± 10	-13.5	1.94
668 cs re.		5.65	28.7	0.1969	0.511 980 ± 11	-12.8	1.88
					Δ = 0.000 034		

See footnote to Table 6 for details.

3.8 ε_{Nd} values from the original measurement. In analogy with a coarse-grained granite, significantly more sample material is required for a representative analysis of sand-size material than for a fine-grained clay sample (or basalt). As the amount of sand-size material available for analysis in this study was as little as 84 mg, the significance of the analytical results for sand samples is questionable. Hence they will be treated with caution.

To conclude, eleven out of twelve replicate measurements of natural samples confirm the general external reproducibility of $\pm 0.5\,\varepsilon_{Nd}$, whereas the reproducibility of sand samples may be on the order of $\pm 2\,\varepsilon_{Nd}$, perhaps even higher.

. .   P   S /N

Sm/Nd ratios determined by isotope dilution with the Munich ^{149}Sm $-$ ^{150}Nd mixed tracer solution are precise to 0.2 %, as verified against the CalTech-Sm/Nd standard solution (E. Hegner, personal communication), and confirmed by replicate measurements of natural samples and USGS reference materials BCR-1 and BCR-2 (see above).

.   Q   ICP-MS

The Bristol in-house standard 3570 and the silicate reference materials BE-N, MAG-1, JG-2, DR-N, JA-3, JB-1, and BHVO-2 were analyzed as a means of controlling the quality of ICP-MS data.

Precision (at the 1 σ level) is better than 5 % for all REE except Gd (12 %), Er (6 %), and Lu (8 %), as established by 47 measurements of the Bristol in-house standard 3570 during a period of 19 months (C. Choi, personal communication, see Table 8).

REE concentrations determined for the reference materials BE-N, JB-1, and BHVO-2 (basalts), JA-3 (andesite), and DR-N (diorite) are in good agreement with published reference values (Table 8). In contrast, the results for MAG-1 (marine mud) and JG-2 (granite) show a systematic deviation from the reference values (Table 8). For MAG-1, LREE concentrations are consistently at, or slightly above, the upper limit of the 1σ uncertainty interval, whereas heavy REE (HREE) concentrations are too low by as much as 16 %. For JG-2, LREE concentrations agree well with the reference values, whereas HREE concentrations are too low by as much as 23 %. Gromet et al. (1984) and Sholkovitz (1990) reported similar HREE depletion and a moderate LREE depletion in sediments subjected to open beaker digestion, which, as they concluded, is not suited for the accurate analysis of sediment samples. It therefore has to be assumed that the REE concentrations determined for bulk samples and leaching residues from core PS2837-5 are incorrect. The results for the leachates, however, should be unaffected.

Table 8 : REE concentrations (µg·g⁻¹) of the Bristol in-house standard 3570 and the reference materials BE-N, MAG-1, JG-2, DR-N, JA-3, JB-1, and BHVO-2, determined by ICP-MS in Bristol (Meas.), reference values (Ref.), and Meas./Ref. ratios. For 3570, the Meas. value is the mean of 6 measurements; the Ref. value is the mean of 47 measurements, carried out over a period of 19 months (personal communication C. Choi). RSD = relative standard deviation. Continued on the next page.

	3570					BE-N		
	Meas.	RSD	Ref.	RSD	Meas./Ref.	Meas.	Ref. [1]	Meas./Ref.
La	8.11	0.036	8.24	0.035	0.98	83.2	82.0	1.02
Ce	18.6	0.051	18.3	0.051	1.02	152	151	1.01
Pr	2.57	0.026	2.59	0.042	0.99	17.8	17.9	0.99
Nd	12.1	0.023	12.2	0.033	0.99	67.5	66.0	1.02
Sm	3.27	0.019	3.30	0.035	0.99	12.4	11.9	1.04
Eu	1.19	0.020	1.23	0.049	0.97	3.62	3.75	0.97
Gd	3.67	0.017	3.60	0.117	1.02	10.6	10.5	1.01
Tb	0.614	0.028	0.629	0.047	0.98	1.28	1.31	0.98
Dy	4.05	0.018	3.97	0.048	1.02	6.50	6.54	0.99
Ho	0.842	0.015	0.863	0.038	0.98	1.05	1.08	0.97
Er	2.53	0.027	2.45	0.056	1.03	2.65	2.60	1.02
Tm	0.355	0.034	0.364	0.047	0.98	0.315	0.320	0.98
Yb	2.42	0.023	2.37	0.034	1.02	1.92	1.83	1.05
Lu	0.334	0.022	0.332	0.076	1.01	0.248	0.264	0.94

	MAG-1			JG-2			DR-N		
	Meas.	Ref. [1]	Meas./Ref.	Meas.	Ref. [1]	Meas./Ref.	Meas.	Ref. [2]	Meas./Ref.
La	42.6	40.7	1.05	18.8	19.0	0.99	20.4	21.5	0.95
Ce	86.5	84.0	1.03	46.1	45.0	1.03	43.6	46.0	0.95
Pr	10.6	10.3	1.02	6.10	6.00	1.01	5.50	5.70	0.96
Nd	39.6	36.9	1.07	25.1	24.0	1.05	22.6	23.5	0.96
Sm	7.41	7.00	1.06	7.40	7.50	0.99	4.88	5.40	0.90
Eu	1.47	1.43	1.03	0.090	0.090	1.00	1.37	1.45	0.95
Gd	5.89	6.20	0.95	8.18	9.30	0.88	4.94	4.70	1.05
Tb	0.809	0.890	0.91	1.43	1.74	0.82	0.746	0.770	0.97
Dy	4.35	5.07	0.86	9.42	11.7	0.81	4.55	4.60	0.99
Ho	0.789	0.970	0.81	1.98	2.52	0.79	0.912	1.00	0.91
Er	2.28	2.73	0.84	6.35	7.80	0.81	2.58	2.50	1.03
Tm	0.314	0.393	0.80	0.942	1.22	0.77	0.373	0.390	0.96
Yb	2.16	2.53	0.86	6.74	8.10	0.83	2.46	2.50	0.98
Lu	0.326	0.381	0.86	0.976	1.21	0.81	0.360	0.400	0.90

Reference values from: [1] Dulski (2001), [2] Govindaraju (1995)

Table 8:...continued

	JA-3			JB-1			BHVO-2		
	Meas.	Ref. [1]	Meas./Ref.	Meas.	Ref. [3]	Meas./Ref.	Meas.	Ref. [4]	Meas./Ref.
La	9.11	9.30	0.98	36.7	37.4	0.98	15.1	15.2	1.00
Ce	21.3	21.6	0.99	63.7	67.4	0.94	37.9	37.5	1.01
Pr	2.78	2.90	0.96	7.11	7.08	1.00	5.37	5.29	1.01
Nd	12.2	12.1	1.01	26.1	26.3	0.99	25.0	24.5	1.02
Sm	2.94	3.00	0.98	4.90	5.06	0.97	6.20	6.07	1.02
Eu	0.784	0.770	1.02	1.44	1.48	0.97	2.03	2.07	0.98
Gd	3.20	3.40	0.94	4.68	4.66	1.00	6.07	6.24	0.97
Tb	0.492	0.530	0.93	0.691	0.640	1.08	0.901	0.936	0.96
Dy	3.16	3.30	0.96	4.11	4.09	1.01	5.28	5.31	0.99
Ho	0.653	0.670	0.98	0.769	0.810	0.95	0.961	0.972	0.99
Er	1.96	2.00	0.98	2.26	2.22	1.02	2.60	2.54	1.02
Tm	0.284	0.290	0.98	0.307	0.330	0.93	0.343	0.341	1.01
Yb	2.00	1.98	1.01	2.05	2.07	0.99	2.09	2.00	1.04
Lu	0.298	0.300	0.99	0.305	0.300	1.02	0.276	0.274	1.01

Reference values: [1] Dulski (2001), [3] Jochum and Jenner (1994), [4] Raczek et al. (2001)

R

All analytical results are given in Appendix A. Sm-Nd data for sediment core samples are presented in Table 10, and in Table 11 for modern samples. The results of ICP-MS measurements at the University of Bristol are listed in Table 12. The Nd isotopic compositions of the HH-leachable fractions of bulk samples from core PS2837-5 are listed in Table 13, and the analytical results for the sequential leaching experiment in Table 14.

.   D

As this thesis deals with a multitude of different samples and sample types, several descriptive terms are defined to avoid confusion and to simplify discussion. 'Bulk sample' refers to a sample as originally collected, without further splitting or extraction, e.g. a one-centimeter slice of sediment core. The bulk samples from the sediment cores PS2837-5 and PS2837-6 are collectively referred to as 'the core samples'. References to 'samples from core PS2837-5' always include the one sample collected from its companion box core, namely sample PS2837-6/1. Individual core samples are identified by their depth in core, e.g. PS2837-5/133 is referred to as sample 133. All samples that do not belong to the core samples are referred to as 'modern samples'. 'Grain-size fraction' refers to material belonging to a given range of grain sizes separated from a particular bulk sample, whereas 'grain-size class' makes no distinction between individual samples. Particular grain-size fractions are appended in abbreviated form to sample names: 'c' is clay (< 2 μm), 'fs' is fine silt (2-10 μm), 'cs' is coarse silt (10-63 μm), 'sil' is silt (2-63 μm), 'sa' is sand (> 63 μm); e.g. L17 cs identifies the fraction 10-63 μm of the Lena River bulk sample L17.

.   S -N   -

. .   S   N

Element abundances in the core samples range from 1.4 μg·g^{-1} to 8.5 μg·g^{-1} for Sm, and from 7.3 μg·g^{-1} to 43.7 μg·g^{-1} for Nd. Each grain-size class is characterized by a distinct range of Sm and Nd concentrations, with only a small overlap between fine silt and clay (Fig. 20a). This overlap may be a consequence of the insufficient separation of clay sized material from the fine silt fraction mentioned in Chapter 2.2.2. Due to the aforementioned problem of heterogeneity (see Chapter 2.4.4), the scatter is highest for sand fractions. The inverse correlation of Sm and Nd concentrations with grain size is in agreement with the
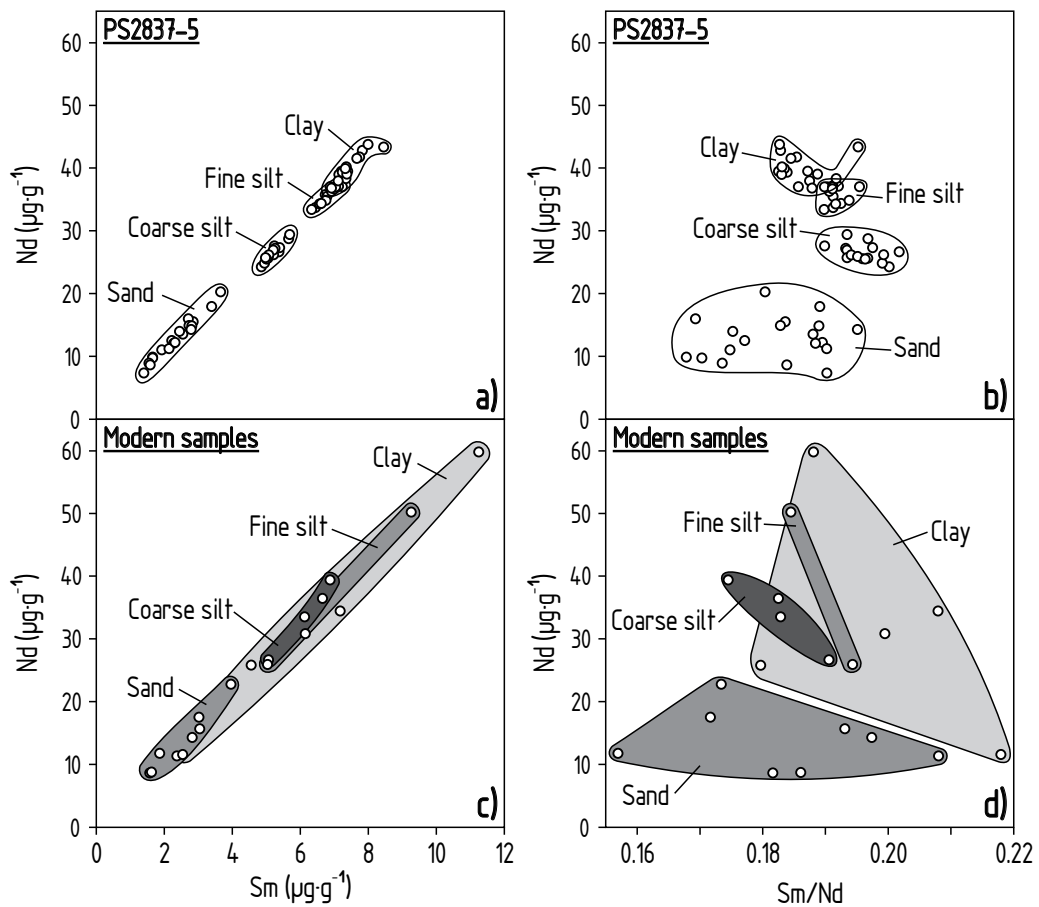
Figure 20 : Sm-Nd abundance data for analyzed grain-size fractions. (**a**) Sm vs Nd and (**b**) Sm/Nd vs Nd for grain-size fractions from sediment core PS2837-5. (**c**) Sm vs Nd and (**d**) Sm/Nd vs Nd for modern samples from the Lena, Ob, and Yenisei rivers, Spitsbergen beach deposits, and IRD from the central Fram Strait.

mineral assemblages that can generally be expected for these grain-size classes (e.g. abundant quartz in the sand fraction, mainly clay minerals in the clay fraction). Sm/Nd ratios span a small range from 0.168 to 0.201, with no clear distinction between, but relative uniformity within each of the different grain-size classes (Fig. 20b). As with Sm and Nd concentrations, the scatter in Sm/Nd ratios is highest for sand fractions.

Modern samples show higher overall variation from 1.6 µg·g^{-1} to 11.2 µg·g^{-1} for Sm, and from 8.6 µg·g^{-1} to 60 µg·g^{-1} for Nd (Fig. 20c). The variation in Sm/Nd ratios between 0.157 and 0.217 is approximately twice the range found in the core samples (Fig. 20d). In contrast to the core samples, the grain-size classes of modern samples do not fall into distinct ranges of Sm and Nd concentrations. With respect to their Sm/Nd ratios, the grain-size classes of modern samples are less uniform than those of the core samples. In Fig. 21, grain-size classes from the core samples and from the modern samples are compared in plots of
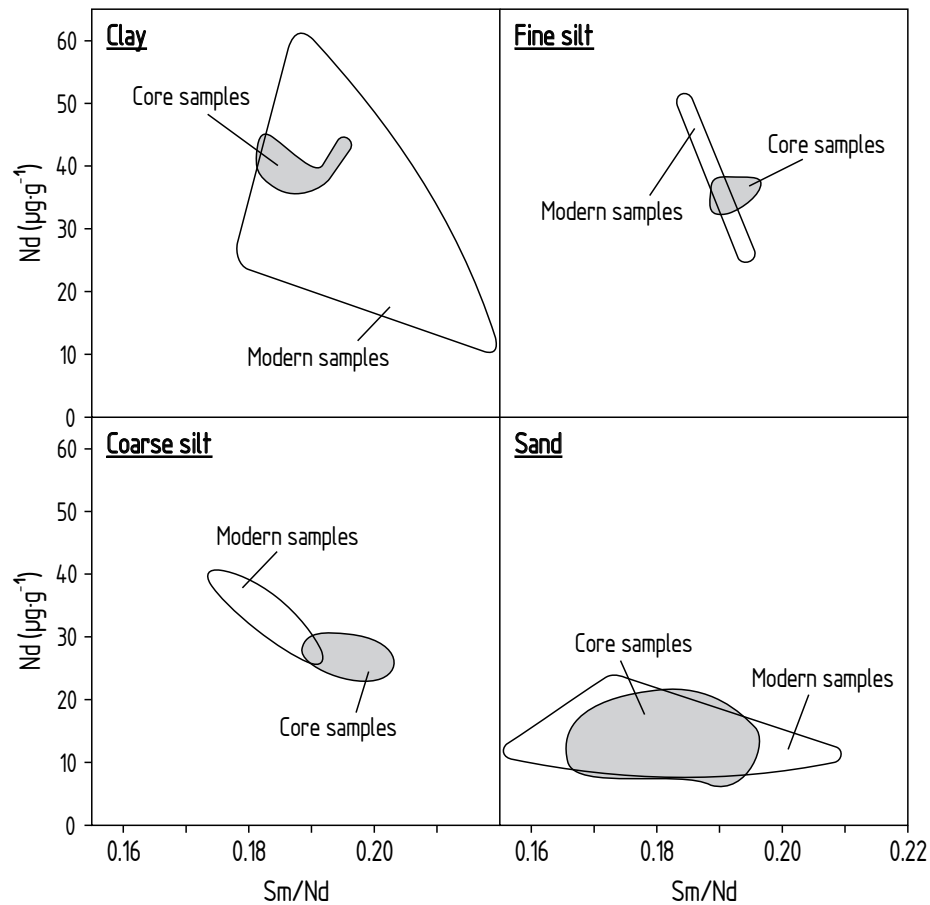
Figure 21 : Sm/Nd ratios vs Nd concentrations of grain-size classes from sediment core PS2837-5 and modern samples.

Sm/Nd ratios vs Nd concentrations. Clay in modern samples covers a much wider range of both Nd concentrations and Sm/Nd ratios than clay in the core samples, which fall within the range of the modern samples. For modern fine silt, the variations in Nd concentrations and Sm/Nd ratios exceed those for the core samples by factors of approximately five and two, respectively. Coarse silt in modern samples is different from coarse silt in the core samples. Although there is a small overlap, modern coarse silt has generally lower Sm/Nd ratios and higher Nd concentrations than coarse silt from the core samples. For sand, the variation in Sm/Nd ratios in modern samples is almost twice that in the core samples, while the variation in Nd concentrations is similar.

Despite being represented by a significantly smaller number of data points, modern samples show a much higher variation in Sm and Nd concentrations and Sm/Nd ratios than the core samples. The implication is that the core samples have a relatively uniform mineralogical composition that has changed only little during 129 ka of sedimentation.

. .   N

Nd isotopic compositions have been determined for grain-size fractions of 18 core samples. For 15 samples, all four size fractions were analyzed. For a further three samples only the sand fraction was measured. ε_{Nd} values for the core samples span a range of 5.1 units (from -9.5 to -14.6). ε_{Nd} values show no correlation with grain size (Fig. 22a), indicating that the isotopic composition is not primarily determined by mineralogical composition.

The modern samples span a range of 11.8 ε_{Nd} values (from -6.0 to -17.8). This includes samples that were analyzed as bulk, or whose grain-size fractions do not match the clay-fine silt-coarse silt-sand scheme (see Table 11 in Appendix A for analyzed size fractions). As with the core samples, ε_{Nd} values in the modern samples do not correlate with grain size. Most modern samples can be distinguished from each other on the basis of their ε_{Nd} values and Sm/Nd ratios (Fig. 22b). The least radiogenic values are found in the beach deposits from Kongsfjorden (ε_{Nd} -14.7 to -17.9) and the samples from the Lena river (ε_{Nd} -14.7 to -16.8). Although their Nd isotopic compositions overlap, the Kongsfjorden samples generally have higher Sm/Nd ratios (0.1861-0.1939) than the Lena samples (0.1568-0.1880). The Kongs-fjorden samples and the Isfjorden samples have similar Sm/Nd ratios (0.1861-0.1939 and 0.1847-0.1960, respectively), but the Nd isotopic compositions of the Isfjorden samples are distinctly more radiogenic (ε_{Nd} -12.6 to -13.6). The three grain-size fractions of the River Ob sample have ε_{Nd} values between -7 and -9.2, and Sm/Nd ratios between 0.1817 and
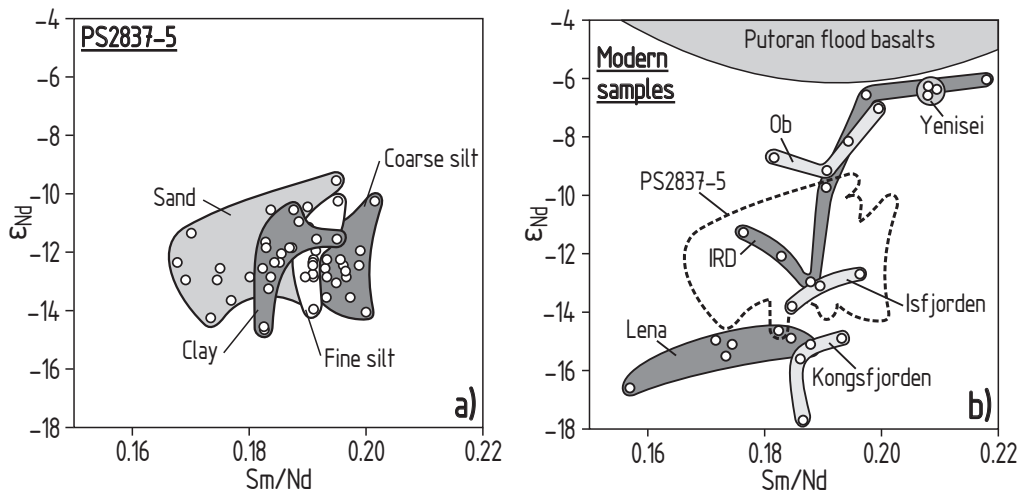
Figure 22 : Sm/Nd ratios vs ε_{Nd} values of (**a**) grain-size fractions from sediment core PS2837-5, and (**b**) modern samples (bulk and grain-size fractions) from the Lena, Ob, and Yenisei rivers, Kongsfjorden and Isfjorden (Spitsbergen), and IRD from the central Fram Strait. Note the closeness of the samples from the Yenisei, one grain-size fraction from the Ob, and some IRD samples to the Putoran flood basalts. Data for the Putoran flood basalts are from Arndt et al. (1995) and Wooden et al. (1993).
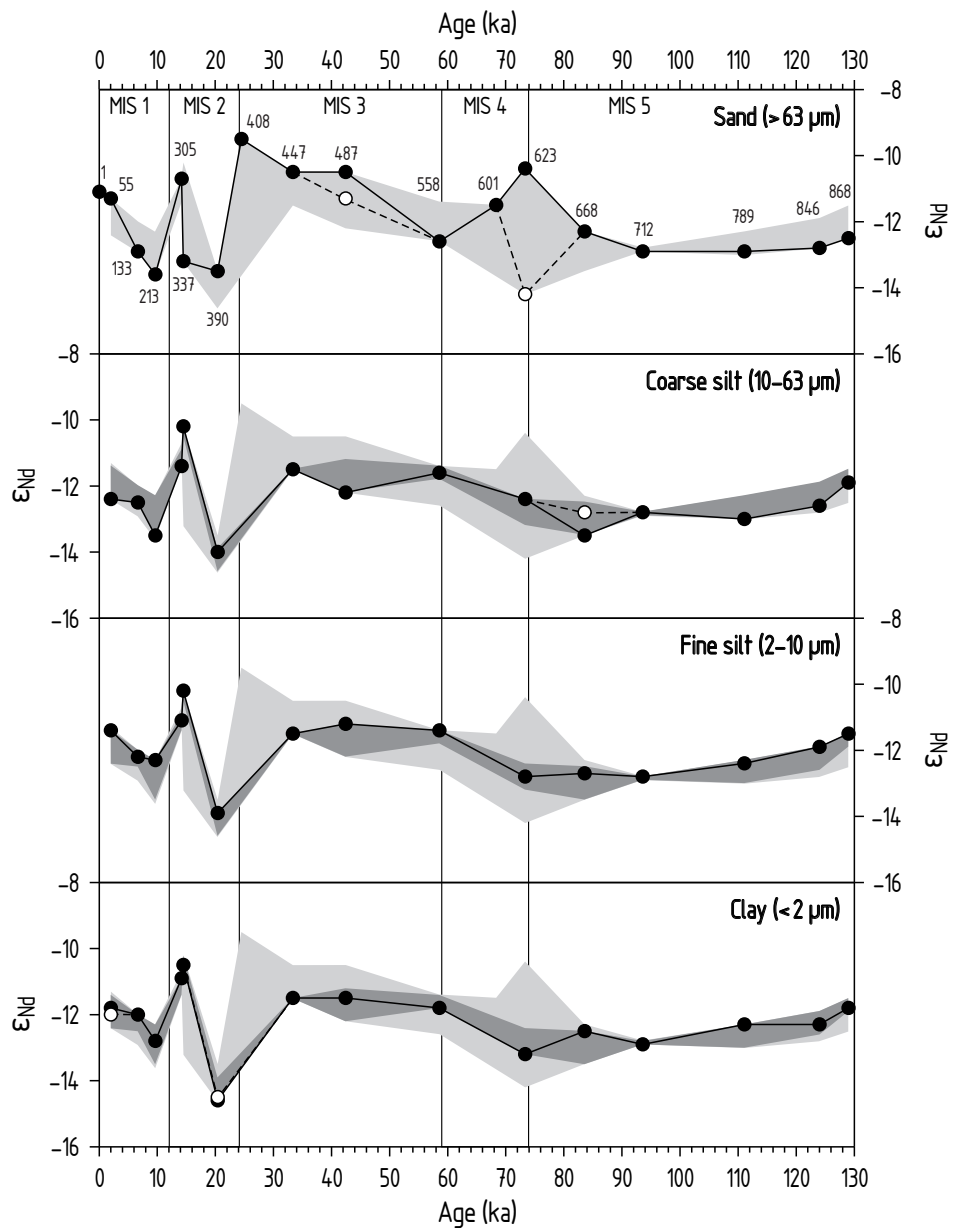
Figure 23 : Downcore variation of ε_{Nd} values for the size fractions clay, fine silt, coarse silt, and sand from sediment core PS2837-5. White circles represent replicate measurements of separate sample aliquots. The light gray area represents the Nd isotopic variation in all size fractions, the dark gray area that of clay, fine silt, and coarse silt only. MIS 1-5 are Marine Isotope Stages after **Martinson et al.** (1987).

0.1997. The three grain-size fractions of the Yenisei sample have a very homogeneous composition with ε_{Nd} values between -6.3 and -6.6, and Sm/Nd ratios between 0.2080 and 0.2094. These compositions are consistent with a significant contribution from the Permo-Triassic flood basalts of the Putoran Plateau ($\varepsilon_{Nd} \sim 0$, Sharma et al., 1992), outcropping in the catchment area of the Yenisei. The Nd isotopic compositions of IRD samples from the central Fram Strait scatter over a wide range (ε_{Nd} -6 to -13). IRD is not recognizable as a distinct source; instead, its Sm-Nd systematics can be explained by mixing of sediments delivered to the Arctic Ocean by the Siberian rivers Lena, Ob, and Yenisei (discussed in Chapter 4.2).

Nd isotopic downcore variation in PS2837-5 is shown for each grain-size class separately in Fig. 23. The curves for clay, fine silt, and coarse silt are very similar, and are in fact identical within the limits of reproducibility of $\pm 0.5\,\varepsilon_{Nd}$. The only exception is sample 213, with a moderate disagreement between its size fractions of $\pm 0.6\,\varepsilon_{Nd}$.

The agreement between the sand curve and the curves for the finer fractions is better than one would expect. For seven samples, the sand fraction is identical with the finer fractions within the limits of reproducibility. For five samples, the sand fraction is close to the finer fractions ($\pm 0.65\,\varepsilon_{Nd}$). For sample 487, one of the two analyzed sand aliquots agrees with the finer fractions to within $\pm 0.45\,\varepsilon_{Nd}$ ($\pm 0.85\,\varepsilon_{Nd}$ for the other). For sample 337 the situation is special, as it contained no detrital sand-size material. Instead, the sand from samples 334, 335, and 336 was combined for analysis. This composite sand sample differs from the three finer grain-size fractions of sample 337 by ca. $3\,\varepsilon_{Nd}$ values. The difference of $3\,\varepsilon_{Nd}$ units may reflect rapid changes in the sedimentational regime, rather than sample heterogeneity (the linear sedimentation rate in this part of the core is, according to the age-depth model, 110 cm·ka^{-1}, compared to 5.5 cm·ka^{-1} in the underlying interval).

. .   D

The distribution of depleted mantle model ages is shown in Fig. 24 separately for each grain-size class of the core samples and for all modern samples together. Model ages range from 1.50 Ga to 2.02 Ga for the core samples. Clay, fine silt, and coarse silt show a normal distribution of model ages (given the small number of data). The general trend of an increase in model age from clay over fine silt to coarse silt reflects the same trend in Sm/Nd ratios. The wider range of model ages for sand fractions reflects the higher scatter in Sm/Nd ratios, and shows a weak indication of a bimodal distribution.

For modern samples, model ages range from 1.37 Ga to 2.14 Ga and have a bimodal distribution. The cluster of model ages younger than 1.6 Ga is formed by the samples from the Ob and Yenisei, and most of the central Fram Strait IRD samples. Their 'young' model ages reflect the input of material derived from the Permo-Triassic flood basalts of the Putoran

Plateau. The remaining modern samples (Lena River, Spitsbergen, and two IRD samples) have model ages centered at approx. 1.85 Ga, somewhat younger than the global average for upper continental crust of ~2 Ga (Hawkesworth and Kemp, 2006).
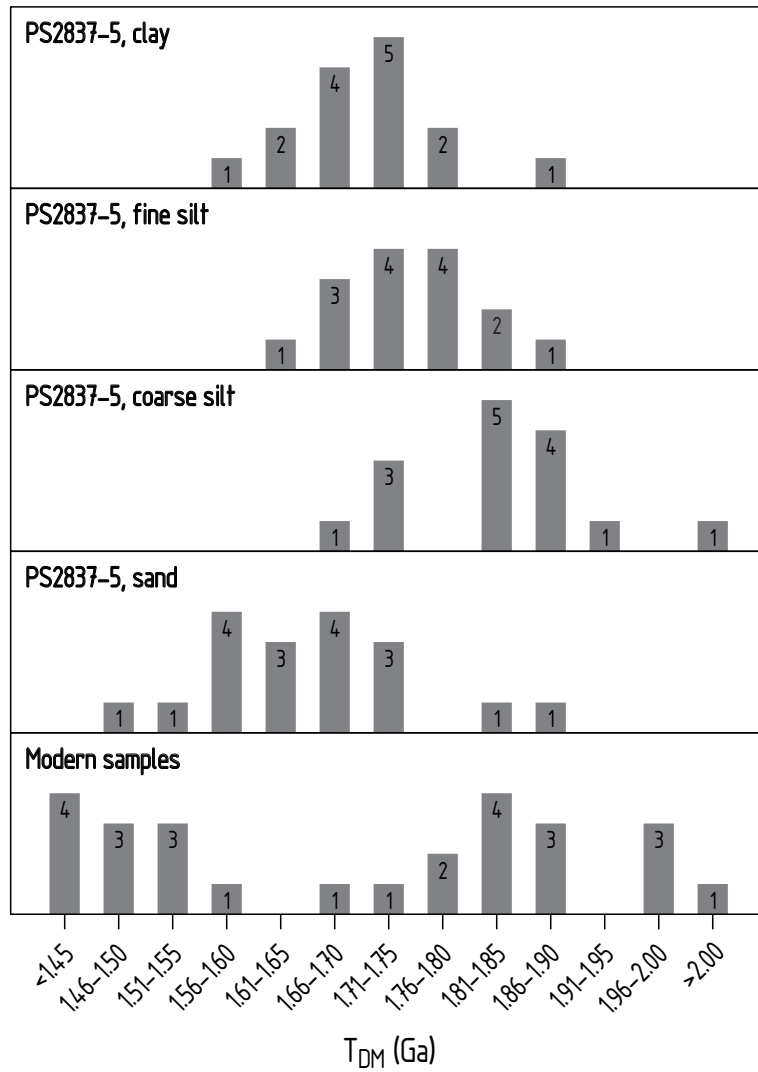
Figure 24 : Distribution of depleted mantle model ages in grain-size classes from core PS2837-5 and modern samples (grouped together).

.   REE   , HH-   ,   -

REE concentrations have been determined for five core samples from sediment core PS2837-5 (213, 390, 623, 668, and 789). For each sample, the untreated bulk sample, the HH leachable fraction, and the solid residue of the leaching process were measured by ICP-MS. The results are listed in Table 12.

Chondrite-normalized REE patterns for the untreated bulk samples (not shown) resemble typical clastic sediments derived from upper continental crust. Shale-normalized patterns (normalized to Post Archean Australian Shale [PAAS], Fig. 25), however, reveal a depletion of HREE relative to average sediment (exemplified by the REE pattern of USGS reference material MAG-1, a marine mud). This HREE depletion probably is an artifact, attributable to insufficient sample digestion (see Chapter 2.5). This may also affect the LREE, although the LREE and MREE in the untreated bulk samples are similar to MAG-1, and fall within the range of post-Archean Australian shales from Nance and Taylor (1976) on which the PAAS composite is based. Total REE contents (ΣREE) range from 163 $\mu g \cdot g^{-1}$ to 187 $\mu g \cdot g^{-1}$, and are similar to PAAS (185 $\mu g \cdot g^{-1}$). Sm and Nd concentrations in bulk samples are between 8 % higher and 10 % lower than predicted from TIMS data (bulk compositions calculated from size-fraction data). The degree of disagreement between ICP-MS data and TIMS data does not show any relation to particular sample properties, such as sand content or grain-size distribution.

The solid residues represent between 85 wt % and 92 wt % of the original aliquots, and have generally flat shale-normalized REE patterns with lower overall REE contents (ΣREE = 90-146 $\mu g \cdot g^{-1}$). Surprisingly, they show no HREE depletion, although the same refractory phases causing the HREE depletion in the untreated bulk samples should also be present in the leaching residues. A possible explanation for this apparent lack of HREE depletion is that it is compensated for by a loss of LREE and MREE at an earlier stage of sample treatment. Bulk compositions calculated from the results for the solid residues and leachates reveal that some LREE and MREE are indeed missing (up to 40 % for La). Loss of solid sample material during sample handling may account for these missing REE. Presumably, fine clay particles were lost during washing of the solid residues after leaching.

The HH leachates have higher total REE contents than the untreated bulk samples (ΣREE = 260-460 $\mu g \cdot g^{-1}$). These values probably underestimate the actual REE contents, since they are based on weight loss during leaching (providing a maximum estimate of leachate mass). Shale-normalized REE patterns display a distinct MREE enrichment with La_N/Sm_N ratios between 0.45 and 0.57, and small positive Ce anomalies between 1.05 and 1.16. The compatibility of these REE patterns with the assumed seawater origin of REE in the HH leachable fractions is discussed in Chapter 4.4.
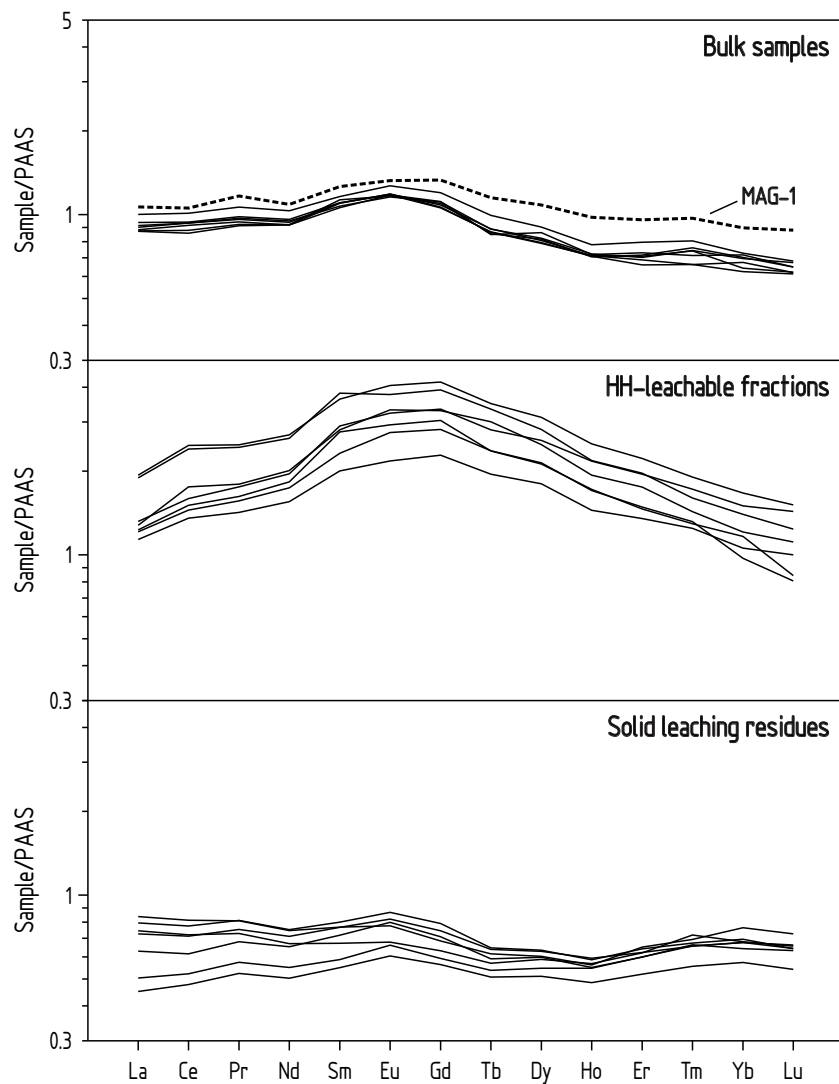
Figure 25 : Shale-normalized REE patterns for samples from sediment core PS2837-5. Top panel: untreated bulk samples. USGS reference material MAG-1 (marine mud) is shown for comparison (data from Dulski, 2001). Middle panel: HH-leachable fractions extracted from separate aliquots of the bulk samples. Bottom panel: solid residues of the leaching process. PAAS data from McLennan (1989). See text for details.

.   N   HH-

Nd isotopic compositions have been determined for the HH leachable fractions of nine core samples (133, 213, 337, 374, 390, 447, 601, 623, and 789; Table 13). ε_{Nd} values for the leachates vary between -9.3 and -13, and are consistently more positive than the calculated bulk compositions of the samples from which they have been extracted. Downcore, the curves for leachates and detrital grain-size fractions show a close covariation with a near
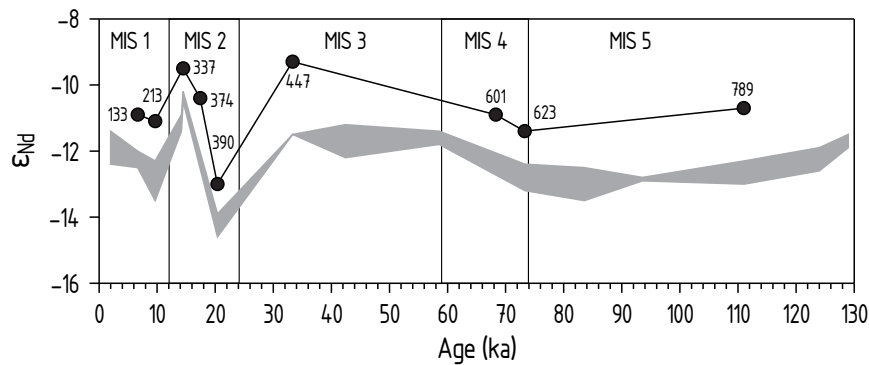
Figure 26: Downcore variation of ε_{Nd} values for HH-leachable fractions in sediment core
PS2837-5. Note that the curve runs sub-parallel to the gray band representing the range
of isotopic downcore variation for the clay, fine silt, and coarse silt fractions. MIS 1-5
are Marine Isotope Stages after **Martinson** et al. (1987)

constant offset of approximately 1.6 ε_{Nd} values (Fig. 26). The shape of the detrital curve
is in fact confirmed by the leachates from samples 374 and 601, for which there are no
detrital counterparts. Possible explanations for this systematic relationship are discussed in
Chapter 4.4.

.   S

Nd isotopic compositions and Sm and Nd abundances have been determined for the un-
treated bulk sample PS2837-5/712, solid residues of four aliquots of the same sample (sub-
jected to different leaching treatments), and six leachates extracted from these aliquots. Sm
and Nd abundances of solid residues and leachates are given in per cent relative to the un-
treated bulk sample, because no meaningful weights could be determined for the leachates
(due to, for instance, sodium acetate precipitated during evaporation of buffered acetic
acid). All results are given in Table 14.

The untreated bulk sample yielded 6.52 µg·g^{-1} Sm, 35.0 µg·g^{-1} Nd, Sm/Nd = 0.1863,
and ε_{Nd} = -12.1. This is in good agreement with a calculated bulk composition based on
the individual results for measurements of grain-size fractions from PS2837-5/712 (6.57
µg·g^{-1} Sm, 35.2 µg·g^{-1} Nd, Sm/Nd = 0.1866, and ε_{Nd} = -12.8).

Fig. 27 shows the Nd isotopic compositions for all samples plotted against their 'leach-
ing index'. The leaching index is an arbitrary measure of leaching. A solid residue with a
high index has been exposed to more and/or stronger leaching steps than a residue with
a low index, i.e. the leaching index increases with every leaching step performed. Accord-
ingly, the higher the index of a leachate, the higher the index of the solid residue from which
it has been extracted.
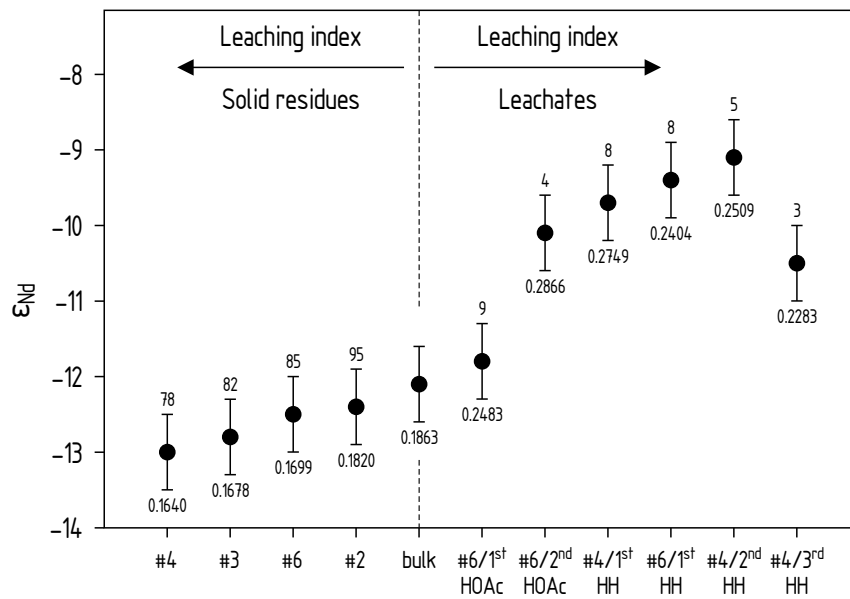
Figure 27: Nd isotopic compositions for leachates and solid residues of the sequential leaching experiment (error bars are $\pm 0.5\ \varepsilon_{Nd}$). The leaching index is an arbitrary measure of leaching. A solid residue with a high index has been exposed to more and/or stronger leaching steps than a residue with a low index. The higher the index of a leachate, the higher the index of the solid from which it has been extracted. Numbers below data symbols are Sm/Nd ratios, numbers above are per cent Nd relative to the untreated bulk sample as determined by isotope dilution, i.e. not normalized to 100 %.

The solid residues show a gradual development towards less radiogenic compositions with increasing leaching index, although the difference of 0.9 ε_{Nd} values between the solid residue with the highest leaching index and the untreated bulk sample is small compared to the external precision of $\pm 0.5\ \varepsilon_{Nd}$. Relative Sm and Nd abundances, and Sm/Nd ratios also decrease to 69 % for Sm, 78 % for Nd, and Sm/Nd = 0.1640, indicating the progressive extraction of a component with a Sm/Nd ratio higher than that of the untreated bulk sample.

A complementary trend is seen for the leachates, whose Nd isotopic compositions develop towards more radiogenic values (up to ε_{Nd} -9.1), except for the leachate with the highest leaching index, which has an intermediate ε_{Nd} of -10.5. Sm/Nd ratios are consistently higher than that of the untreated bulk sample (between 0.2283 and 0.2866), but show no systematic relation with the leaching index. The relative amounts of Sm and Nd in the different leachates vary between 4 % and 13 % for Sm and between 3 % and 9 % for Nd.

The Sm-Nd systematics of the leachates and solid residues cannot be explained by simple binary mixing between a pure detrital component and a leachable component with a high Sm/Nd ratio. Instead, the data are consistent with three-endmember mixing, as illus-

trated in Fig. 28. In a plot of Sm/Nd ratio vs ε_{Nd}, the solid residues fall on a mixing line ($R^2 = 0.984$) with the untreated bulk sample, #4/3rd HH, #6/1st HH, and #4/2nd HH (in the order of increasing Sm/Nd ratio). At the extreme ends lie #4 solid residue and #4/2nd HH (EM B in Fig. 28). Instead of #4 solid residue, #3 solid residue is chosen as the detrital endmember (EM A in Fig. 28) because prolonged leaching of #4 solid residue may have attacked detrital minerals, as indicated by the composition of #4/3rd HH. The three remaining leachates #6/1st HOAc, #6/2nd HOAc, and #4/1st HH plot off this mixing line. Two of these three leachates (#6/2nd HOAc and #4/1st HH) fall on a regression line with #4/2nd HH ($R^2 = 0.993$). If this correlation is interpreted as the result of binary mixing, than EM C falls on an extrapolation of the regression line towards less radiogenic ε_{Nd} values. The intersect of the EM B–EM C mixing line with an extrapolation of the connecting line between EM A and #6/1st HOAc yields the composition of EM C. Allowing for adjustments to optimize the R^2 values for the EM A–EM C and EM B–EM C mixing lines, EM C has a Sm/Nd ratio of 0.3164 and an ε_{Nd} of -10.9.

Data plotting along a straight line in a graph of Sm/Nd against ε_{Nd} are consistent with binary mixing only if the concentrations of Sm and Nd change continuously along this line. Although weighing of the leachates gave no meaningful results, the determined weights can be used to derive minimum estimates for the Sm and Nd concentrations of the leachates. Allowing Sm and Nd concentrations higher than these minimum estimates (within reasonable limits), EM B and EM C can be modelled. Concentrations of 20 $\mu g \cdot g^{-1}$ Sm and 80 $\mu g \cdot g^{-1}$ Nd for EM B, and 15 $\mu g \cdot g^{-1}$ Sm and 47.5 $\mu g \cdot g^{-1}$ Nd for EM C yield consistent results for all solid residues and leachates.

Regarding the nature of the endmembers, it can be said that EM A obviously is the detrital endmember. EM B, which is present in significant amounts only in the HH leachates, probably is the seawater endmember released from Fe-Mn phases. As dilute acetic acid is known to dissolve Fe-Mn phases (Chester and Hughes, 1967), if only in small amounts, the composition of the second acetic acid leachate of aliquot #6 is compatible with EM B being the seawater endmember. The nature of EM C is discussed in Chapter 4.4, but it can be observed that it is soluble in dilute acetic acid, and that it has been completely removed by twofold leaching with 1.7 $mol \cdot l^{-1}$ acetic acid prior to the first HH leaching. In contrast, the single leaching with buffered 0.87 $mol \cdot l^{-1}$ acetic acid prior to the first HH leaching of aliquot #4 has only partly removed EM C. This is an important observation, the implication of which is also discussed in Chapter 4.4.
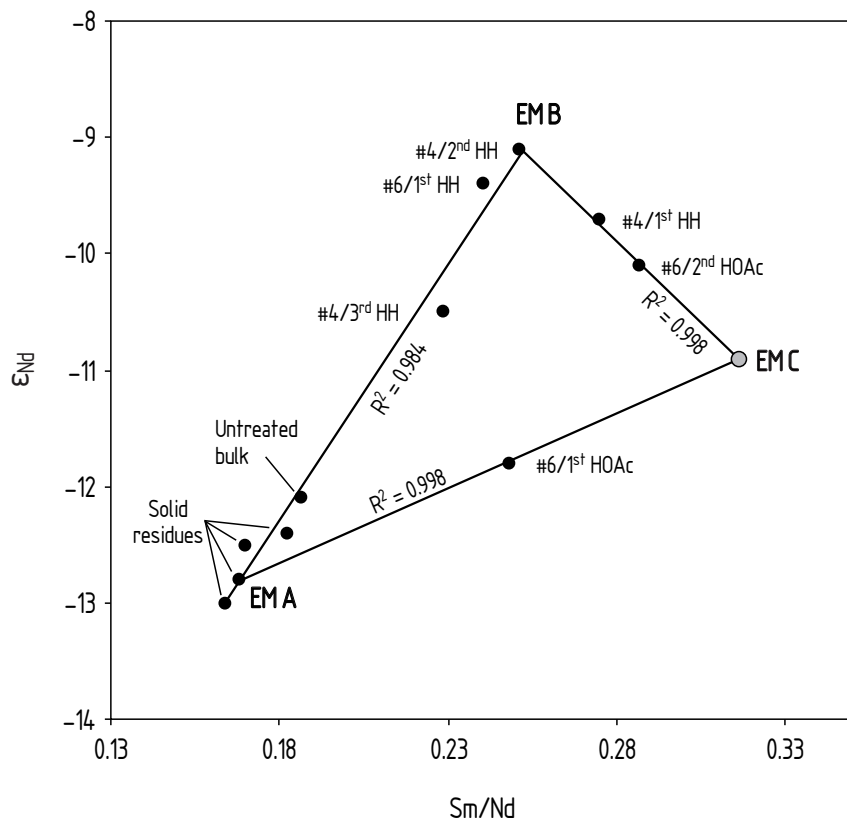
Figure 28 : Sm/Nd ratios vs ε_{Nd} values for the results of the sequential leaching experiment. The data are consistent with ternary mixing between #3 solid residue (EM A), #4/2nd HH (EM B), and a hypothetical endmember EM C (gray circle). See text for details.

D

. S   -

One of the initial assumptions of this study was that more detailed information about oceanographic processes may be gained by analyzing several grain-size fractions instead of just one (e.g. bulk samples). However, for 14 out of 15 samples from core PS2837-5, the ε_{Nd} values of clay, fine silt, and coarse silt are identical within the external reproducibility of ± 0.5 ε_{Nd} units. Only one sample shows a moderate disagreement between its fine size fractions of ± 0.6 ε_{Nd} values. It therefore seems justifiable to use calculated bulk compositions < 63 µm for the discussion of the results, rather than the individual grain size fractions. Although the sand fractions agree considerably well with the finer fractions for most samples (considering the poor reproducibility on the order of ± 2 ε_{Nd} values), they will be treated independently, for they have a special meaning as indicators of ice rafting.

Bulk compositions < 63 µm were calculated by three-endmember-mixing between clay, fine silt, and coarse silt, using the data from Table 10. The results are listed in Table 9, and shown as a downcore profile in Fig. 29. Bulk compositions < 63 µm were also calculated for the modern samples K5-2 (IRD), L22 (Lena), BP01/72 (Ob), and BP00/15 (Yenisei). The results are listed in Table 9.
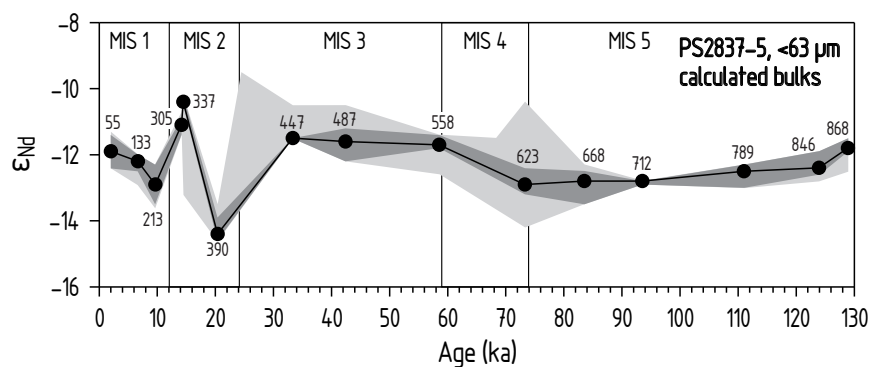
Figure 29 : Downcore variation of ε_{Nd} values in core PS2837-5, represented by calculated bulk compositions < 63 µm. The light gray area represents the isotopic variation in all size fractions, the dark gray area that of clay, fine silt, and coarse silt. MIS 1-5 are Marine Isotope Stages after **Martinson et al.** (1987).

Table 9 : Sm-Nd data for bulk samples (< 63 μm) from sediment core PS2837-5, central Fram
Strait IRD (K5-2), and the Siberian rivers Lena (L22), Ob (BP01/72), and Yenisei
(BP00/15). Calculated from size-fraction data in Tables 10 and 11.

Sample	Sm (μg·g^{-1})	Nd (μg·g^{-1})	Sm/Nd	^{147}Sm/^{144}Nd	^{143}Nd/^{144}Nd	ε_{Nd}	T_{DM} (Ga)
55	6.39	33.6	0.1902	0.1149	0.512 030	-11.9	1.73
133	6.45	34.2	0.1886	0.1139	0.512 015	-12.2	1.74
213	6.51	34.6	0.1882	0.1137	0.511 978	-12.9	1.79
305	6.45	34.0	0.1897	0.1146	0.512 068	-11.1	1.67
337	6.69	34.9	0.1917	0.1158	0.512 106	-10.4	1.63
390	7.04	37.8	0.1862	0.1125	0.511 898	-14.4	1.89
447	6.58	34.4	0.1913	0.1155	0.512 050	-11.5	1.71
487	6.95	35.8	0.1941	0.1172	0.512 041	-11.6	1.75
558	6.70	35.3	0.1898	0.1146	0.512 040	-11.7	1.71
623	6.32	33.5	0.1887	0.1140	0.511 975	-12.9	1.80
668	6.68	35.5	0.1882	0.1137	0.511 984	-12.8	1.78
712	6.68	35.7	0.1871	0.1130	0.511 980	-12.8	1.77
789	6.55	34.6	0.1893	0.1143	0.511 996	-12.5	1.77
846	6.17	32.3	0.1910	0.1154	0.512 004	-12.4	1.78
868	6.47	34.1	0.1897	0.1146	0.512 035	-11.8	1.72
IRD (K5-2)	4.67	24.2	0.1930	0.1166	0.512 172	-9.1	1.54
Lena	7.90	42.9	0.1841	0.1112	0.511 880	-14.8	1.89
Ob	6.20	31.9	0.1944	0.1174	0.512 217	-8.2	1.48
Yenisei	4.09	19.6	0.2087	0.1262	0.512 312	-6.4	1.46

.   S   Y

P

At the location of core PS2837-5, the deposition of lithogenic particles larger than 63 μm
can only be explained with delivery by floating ice. Under present-day, interglacial condi-
tions, sea ice rafting is supposed to be the main mechanism of sediment transport to the
deep Arctic Ocean (Nürnberg et al., 1994; Eicken et al., 2000), and may also significantly
contribute to the sedimentation at the Yermak Plateau.

The main source of sea ice IRD transported to the Fram Strait via the Trans Polar Drift
(TPD) is generally thought to be the western Laptev Sea shelf area, where shallow water
depth favors sediment entrainment by suspension freezing (Nürnberg et al., 1994; Eicken
et al., 1997; Tütken et al., 2002). As this process becomes less effective with increasing water
depth, the Kara Sea is generally considered to be of only minor importance regarding the
production of IRD (Pfirman et al., 1997). While this may be true for direct export of IRD
from the Kara Sea, Nd isotope data suggest that sediments becoming entrained in sea ice in
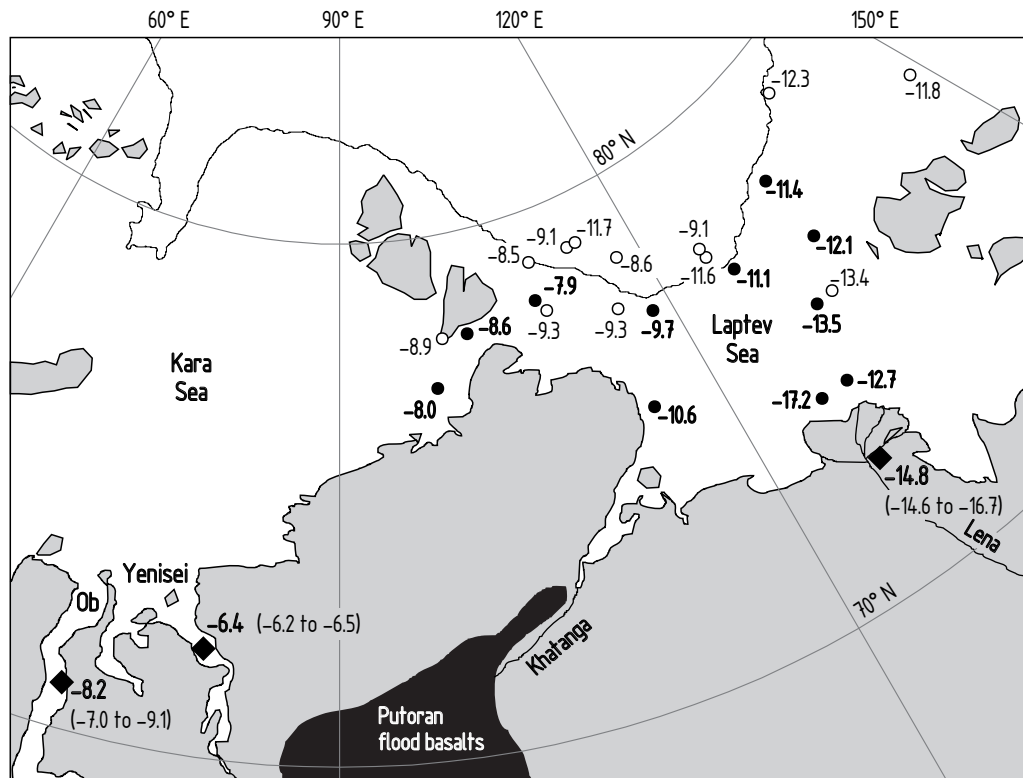
Figure 30 : ε_{Nd} values of bulk samples < 63 μm of surface sediments (filled black circles and bold numbers) and sediment-laden sea ice (open circles) from the eastern Kara Sea and the Laptev Sea (data from **Eisenhauer et al., 1999**, and **Tütken et al., 2002**), and calculated bulk compositions < 63 μm for sediments delivered by the Ob, Yenisei, and Lena rivers (black diamonds). The values in parentheses represent the total variation found for each river.

the western Laptev Sea contain a significant proportion of material originally delivered to the Kara Sea by the Ob and Yenisei rivers. **Eisenhauer et al.** (1999) and **Tütken et al.** (2002) reported Nd isotope data for surface sediments and sediment-laden sea ice from the eastern Kara Sea and the Laptev Sea. Although the data display some heterogeneity, a gradual eastward decrease of ε_{Nd} values from -8 in the eastern Kara Sea to approximately -13 in the eastern Laptev Sea is apparent (Fig. 30). Compared to the Nd isotopic compositions of sediments delivered by the Ob, Yenisei, and Lena (Table 11, Fig. 30), the data from **Eisenhauer et al.** (1999) and **Tütken et al.** (2002) are in excellent agreement with an eastward transport of clastic material from the Kara Sea into the Laptev Sea, and an eastward increasing influence of the Lena River.

Tütken et al. (2002) found a narrow range of ε_{Nd} values (-8.3 to -9.4) in sediment-laden sea ice in the Siberian branch of the TPD between Svalbard and Franz-Josef-Land, pointing to an origin from a restricted area within the western Laptev Sea. In contrast, ε_{Nd}

values between -6.0 and -12.8 for sediment-laden sea ice in the central Fram Strait (Table 11) indicate a less restricted source area probably including the Kara Sea and the eastern Laptev Sea.

In Fig. 31 Sm/Nd ratios and ε_{Nd} values for calculated bulk compositions < 63 μm for core PS2837-5 and the central Fram Strait IRD sample K5-2 are compared with calculated bulk compositions < 63 μm for the river samples from the Ob, Yenisei, and Lena. Consistent with the above findings, the IRD sample plots inside a mixing triangle defined by the three rivers. The core samples also plot inside, or close to, the same mixing triangle. This may suggest that IRD derived from the Kara- and Laptev Sea shelves, transported to the Yermak Plateau via the TPD, is the major component of sediments in core PS2837-5.

This view was suggested by Levitan et al. (2002b), who, based on the mineralogical compositions of sediment cores from the Yermak Plateau (including PS2837-5), argued that the lithogenic silt and sand fractions of sediments from the Yermak Plateau are mainly transported by sea ice and icebergs from Eurasian sources. For the pelitic fraction, they assumed a North Atlantic provenance including the Norway-Greenland Basin. Similarly, Tütken et al. (2002), based on Sr and Nd isotope data, argued that up to 75 % of interglacial sediments in core PS1533 (north-eastern Yermak Plateau, see Fig. 32) were transported as IRD from the western Laptev Sea shelf via the TPD. Vogt et al. (2001) also reported high percentages of Kara- and Laptev Sea shelf material in sediments from the last two deglaciations in core PS2212-3 (north-eastern Yermak Plateau, see Fig. 32).

The sedimentary record of PS2837-5, however, allows an alternative interpretation that
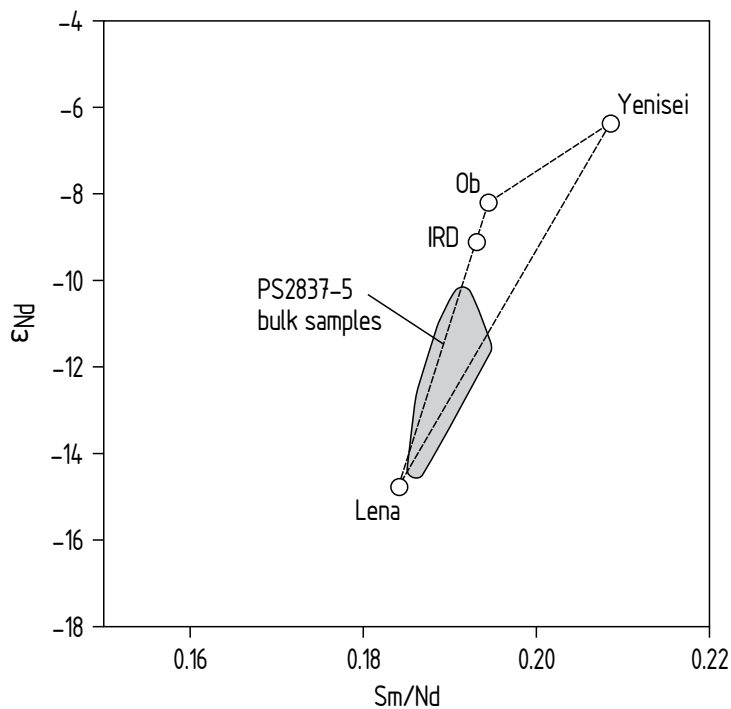
Figure 31: Calculated bulk compositions < 63 μm for core PS2837-5, compared to calculated bulk compositions < 63 μm for IRD sample K5-2 and the river samples from Ob, Yenisei, and Lena. The core samples and the IRD sample fall within, or close to, a mixing triangle defined by the Lena, Ob, and Yenisei samples.
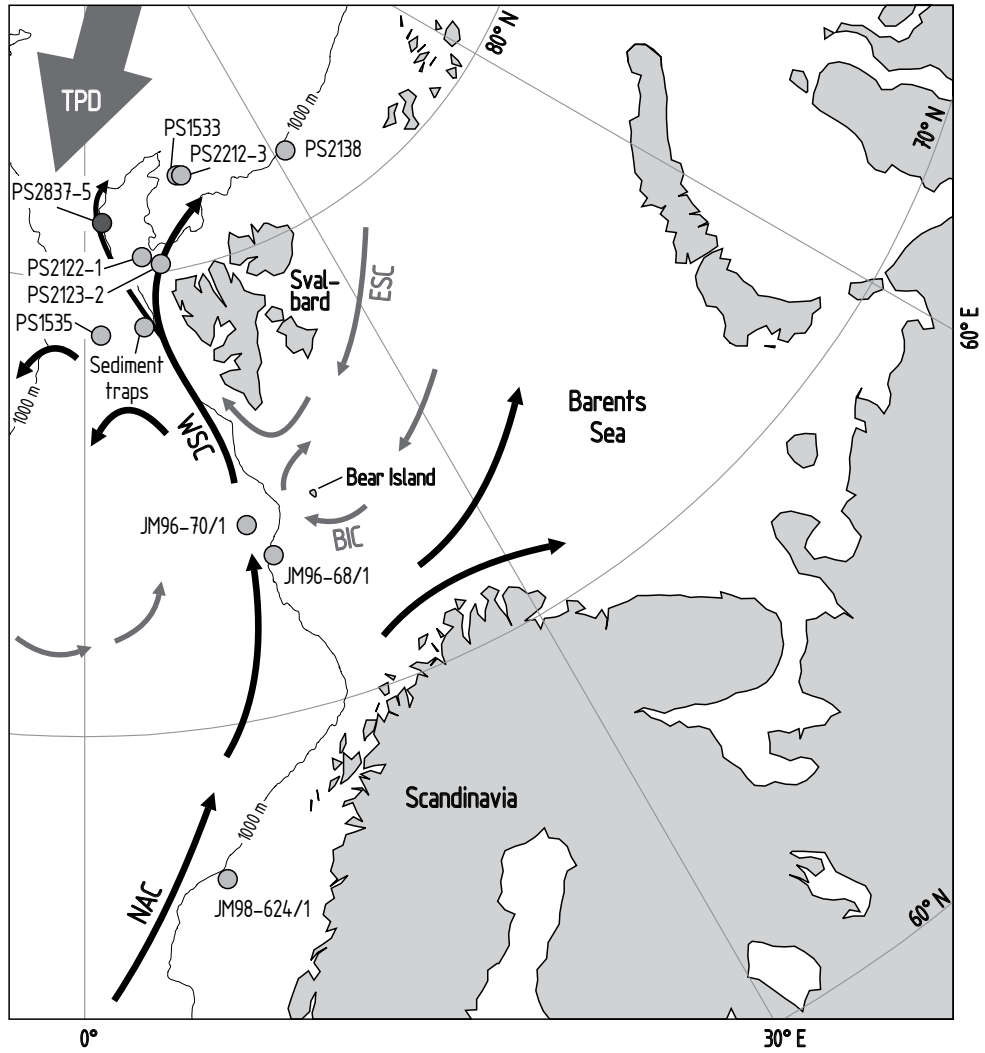
Figure 32 : Map of the Svalbard/Barents Sea area with a simplified illustration of surface circulation and locations of sediment cores and traps discussed in the text. Temperate waters of Atlantic origin are indicated by black arrows (NAC = Norwegian Atlantic Current, WSC = West Spitsbergen Current). Cold waters of Arctic origin are indicated by gray arrows (TPD = Trans Polar Drift, ESC = East Spitsbergen Current, BIC = Bear Island Current). PS1533 from Tütken et al. (2002); PS2212-3, PS2122-1, and PS2123-2 from Vogt et al. (2001); PS2138 from Knies et al. (2001); PS1535 from Spielhagen et al. (2004); sediment traps from Hebbeln (2000); JM96-68/1, JM96-70/1, and JM98-624/1 from Farmer and Barber (2003).

may also apply to other cores from the area. Compared to the sediment load of modern sea ice from the Arctic Ocean, the sediments in core PS2837-5 have higher clay and sand contents, and, despite covering 129 ka of sedimentation, are compositionally more homogeneous (Fig. 33). Also, sediment accumulation rates—at least in the uppermost part of the core corresponding to present-day oceanographic conditions—are too high to be explained by IRD deposition alone (Hebbeln, 2000). A second transport mechanism, presumably delivery of suspended matter by surface/subsurface currents, is therefore necessary. The Sm-Nd systematics of the core samples require that the current-delivered material (hereafter referring to the suspended load, as opposed to IRD delivered by sea ice or icebergs drifting with surface currents) has the same, or an isotopically very similar, source as the IRD. Since ice rafting is the only plausible mechanism for sediment transport to the Yermak Plateau from the Kara- and Laptev Sea shelves, this part of the Eurasian shelf can be excluded for the current transported component. A geographically different, but isotopically very similar source might be a possible explanation. However, it seems more plausible that the IRD in core PS2837-5 is not derived from the Kara- and Laptev Sea shelves at all, but instead has the same source as the current-transported component. This source presumably lies south of the core location, and both IRD and suspended matter are delivered by the West Spitsbergen Current (WSC).

Considering present-day oceanic circulation, the suspended load of the WSC may be derived from a variety of sources; sediment particles can be transported from the south by the NAC/WSC system (NAC = Norwegian Atlantic Current; see Fig. 32), and may also be delivered by other water masses converging with the WSC from the west or the east.

Due to complex patterns of recirculation in the Fram Strait and the Greenland Sea (Rudels et al., 1999; Schlichtholz and Houssais, 1999), the provenance of suspended matter that may be fed into the WSC from the west is difficult to constrain. Water leaving the Arctic Ocean through the western Fram Strait is partly recirculated towards the WSC in the Greenland Sea and may transport sediment from Amerasia and Greenland. However, significant sediment delivery from these areas is unlikely, since ε_{Nd} values typical for this area of < -20 (Tütken et al., 2002) are found neither in core PS2837-5, nor in core PS1533 (Tütken et al., 2002). Studies of the chemical composition of Fe oxide grains entrained in Arctic Ocean sea ice (Darby, 2003) and lithological compositions and abundances of ice rafted clasts in Arctic Ocean sediments (Phillips and Grantz, 2001) also indicate no significant sediment input from Amerasia and Greenland. Deposition of material from the Kara- and Laptev Sea via recirculation in the Greenland Sea cannot be excluded on the basis of Nd isotopes. It is, however, unlikely that the contribution from eastwards directed recirculation is significant (judging from, for instance, magnetic susceptibility distribution in surface sediments from the Greenland and Norwegian Seas, Pirrung et al., 2002).
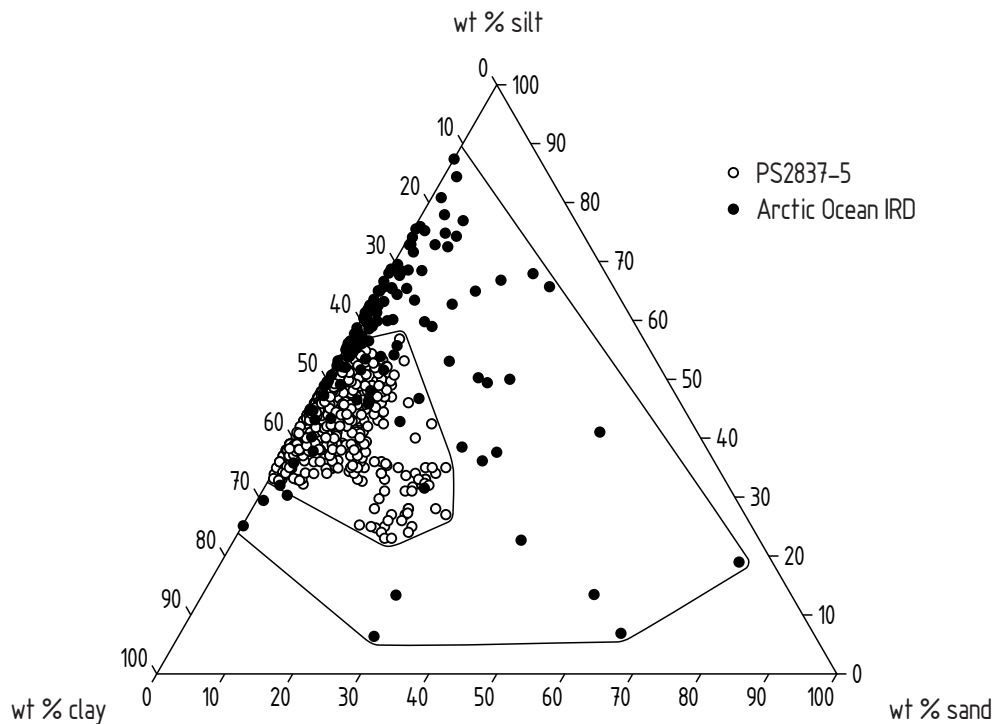
Figure 33: Grain-size compositions of 845 samples from sediment core PS2837-5 (data from Hass, 2000) and 129 samples of Arctic Ocean sea ice IRD (data from Wollenburg, 1993).

In contrast, significant contribution from the east, i.e. the Svalbard/Barents Sea area, is a plausible scenario supported by mineralogical data (high kaolinite contents of lithogenic material collected in sediment traps in the eastern Fram Strait; Berner and Wefer, 1994). Pathways for suspended particulate matter export from the Barents Sea are given under a variety of climatic conditions: today, the Bear Island and East Spitsbergen surface currents reach the western shelf edge (Fig. 32). Transport of suspended particles may also occur through the bathymetric depressions of the Bear Island Trough (south of Bear Island) and, to a lesser degree, the Storfjordrenna (north of Bear Island). These troughs are outlets for cold and saline waters that are formed on the shelf in winter (AMAP, 1998). During glacial periods, when the shelf was covered by an ice sheet, large amounts of sediments were transported subglacially to the shelf edge (e.g. Laberg and Vorren, 1995). Periodic collapse of sediment piles built from this subglacial transport repeatedly led to turbidity flows that built, for instance, the large Bear Island Trough Mouth Fan (BITMF; Laberg and Vorren, 1996).

The Barents Sea shelf is mainly composed of clastic Mesozoic rocks (Dallmann, 1999), which makes it difficult to estimate the Nd isotopic composition of sediments derived from this area. For instance, ε_{Nd} values for Triassic sandstones from Spitsbergen, Bear Island, Novaya Zemlya, and the central and southern Barents Sea scatter between -15.5 and 1.2

(Mørk, 1999). The problem of isotopic heterogeneity can be overcome by looking at naturally mixed composite samples, such as sediments from the BITMF. Since BITMF sediments were delivered by an ice stream fed by glaciers converging in the Bear Island Trough (Laberg and Vorren, 1995), they may provide a reasonable approximation to an average Barents Sea composition. Farmer and Barber (2003) presented Nd isotope data for two samples (< 63 μm) from the BITMF (cores JM96-68/1 and JM96-70/1, see Fig. 32). The sample from core JM96-68/1 is from a Late Weichselian (Last Glacial Maximum) debris flow deposit, and is entirely composed of Barents Sea shelf material (Laberg and Vorren, 2000). Its ε_{Nd} value of -10.1 is similar to the most radiogenic values in core PS2837-5 (Fig. 34), making a close genetic relationship possible. The sample from core JM96-70/1 has been dated to the Holocene, when, according to Laberg and Vorren (1995), most of the sediments introduced to the fan probably resulted from winnowing of shallow bank sediments on the Barents Sea shelf. This sample's moderately lower (relative to the Late Weichselian sample) ε_{Nd} value of -11.4 may indicate a contribution from a source outside the Barents Sea.

A plausible candidate for this source is the Norwegian shelf, from where sediments can be delivered by the NAC (see Fig. 32). Farmer and Barber (2003) presented Nd isotope data for two samples (< 63 μm, dated to the Last Glacial Maximum) from core JM98-624/1 from the mid-Norway shelf (see Fig. 32). The samples have ε_{Nd} values of -14.8 and -15.1, consistent with a western Baltic Shield source (Paleoproterozoic crust, or its reworked Caledonian equivalent; Farmer and Barber, 2003). Reduced sediment delivery from the Barents Sea shelf under interglacial (unglaciated) conditions may increase the relative proportion of sediments derived from the mid-Norway shelf, resulting in more negative ε_{Nd} values for the suspended load of the WSC. Note that ε_{Nd} values similar to the mid-Norway shelf are found in the Caledonian fold belt of western Spitsbergen (Kongsfjorden samples WoF and WoG, see Fig. 34). While sediment delivery from western Spitsbergen to the BITMF is unlikely (due to missing pathways), sediment transport to the Yermak Plateau via the WSC is plausible. The available Nd isotope data alone, however, do not allow to distinguish between western Spitsbergen and the mid-Norway shelf.

In summary, existing pathways and Nd isotope data suggest that the suspended load of the WSC is composed of material derived from the Barents Sea shelf and the Norwegian shelf/western Spitsbergen area. Variations in the relative proportions of sediments delivered from these areas can account for the downcore Nd isotopic variation found in core PS2837-5 (Fig. 34).

Independent evidence suggests that also the IRD in core PS2837-5 is mainly derived from the Svalbard/Barents Sea area. Hebbeln (2000) reported sediment flux data obtained from sediment traps moored for three years (during the late 1980s) in the eastern Fram Strait (see Fig. 32). Although a continuous but small release of IRD from TPD sea ice was observed, four to sixfold higher fluxes occurred when sea ice from the fjords and coastal
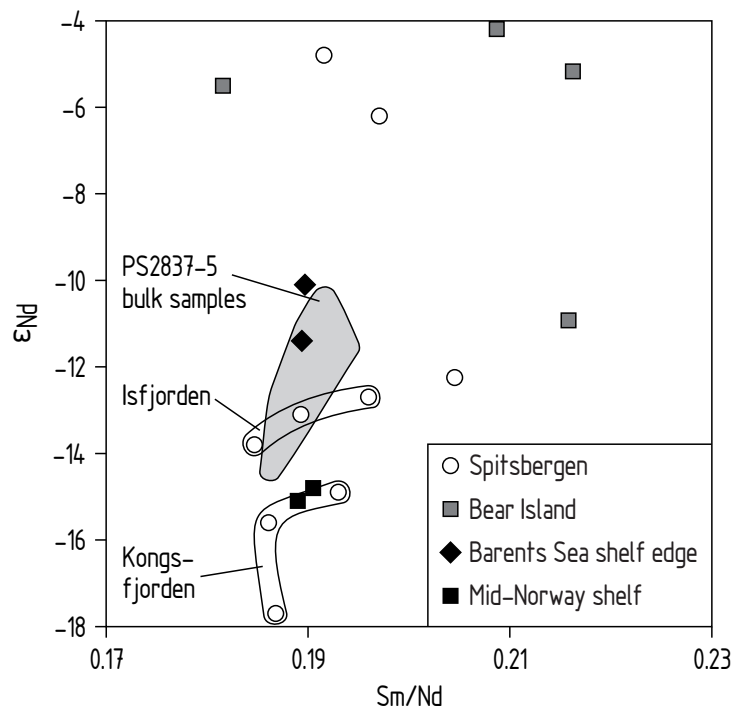
Figure 34: Sm/Nd ratios vs ε_{Nd} values for calculated bulk compositions < 63 µm from core
PS2837-5 and data from the literature. Spitsbergen (except Isfjorden and Kongsfjorden,
this study) and Bear Island data are for Triassic sandstones from Mørk (1999). Barents
Sea shelf edge and mid-Norway shelf data are for samples from the cores JM96-68/1,
JM96-70/1, and JM98-624/1 (see Fig. 32) from Farmer and Barber (2003).

areas of Svalbard and the Barents Sea was close to the sediment traps. A proximal source for
the released IRD is indicated by high numbers of plasma-containing benthic foraminifers.
The cold East Spitsbergen Current (ESC, Fig. 32) carries sea ice from the Barents Sea and
eastern Svalbard, and, after rounding the southern tip of Spitsbergen, flows northwards as
a coastal current (Johannessen, 1986). On its way north, it can pick up more sea ice from
the fjords and coastal areas of western Spitsbergen. If this Spitsbergen/Barents Sea sea ice
becomes entrained in the WSC (flowing further off the coast), it might be carried north
up to the location of core PS2837-5, and significantly contribute to the deposition of IRD
there.

Although TPD sea ice is also melted by the high surface temperatures of the WSC (> 0
°C year-round, Johannessen, 1986), it apparently releases significantly less IRD than the
Spitsbergen/Barents Sea sea ice. According to Hebbeln (2000), the explanation is found in
the age difference between the two different types of sea ice. The Spitsbergen/Barents Sea sea
ice is first-year ice, and its sediment load is evenly distributed throughout the ice column.
In contrast, the TPD sea ice has a multi-year history with several seasonal thawing/freezing

cycles, which lead to a net loss of sediment and a concentration of the remaining sediment at the surface of the ice floe (Pfirman et al., 1989). Because melting by 'warm' water happens from the bottom upwards, TPD sea ice requires substantially more melting than Spitsbergen/Barents Sea sea ice before IRD is released.

At this point it can be concluded that, at least under present-day oceanographic conditions, the western Yermak Plateau receives a strong input of current-transported sediments and IRD from the Svalbard/Barents Sea area (with possible contributions from Scandinavia). The flux of IRD derived from the Kara- and Laptev Sea shelves (which are the major sources for IRD in the deep Eurasian Basin) is proposed to be small compared to the input of IRD from the Svalbard/Barents Sea area.

.   O   Y   P
L   Q

Fig. 35 shows the downcore variation of sand content as an indicator of ice rafting by sea ice and icebergs, and ε_{Nd} values for the fractions > 63 µm and < 63 µm in core PS2837-5. The < 63 µm curve shows little variation around a mean ε_{Nd} value of -12.3 (± 0.5, 1σ) prior to 30 ka and after 10 ka, with no correlation between ε_{Nd} values and abundance of particles > 63 µm ($R^2 = 0.12$). Only between 30 ka and 10 ka, coeval with the most prominent peak in sand abundance, significant variation between ε_{Nd} values of -14.4 and -10.4 can be seen. The ε_{Nd} curve for the fraction > 63 µm shows higher variation than the finer fraction, but, as mentioned before, it is difficult to judge whether or not this higher variation is analytically significant. The correlation of ε_{Nd} values and abundance of particles > 63 µm is only marginally better ($R^2 = 0.2$).

As demonstrated above, sedimentation at the location of core PS2837-5 is, under present day oceanographic conditions, dominated by particulate matter derived from the Svalbard/Barents Sea area and possibly north-western Scandinavia. The aim of this Chapter is to demonstrate that the downcore variation in core PS2837-5 can be explained by climate induced variations in sediment delivery from these sources. If, as proposed, no other sources were involved, the basic modern pattern of circulation in the Atlantic–Arctic Ocean gateway has been active during most of the 129 ka covered by the sedimentary record of core PS2837-5.

In the past 180 ka (the last two glacial–interglacial cycles), the Svalbard/Barents Sea area and Scandinavia were affected by four large-scale glaciations (Svendsen et al., 2004): the Saalian (ca 180 ka-130 ka), the Early Weichselian (ca 90 ka-80 ka), the Middle Weichselian (ca 60 ka-50 ka), and the Late Weichselian (ca 24 ka-18 ka). Of these four glaciations, the Saalian was by far the largest in areal extent, total ice volume, and duration. The later glaciations were characterized by progressively smaller ice sheets over the Barents Sea, the
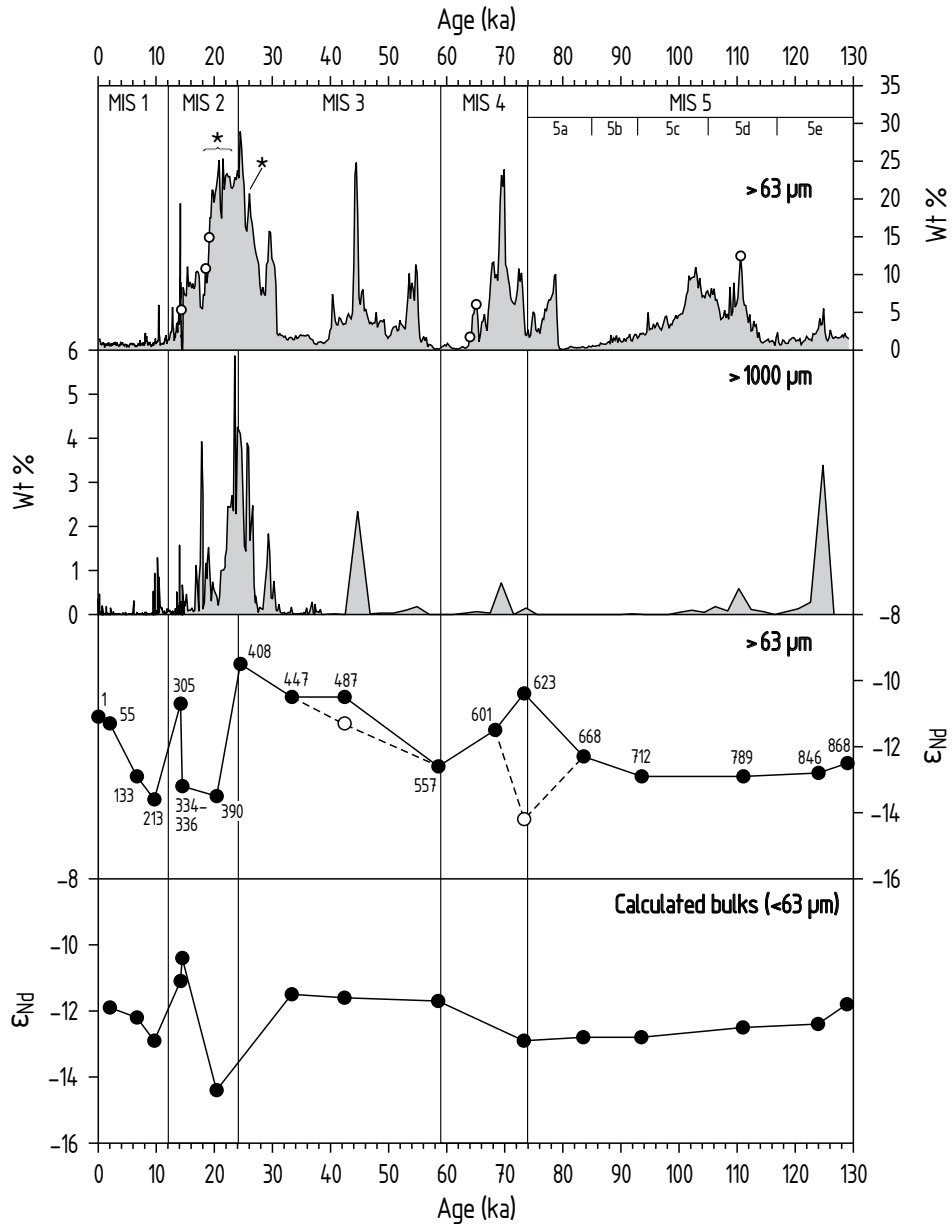
Figure 35: Downcore variation of abundance of particles > 63 μm and > 1000 μm, and ε_{Nd} values in core PS2837-5. Open circles in the > 63 μm abundance curve mark dropstones. Asterisks mark layers where high sand contents result from abundant planktic foraminifers (Nørgaard-Pedersen et al., 2003). This might also be the case for some sand-abundance peaks in the lower part of the core, for which no foraminifer data exist. The sample density of the > 1000 μm curve is 1 cm between 0 ka an 38.5 ka, and 10 cm beyond 38.5 ka. Open circles in the ε_{Nd} curve for sand represent replicate measurements of separate sample aliquots. Abundance data are from Hass (2000) for the fraction > 63 μm, and from Hass (unpubl. data) for the fraction > 1000 μm. MIS 1-5 are Marine Isotope Stages after Martinson et al. (1987).

Kara Sea, and the Siberian mainland, whereas the southward extension of the ice sheet over Scandinavia and northern Europe progressively increased. The smallest differences in areal extent between successive glaciations are found in the Svalbard/Barents Sea area and in northern Scandinavia (Svendsen et al., 2004). During each of these four glaciations, the ice caps over Svalbard and Scandinavia were at one point connected by an ice sheet covering the Barents Sea shelf (the Svalbard/Barents Sea Ice Sheet, SBIS), which had a triple effect. First, inflow of Atlantic water through the Barents Sea was cut off, rerouting the entire inflow to the Fram Strait. Second, transport of sea ice from a proximal source to the Yermak Plateau via the East Spitsbergen Current ceased and was replaced by iceberg rafting from the SBIS, possibly including more distant sources. Third, continuous injection of suspended matter into the WSC by outflow from the Barents Sea ceased. This might have been partly compensated for by outflow from meltwater channels, and periodic collapse of sediment piles build from continuous subglacial transport of material to the shelf break (Laberg and Vorren, 1996).

In the following paragraphs, the ε_{Nd} record of core PS2837-5 is discussed in the light of the current understanding of the glacial/interglacial history of the Svalbard/Barents Sea area. Additional information comes from core PS1533 from the eastern Yermak Plateau (Fig. 32), for which Tütken et al. (2002) presented a continuous ε_{Nd} record extending back to the Saalian glaciation (not recorded in core PS2837-5). Fig. 36 shows that the ε_{Nd} records for the two cores are similar during MIS 1, 2, and 5, whereas they are significantly different during MIS 3 and, to a lesser degree, in early MIS 4. This might as well be due to inconsistencies in the age-depth models.

. .   S   MIS   (–   )

According to recent land-based (Svendsen et al., 2004) and marine-based (Spielhagen et al., 2004) compilations of the Late Quaternary ice sheet history of northern Eurasia, the ice sheet configuration along the western Scandinavia-Barents Sea-Svalbard margin was similar during the peak phases of the Saalian glaciation (ca 135 ka) and the Last Glacial Maximum (LGM, ~21.5 ka-18 ka; Sarnthein et al., 2003), but different during the intervening glaciations. The Saalian and Late Weichselian glaciations may therefore have had similar effects on the delivery of sediments to the Yermak Plateau. The Nd isotope record of core PS1533 indeed shows similar ε_{Nd} values during the glacial maxima, and a similar shift to less radiogenic values during the deglaciations (Fig. 36).

A puzzling feature, according to Spielhagen et al. (2004), is that the onset of IRD deposition in the central and eastern Fram Strait is delayed by several thousand years relative to the central Arctic Ocean. Spielhagen et al. (2004) suggested that during the early parts of the glaciation, southward export of IRD bearing icebergs occurred through the western
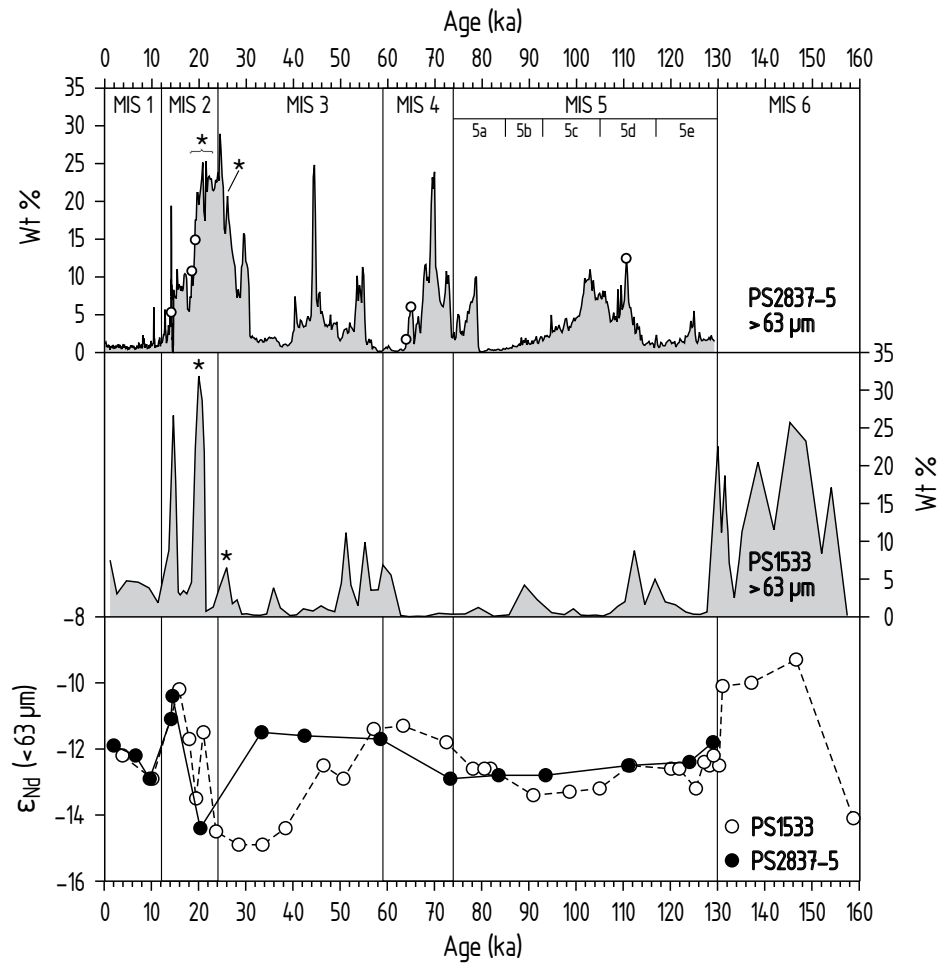
Figure 36 : Comparison of sand contents and downcore Nd isotopic variations in cores PS2837-5 and PS1533. Open circles in the sand abundance curve of PS2837-5 mark dropstones. Asterisks mark layers where high sand contents result from abundant planktic foraminifers (Nørgaard-Pedersen et al., 2003; Spielhagen et al., 2004). This might also be the case for some sand-abundance peaks in the lower parts of the cores, for which no foraminifer data exist. Note the similarity of the ε_{Nd} curves in MIS 1, 2, and 5. Nd isotope data for PS1533 from Tütken et al. (2002). Grain-size data for core PS2837-5 are from Hass (2000). Grain-size data and age model for PS1533 are from Spielhagen et al. (2004). MIS 1-6 are Marine Isotope Stages after Martinson et al. (1987).

Fram Strait only. This interpretation apparently is based on the assumption that the icebergs that delivered IRD to the central Arctic Ocean and the central and eastern Fram Strait had the same source. This, however, doesn't necessarily have to have been the case. Central Arctic Ocean IRD might have been delivered by icebergs drifting with the TPD, whereas IRD in the central and eastern Fram Strait could have been delivered by northward drifting icebergs that broke off the ice sheet at the western Svalbard/Barents Sea margin. If this was

the case, the delayed onset of IRD deposition indicates that the advancing ice sheet reached the shelf break at the western Svalbard/Barents Sea margin several thousand years later than in Siberia.

. .   MIS   (–   )

The oldest sediments in core PS2837-5 correspond to the last interglacial period, the Eemian (MIS 5e), during which a strong inflow of Atlantic water is recorded in several cores from the Arctic gateway and the Arctic Ocean (Spielhagen et al., 2004). The MIS 5e IRD peak in core PS2837-5 (Fig. 35) probably reflects the rapid disintegration of the remaining MIS 6 ice sheet. Evidence for iceberg rafting in MIS 5e is also found further south in core PS1535 (eastern Fram Strait; Spielhagen et al., 2004), but neither in core PS1533 (eastern Yermak Plateau; Spielhagen et al., 2004), nor in cores PS2123-2 and PS2122-1 (north-eastern Svalbard shelf and margin; Vogt et al., 2001). This suggests that the icebergs drifting over the location of core PS2837-5 calved off the western ice sheet margin (Svalbard/Barents Sea).

Further IRD peaks are found in core PS2837-5 in MIS 5d and 5c (Fig. 35). The MIS 5d peak correlates with the first post-Eemian ice sheet advance onto the Spitsbergen shelf between ca 118 ka and 106 ka (Mangerud et al., 1998). This glacial advance appears to have been restricted to the north-western Svalbard/Barents Sea area, and is not found in reconstructions of Scandinavian and northern Siberian ice sheet history (e.g. Svendsen et al., 2004). The MIS 5c peak coincides with a second Atlantic water inflow event around 100 ka (Spielhagen et al., 2004), and probably reflects the disintegration of the MIS 5d ice sheet. Again, evidence for iceberg rafting in MIS 5d and 5c is found in core PS1535, but to a much lesser degree in the other, more proximal cores to the east and southeast.

Sedimentary records from the central Arctic Ocean (Spielhagen et al., 2004) support land-based reconstructions (Svendsen et al., 2004) of a large-scale, Early Weichselian glaciation in north-eastern Eurasia during MIS 5b. Terrestrial and marine evidence suggests a short-lived (< 10 ka) advance to the west coast of Svalbard at that time (Mangerud et al., 1998). The ice sheet may in places have reached the shelf edge west of Svalbard, but nevertheless was much smaller than the MIS 5d ice sheet on Svalbard (Mangerud et al., 1998). Spielhagen et al. (2004) noted that the low IRD contents in MIS 5b sediments in cores PS1533 and PS1535 (as in core PS2837-5, see Fig. 35) are difficult to reconcile with their model of dominant iceberg drift out of the Arctic Ocean. They suggested that, due to inflowing Atlantic water, icebergs may have melted inside the Arctic Ocean before reaching Fram Strait. But, since indicators of Atlantic inflow yielded inconsistent results, they concluded that the low IRD contents remain (for the time being) an unsolved contradiction. If, however, as proposed in this thesis, the dominant direction of ice drift in the eastern Fram Strait was northward throughout the Late Quaternary, the lack of abundant IRD in MIS 5b is compatible with the very restricted extent of the glaciation on Svalbard.

Several cores from the Arctic gateway and the central Arctic Ocean contain faunal evidence (e.g. abundant planktic foraminifers) for an interval of strong inflow of Atlantic water in MIS 5a and MIS 4 (e.g. Hebbeln and Wefer, 1997; Spielhagen et al., 2004). In the central Arctic Ocean, this interval is interrupted by a sudden increase in IRD deposition shortly after 80 ka, accompanied by a drop in planktic foraminifer abundance (Spielhagen et al., 2004). The sharp lower boundary and fining-upwards character of the IRD rich layer indicate rapid onset and gradual decrease of iceberg rafting. Spielhagen et al. (2004) assumed that a combination of strong Atlantic water inflow (moisture supply) during MIS 5a and rapidly decreasing northern high-latitude insolation led to an early Middle Weichselian formation of ice domes in the Barents Sea/Kara Sea area. This iceberg rafting event is not recorded in Arctic gateway cores (Spielhagen et al., 2004); contents of particles > 63 μm are close to zero in core PS1533 (eastern Yermak Plateau), whereas elevated sand contents in core PS1535 (eastern Fram Strait) are caused by abundant planktic foraminifers. Since the abundance of planktic foraminifers in core PS1535 is continuously high between 80 ka and 65 ka (Spielhagen et al., 2004), the inflow of Atlantic water may have continued across the MIS 5/4 boundary. The low central Arctic foraminifer abundances during the 80 ka ice rafting event may therefore reflect diminished surface productivity (due to dense ice cover) rather than reduced inflow of Atlantic water.

The shape of the 80 ka-74 ka peak in the > 63 μm abundance curve of core PS2837-5 (Fig. 35) resembles that found in central Arctic Ocean cores. However, it appears not to be related to increased iceberg rafting (it is not seen in the > 1000 μm record). Different possible explanations for the elevated sand contents, all connected to the strong inflow of Atlantic water, include abundant planktic foraminifers (as in core PS1535), winnowing of finer particles by fast flowing bottom water, or enhanced melting of sediment laden sea ice.

Despite considerable climatic variability in MIS 5, the Nd isotope record of core PS2837-5 shows only minor variation during this period (Fig. 35). For fractions > 63 μm (representing IRD deposition), ε_{Nd} values first decrease from -12.5 for sample 868 to -12.9 for sample 712, and the rise to -12.3 for sample 668 (the age of 73.3 ka for sample 623 probably is overestimated by ca 8 ka, placing it in middle MIS 4 instead; discussed below). The ε_{Nd} curve for fractions < 63 μm (representing WSC suspended load plus fine-grained IRD) shows similarly small variation. The greater part of this small variation occurs early in the record, between samples 868 (129 ka, ε_{Nd} -11.8) and 846 (124 ka, ε_{Nd} -12.4). The remaining part of the interval is characterized by a gradual decrease of ε_{Nd} values to -12.8 for sample 668 (continued until the probably incorrectly dated sample 623, ε_{Nd} -12.9, see above). With an ε_{Nd} value similar to that for the youngest core sample 55 (2 ka, ε_{Nd} -11.9), and close to that for a Holocene sample from core JM96-70/1 from the BITMF (ε_{Nd} -11.4, Farmer and Barber, 2003), sample 868 is considered to reflect typical interglacial conditions. The subsequent decrease of ε_{Nd} values to -12.8 for sample 668 (or -12.9 for sample

623) is of similar magnitude as the variation between the Holocene (interglacial) samples 213, 133, and 55 (Fig. 35). Although full interglacial conditions clearly did not prevail throughout MIS 5, full, global-scale glacial conditions were not reached either (at no time between the Saalian and the Late Weichselian, e.g. Spielhagen et al., 2004; Svendsen et al., 2004). This may suggest that the delivery of suspended particulate matter to the western Yermak Plateau is significantly influenced only by climatic variation of full glacial/full interglacial amplitude. On the other hand, the gradual nature of the MIS 5 trend argues for some response to an equally gradually operating, not yet identified mechanism.

The good agreement between IRD abundance in core PS2837-5 and the glacial history of the Svalbard archipelago suggests that the north-western Svalbard/Barents Sea area was the dominant, if not the only, source of IRD delivered to the western Yermak Plateau during MIS 5. The narrow range of ε_{Nd} values argues for a very restricted source area within the isotopically heterogeneous Svalbard/Barents Sea region (e.g. Isfjorden, see Fig. 34, or other areas with similar Mesozoic lithologies on eastern Svalbard and the north-western Barents Sea shelf). This, in turn, argues for a derivation of WSC suspended load from the same area. In analogy to the present-day situation, suspended matter from the Barents Sea shelf, delivered via the East Spitsbergen and Bear Island currents, might have dominated the suspended load budget of the WSC. Note, however, that the likely interruption of the East Spitsbergen and Bear Island currents during times when an ice sheet covered the interior part of the Barents Sea shelf presents a problem. The Early Weichselian glaciation in MIS 5b, for instance, although of limited extent along the western Svalbard margin (Mangerud et al., 1998), probably occupied the entire Barents Sea shelf east of Svalbard (Svendsen et al., 2004). Although speculative, the missing Barents Sea outflow might have been completely compensated for by periodic collapse of sediment piles resulting from subglacial transport to the shelf edge.

. . MIS – MIS (–)

The MIS 5/4 and MIS 4/3 boundaries are uncertain for core PS2837-5. For reasons discussed in section 2.1.1.1, the age-depth model for the lower half of core PS2837-5 is based on linear interpolation between the oldest reliable AMS ^{14}C date at 389 cm (20.16 ka) and an age estimate of 129 ka for the core bottom. Necessarily, this approach yields a constant sedimentation rate, which, however, is an unrealistic assumption for more than 100 ka of sedimentation in a dynamic environment. It is therefore likely that the stratigraphy of core PS2837-5 is partly distorted (i.e. compressed or stretched) by the linear age-depth model. The core section predicted to correspond to MIS 4 to early MIS 3 appears to be particularly affected.

Based on high rates of IRD deposition in the central Arctic Ocean, Spielhagen et al. (2004) concluded that the Middle Weichselian (MIS 4 to early MIS 3) ice sheet in northern Eurasia was exceptionally productive in terms of iceberg calving rate and/or sediment load. Using faunal evidence from Fram Strait sediment cores (Baumann, 1990; Hebbeln and Wefer, 1997; Hald et al., 2001), they suggested that seasonally open water conditions, caused by strong MIS 4 Atlantic water inflow (Hebbeln and Wefer, 1997), still existed when the ice sheet had already reached much of its maximum extent. The associated, persisting moisture supply probably was stronger than during earlier MIS 6 and 5 glaciations, leading to a faster ice flow and thus a higher iceberg calving rate. The implication for core PS2837-5 is that the sedimentation rate during the Middle Weichselian probably was higher than the 4.40 cm·ka^{-1} predicted by the age-depth model.

High IRD abundances in MIS 4 to early MIS 3 (65 ka–50 ka) sediments in many cores from the Arctic gateway and the central and eastern Arctic Ocean are related to the main phase of the Middle Weichselian glaciation (Spielhagen et al., 2004, and references therein). In core PS2837-5, this interval probably is represented by the core section dated to 74 ka–50 ka. Elevated sand contents between 74 ka and 63 ka, and between 55 ka and 53 ka (Fig. 35), can unambiguously be attributed to iceberg rafting. Peaks in the > 1000 μm curve at 73.5 ka, 69.5 ka, and 54 ka (Fig. 35), and dropstones at 587 cm (65.8 ka) and 582 cm (64.7 ka) prove melting of icebergs over the western Yermak Plateau. If the stratigraphic model for core PS2837-5 indeed overestimates the age of this core section, then the onset of enhanced IRD deposition dated to 74 ka may correlate with the approach of the SBIS to the shelf break at ca 65 ka (Mangerud et al., 1998), as recorded in several cores from the western, north-western, and northern Svalbard/Barents Sea margin (Mangerud et al., 1998; Vogt et al., 2001; Knies et al., 2001). A local minimum in the planktic foraminifer $\delta^{18}O$ record of core PS2837-5 (R.F. Spielhagen, personal communication) suggests that the 55 ka–53 ka sand peak in core PS2837-5 correlates with a major deglacial event, which is recorded throughout the Arctic as a strong meltwater spike around 52 ka (Spielhagen et al., 2004). The interval with low sand contents dated to 63 ka–55 ka may reflect a reduction in the rate of iceberg calving between the retreat of the ice sheet from the shelf break at ca 59 ka (Mangerud et al., 1998) and the 52 ka major deglacial event.

Nd isotope data for fractions > 63 μm from core PS2837-5 suggest significant differences in IRD delivery between the MIS 5 and MIS 4 glaciations. Although the reliability of ε_{Nd} values for sand samples is questionable (see replicate of sand sample 623, Fig. 35), the excursion towards more positive values during the Middle Weichselian (sand samples 623 and 601, perhaps beginning with sample 668) is considered to be at least qualitatively correct. Sand sample 557 (ε_{Nd} -12.6), probably post-dating the retreat of the Middle Weichselian ice sheet from the shelf break, records a return to pre-glacial conditions. The shift to more positive ε_{Nd} values during MIS 4 is compatible with an increased input of IRD

derived from eastern Svalbard. The lack of such a shift during the MIS 5d glaciation (which was of similar areal extent in the north-western Svalbard/Barents Sea area; Mangerud et al., 1998) may be explained with the aforementioned model of exceptionally fast Middle Weichselian ice flow of Spielhagen et al. (2004). Iceberg calving rates generally are highest in front of fast flowing ice streams (Dowdeswell et al., 1998; Siegert and Dowdeswell, 2002). Accordingly, the Middle Weichselian glaciation in the north-western Svalbard/Barents Sea area may have been characterized by ice streams (e.g. through Isfjorden) that were larger and faster than during the Early Weichselian. The IRD carried by Middle Weichselian icebergs may therefore have been derived from more interior parts of the ice sheet (e.g. eastern Svalbard, Mesozoic sedimentary rocks), yielding a more radiogenic Nd isotopic signature than Early Weichselian IRD.

Fractions < 63 μm show a very different response to the Middle Weichselian glaciation. Sample 623 (ε_{Nd} -12.9) falls on the trend of minimally decreasing ε_{Nd} values throughout MIS 5 (Fig. 35). This supports the assumption (derived from the MIS 5 Nd isotope record) that the ice sheet, which at that time probably had reached its maximum extension, had no influence on the transport of WSC suspended load. Sample 558 (ε_{Nd} -11.7), probably post-dating the peak glacial phase, marks the end of the MIS 5/MIS 4 trend and records a return to typical interglacial ε_{Nd} values that remain stable around -11.6 throughout MIS 3.

. .   M   MIS (.   –   )

In core PS2837-5, the interval between 50 ka and 30 ka is characterized by sand contents around 5 wt % before 40 ka (with a prominent peak at 45 ka), and around 1-2 wt % after 40 ka (Fig. 35). Although the elevated sand contents between 50 ka and 40 ka might reflect sea ice rafting, rather than iceberg rafting, the peak in abundance of clasts > 1000 μm at 45 ka proves iceberg drift at that time. Similar indication for ice rafting is found in cores from the northern Barents Sea margin (PS2138; Knies et al., 2001) and the eastern Fram Strait (PS1535; Spielhagen et al., 2004). Elevated levels of clasts > 2 mm in PS2138 between 50 ka and 40 ka are compatible with the presence of a Middle Weichselian ice sheet in parts of the eastern Svalbard/Barents Sea area until at least 44 ka, as proposed by Andersen et al. (1996). High amounts of IRD with typical Mesozoic rocks from the Barents Sea in sediments from 50 ka to 35 ka in core PS1535 indicate that a minor glaciation may have existed in the NW Barents Sea area prior to the main ice sheet build-up in latest MIS 3 (Spielhagen, 1991; Spielhagen et al., 2004).

In contrast, cores from the north-western Svalbard margin (e.g. PS2122-1 and PS2123-2) and the eastern Yermak Plateau (e.g. PS2212-3 and PS1533) contain only minor IRD from the period between ca. 50 ka and 30 ka (Vogt et al., 2001; Spielhagen et al., 2004). Thus, the IRD record of core PS2837-5 more closely resembles those of cores from the

northern Barents Sea margin and the eastern Fram Strait, rather than those of more prox-
imal cores from the north-western Svalbard margin and the eastern Yermak Plateau. This
finding supports the assumption that the deposition of IRD at the western Yermak Plateau
mainly responds to fluctuations of the marine-based part of the SBIS. The correlation be-
tween the IRD record of core PS2837-5 and fluctuations of the land-based part of the SBIS
on the Svalbard archipelago appears to be weak, which is also indicated by the significantly
different isotope records of the cores PS2837-5 and PS1533 during MIS 3 (Fig. 36, discussed
below).

The decrease of sand contents in core PS2837-5 at 40 ka may be connected to a strong
inflow of temperate Atlantic water into the Fram Strait that occurred during the 'high pro-
ductivity event' HP3 (ca. 41 ka-38 ka) in the Fram Strait and the Nordic Seas (Dokken and
Hald, 1996; Hald et al., 2001). In contrast to other inflow events, this one probably caused
a negative ice mass balance instead of ice sheet growth (Spielhagen et al., 2004). Consistent
with this assumption, the small sand peak (7.4 wt %) at 40.4 ka in core PS2837-5 may re-
flect the disintegration of a minor ice sheet in the Svalbard/Barents Sea area. The increase
in sand content from ~1 wt % to ~2 wt % around 38 ka may then mark the end of the
inflow event, and indicate an intensification of ice rafting. Note, however, that this match
might as well be a coincidental result of uncertainties in the age-depth model.

Nd isotope data are available for two samples from the interval between 50 ka and 30
ka: sample 487 at 42.4 ka, and sample 447 at 33.3 ka. The fractions < 63 μm of these two
samples have typical interglacial ϵ_{Nd} values of -11.6 and -11.5, respectively. The fractions
> 63 μm, on the other hand, follow a trend characterized by progressively more radiogenic
ϵ_{Nd} values throughout MIS 3 (Fig. 35). The ϵ_{Nd} values of -10.5 for the samples 487 sa and
447 sa (-11.3 for the replicate of 487 sa) are close to the assumed average Barents Sea shelf
composition of ϵ_{Nd} -10.1 (see Chapter 4.2), which is compatible with the minor, pre-LGM
glaciation in the NW Barents Sea area as proposed by Spielhagen (1991) and Spielhagen
et al. (2004). The lack of an unradiogenic component suggests that the glaciation may have
been restricted to eastern Svalbard, leaving the Caledonian fold belt in western Spitsbergen
ice free.

Fig. 36 shows that ϵ_{Nd} values for fractions < 63 μm from core PS1533 between 40 ka
and 30 ka are significantly more negative than in core PS2837-5. According to Tütken et al.
(2002), the low ϵ_{Nd} values in core PS1533 reflect a massively increased input of material
derived from northern Spitsbergen, which would be in accordance with a build-up of the
Late Weichselian ice sheet on Svalbard as early as 40 ka (as proposed by Lloyd et al., 1996).
This early build-up of an ice sheet on Svalbard is neither reflected in the Nd isotope record
of core PS2837-5, nor recorded in other cores from the area (Knies et al., 2000; Vogt et al.,
2001), which may point to inconsistencies in the age-depth model for core PS1533.

Knies et al. (2000) argued for a rapid build-up of the SBIS after 34 ka, whereas Lloyd et al. (1996) propose an onset of glaciation on Svalbard as early as 40 ka. The general consensus, however, is that the major build-up of the Late Weichselian SBIS was a two-step process connected to periods of strong Atlantic water inflow (i.e. moisture supply) between 32 ka and 26 ka, and around 20 ka (Spielhagen et al., 2004). Both inflow events are reflected by high abundances of planktic foraminifers in cores PS1535 and PS1533 (Spielhagen et al., 2004). High abundances of planktic foraminifers are also found in core PS2837-5 (Nørgaard-Pedersen et al., 2003), and, between 23 ka and 18 ka in particular, result in high abundances of particles > 63 μm that do not reflect increased ice rafting (Fig. 35).

A peak in IRD abundance at ca. 30 ka in core PS2138 from the northern Barents Sea margin is interpreted as a first initial instability of the ice sheet during build-up (Knies et al., 2001). A similar peak is found in core PS2837-5 (Fig. 37), but not in cores from the northwestern Svalbard margin and the eastern Yermak Plateau (Vogt et al., 2001; Spielhagen et al., 2004). This, again, supports the assumption that the deposition of IRD at the western Yermak Plateau mainly responds to fluctuations of the marine based-part of the SBIS.

On the continental slope west of Spitsbergen, the initial stage of the Late Weichselian glaciation (30 ka-27 ka) was characterized by low accumulation rates and a low influx of iceberg rafted sediments (Elverhøi et al., 1995). Clay mineral assemblages and reworked palynomorphs of Late Cretaceous and Triassic age point to eastern Svalbard and parts of the northern and eastern Barents Sea as the sources of the delivered sediments (Elverhøi et al., 1995).

At 27 ka, synchronous with an increase in abundance of particles > 1000 μm in core PS2837-5 (Fig. 37), the ice sheet reached the northern Barents Sea margin between Svalbard and Franz-Josef-Land (Knies et al., 2000, 2001). At the same time, the ice sheet advanced onto the Barents Sea shelf south of Svalbard (Elverhøi et al., 1995). The advance to the shelf break west of Svalbard was delayed until 22.5 ka (Andersen et al., 1996; Landvik et al., 1998). Grounded ice on the western Svalbard shelf might have affected the northward transport of icebergs by coastal currents, as could be concluded from the reduction of IRD > 1000 μm in core PS2837-5 around 22.5 ka (Fig. 37).

Sediments deposited on the continental slope west of Svalbard between 27 ka and 22.5 ka are characterized by high contents of organic carbon and abundant rock fragments with lithologies typical for the northern and eastern Barents Sea (Elverhøi et al., 1995; Andersen et al., 1996). The high organic carbon contents are thought to reflect increased erosion of Jurassic shales on Spitsbergenbanken south of Svalbard (Elverhøi et al., 1995). Accordingly, sediments in core PS2837-5 deposited between 27 ka and 22.5 ka can be expected to contain no IRD derived from western Spitsbergen, but abundant material derived from the north-
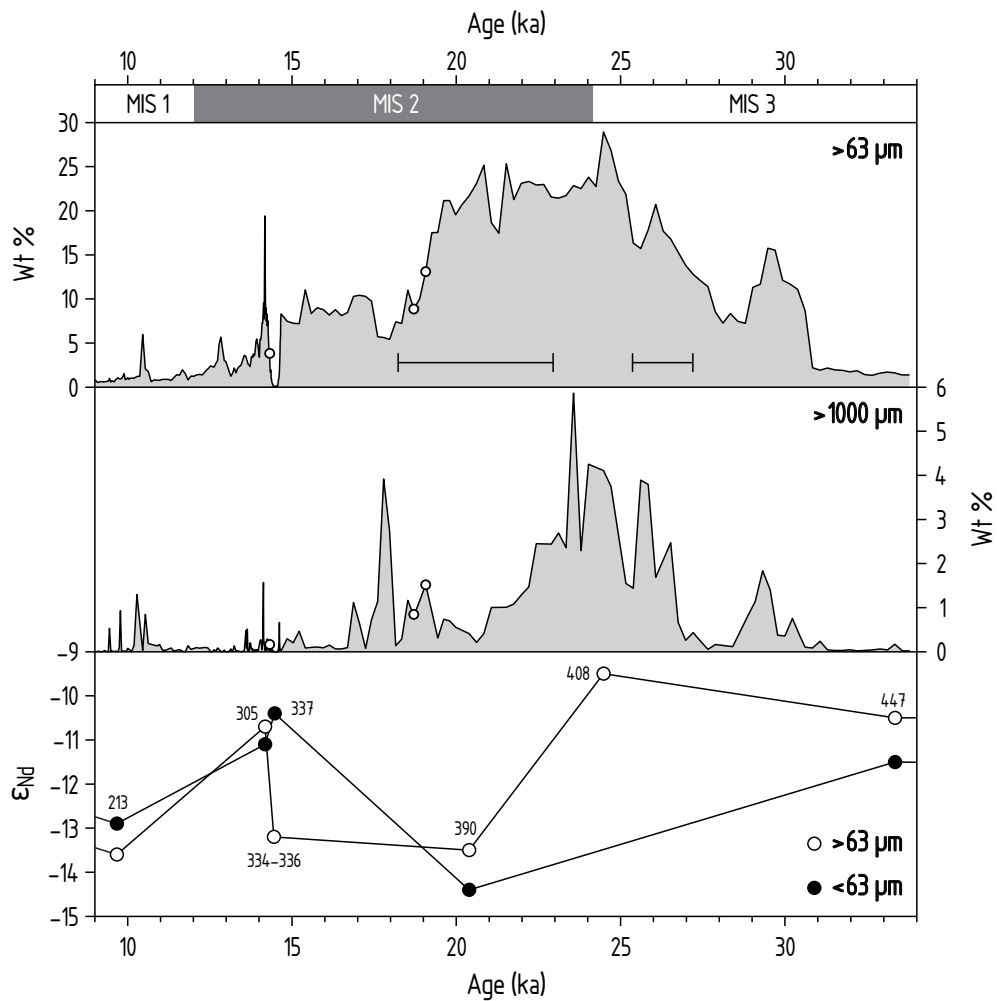
Figure 37: Downcore variation of abundance of particles > 63 μm and > 1000 μm, and ε_{Nd} val-
ues in core PS2837-5 between 34 ka and 9 ka. Open circles in the > 63 μm and > 1000
μm abundance curves mark dropstones. Horizontal black bars in the uppermost panel
mark layers where high sand contents result from abundant planktic foraminifers
(Nørgaard-Pedersen et al., 2003). Abundance data are from Hass (2000) for the frac-
tion > 63 μm, and from Hass (unpubl. data) for the fraction > 1000 μm. MIS 1, 2, and 3
are Marine Isotope Stages after Martinson et al. (1987).

ern and eastern Barents Sea. The ε_{Nd} value of -9.5 for sand sample 408 (24.5 ka) therefore
supports the assumption that the Barents Sea shelf is the major source of sediments with
radiogenic Nd isotopic compositions in core PS2837-5.

Synchronous with the advance of the ice sheet to the shelf break west of Svalbard at 22.5
ka, sedimentary records from the lower continental slope west of Svalbard reveal a major
shift in sediment provenance (Elverhøi et al., 1995); a reduction of organic carbon contents
(reduced erosion of Mesozoic rocks on Svalbard) was accompanied by a strong increase in

the abundance of crystalline IRD. Due to the limited exposure of crystalline rocks along the west coast of Spitsbergen, Elverhøi et al. (1995) assume that the crystalline IRD was mainly derived from Fennoscandia. Iceberg drift from far south is also indicated by the occurrence of chalk fragments (Elverhøi et al., 1995) diagnostic of North Sea tills and southern North Sea bedrock (Spielhagen, 1991). A chalk fragment containing Cretaceous coccoliths (E. Martini, personal communication) was also found in the fraction > 63 μm of sample 390 (20.4 ka) from core PS2837-5, proving iceberg drift from the North Sea as far north as the western Yermak Plateau. ε_{Nd} values of -13.5 and -14.4 were determined for the fractions > 63 μm and < 63 μm of sample 390, respectively. Compared to Nd isotopic compositions of mid-Norway shelf sediments (ε_{Nd} -14.8 and -15.1; Farmer and Barber, 2003), the ε_{Nd} values of fine and coarse fractions of sample 390 are consistent with a strong input from the Fennoscandian Ice Sheet. The moderate offsets towards more radiogenic values probably reflect continued, but reduced, sediment delivery from the Svalbard/Barents Sea area (Elverhøi et al., 1995).

. .   E   (– .   )

A first sign of disintegration of the Late Weichselian SBIS is found in a sudden increase of IRD in cores from the northern Barents Sea margin at ca 18.5 ka (Knies et al., 2001). Shortly afterwards, a beginning disintegration of the ice sheet in the southern Barents Sea is recorded in cores from the continental margin west of Svalbard (Elverhøi et al., 1995; Andersen et al., 1996). Triggered by a small rise in sea level that led to a destabilization of the shelf-based parts of the ice sheet, the initial phase of deglaciation was characterized by melting of icebergs (drifting with inflowing temperate Atlantic water) rather than direct meltwater run-off (Elverhøi et al., 1995). Accordingly, the prominent peak of IRD > 1000 μm at 18 ka in core PS2837-5 (Fig. 37) is interpreted to reflect increased iceberg rafting from the disintegrating, shelf-based parts of the SBIS.

A possible explanation for the significant reduction in abundance of IRD > 1000 μm at 17 ka (Fig. 37) is given by Knies et al. (2001). They suggest that great numbers of icebergs released from the fast-decaying ice sheet caused a cooling of surface waters, which slowed down the release of IRD from melting icebergs. During the same period, rare or absent 'Atlantic species' of benthic foraminifers in core PS2837-5 indicate diminished inflow of temperate Atlantic water (Wollenburg et al., 2004).

While contents of coarse IRD (> 1000 μm) in core PS2837-5 are low between 17 ka and 14.7 ka, contents of particles > 63 μm are elevated (Fig. 37). As abundances of planktic foraminifers are low during this interval (Nørgaard-Pedersen et al., 2003), the elevated sand contents most likely reflect enhanced sea ice rafting. The cooling of the surface waters mentioned above would have greatly facilitated the formation of sea ice.

. .   G   I   (.   – .)

A sudden rise of high-latitude atmospheric temperatures at 14.7 ka, recorded in oxygen isotope records from Greenland ice cores (Grootes et al., 1993), marks the beginning of the Greenland Interstadial 1 (GI-1, following the stratigraphic scheme proposed by Björck et al., 1998). This happened during a period of rapidly increasing high-northern latitude summer insolation (Laskar, 1990) and significant warming of surface temperatures in middle and northern Europe (Renssen and Isarin, 2001). The rising temperatures accelerated the decay of the SBIS, which led to the release of meltwater plumes carrying large amounts of fine-grained sediments (Elverhøi et al., 1995; Andersen et al., 1996). The strong discharge of meltwater from decaying high-latitude ice sheets may also have destabilized thermohaline circulation, which is a probable cause for a collapse of bottom currents at the western Yermak Plateau (Birgel and Hass, 2004). This collapse led to the deposition of large amounts of fine-grained sediments at the location of core PS2837-5 between 14.65 ka and 14.25 ka (Fig. 38). Iceberg rafting, however, continued during this episode, as indicated by the finding of a dropstone (Fig. 38). This iceberg rafting most probably is related to a short glacial readvance onto the shelf west of Svalbard that culminated around 14.4 ka (Elverhøi et al., 1995). On the lower continental slope west of Svalbard, sediments deposited during the early part of this glacial readvance contain both crystalline IRD and clastic-sedimentary IRD derived from the Svalbard/Barents Sea area (Elverhøi et al., 1995; Andersen et al., 1996). During the later part of the glacial readvance, only clastic sedimentary IRD is recorded. The crystalline IRD most likely was derived from the pre-Old Red basement exposed along the west coast of Spitsbergen. A Scandinavian provenance, however, cannot be excluded, as an approximately simultaneous readvance of the Fennoscandian Ice Sheet has been reported by Mangerud et al. (1979) and Vorren et al. (1988).

Nd isotopes indicate that the same sequence of events is recorded in core PS2837-5 (Fig. 38). ε_{Nd} values of -13.2 and -10.7 for the sand fractions of samples 334-336 and 305, respectively, prove an abrupt shift of IRD provenance from a mixed Svalbard-(Scandinavia)-Barents Sea source to a probably 'pure' Barents Sea source between 14.45 ka and 14.2 ka (Fig. 38). A similar shift of provenance is not found for the fractions < 63 μm of the samples 337 and 305, which have ε_{Nd} values of -10.4 and -11.1, respectively. These values are in good agreement with ε_{Nd} values of -10.1 and -11.4 for sediment samples from the Barents Sea slope in front of the Bear Island Trough (Farmer and Barber, 2003), which is a likely outlet for the above mentioned sediment-laden meltwater plumes from the Barents Sea.

Around 12.8 ka, a small peak of IRD > 63 μm (but not of IRD > 1000 μm) in core PS2837-5 marks the upper boundary of a thin layer devoid of foraminifers (R.F. Spielhagen, personal communication). Spielhagen et al. (2004) interpret similar, foraminifer free
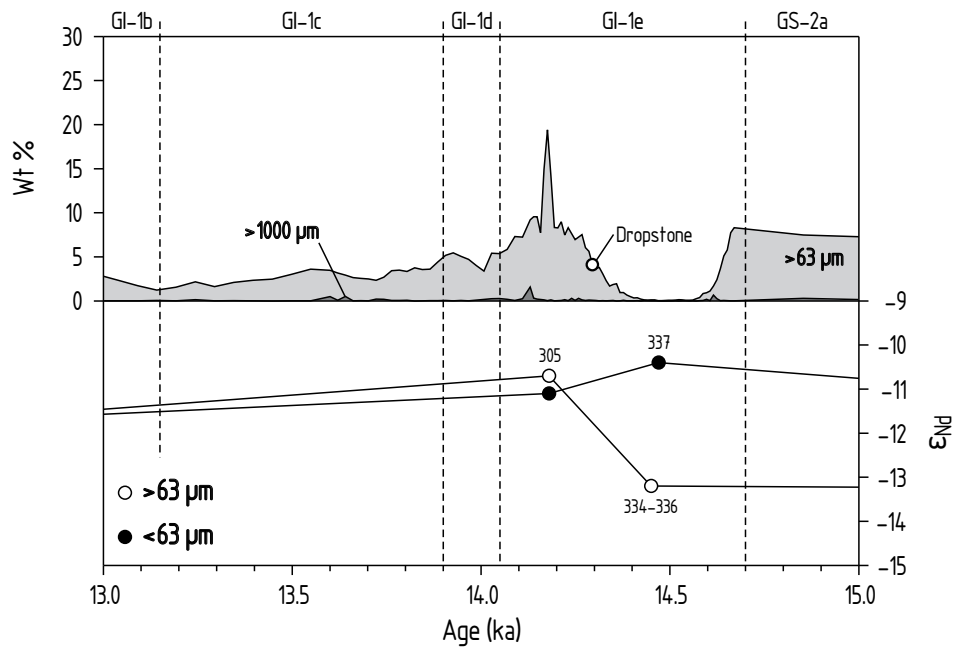
Figure 38: Downcore variation of abundance of particles > 63 μm and > 1000 μm, and ε_{Nd} values
in core PS2837-5 between 15 ka and 13 ka. Abundance data are from Hass (2000) for
the fraction > 63 μm, and from Hass (unpubl. data) for the fraction > 1000 μm. Strati-
graphic division after Björck et al. (1998): GI-1 is the warm Greenland Interstadial 1
(episodes b and d are relatively colder than episodes c and e). GS-2 is the cold Green-
land Stadial 2 (GS-2a is a particularly cold episode).

layers in cores PS1535 and PS1533 to be the result of either carbonate dissolution at the
sea floor, or a decrease of surface salinity below the tolerance limit of planktic foraminifers.
In the case of core PS2837-5, the low salinity (i.e. meltwater) scenario is the more likely
explanation, supported by a fast 1 ‰ rise of δ^{18}O values above the foraminifer free layer
(Nørgaard-Pedersen et al., 2003). The elevated sand contents are therefore likely to reflect
a period of enhanced sea ice formation and -rafting.

. .   H   (.   –   )

A small, but distinct IRD peak (both > 63 μm and > 1000 μm; Fig. 37) at 10.5 ka is the last
evidence of enhanced iceberg drift at the western Yermak Plateau, most probably reflecting
the rapid disintegration of the remaining SBIS. The age of this last iceberg rafting event
coincides with the peak of post-glacial meltwater pulse 1b (MWP 1b), during which global
sea level rose by about 28 meters (Fairbanks, 1989). Although several central Arctic Ocean
records show a MWP 1b signal (with evidence of ice sheet melting in northern Canada
and/or northern Greenland, Nørgaard-Pedersen et al., 1998), Greenland ice core records

(Grootes et al., 1993) show no indication of an interruption of the steady trend towards higher atmospheric temperatures. Similarly, the $\delta^{18}O$ record of core PS2837-5 (Nørgaard-Pedersen et al., 2003) shows no disturbance around 10.5 ka. It can therefore be assumed that MWP 1b was not connected to a strong input of meltwater to the areas of deep-water formation in the Nordic Seas. Accordingly, the raised iceberg abundance at the western Yermak Plateau probably was triggered by the rising sea level. The nature of the ice sheet(s) supplying the enormous amounts of meltwater during MWP 1a and 1b is the subject of an ongoing debate. Weaver et al. (2003) proposed an Antarctic source for MWP 1a (coeval with GI-1), which might also be an explanation for the lack of a meltwater signal in the Nordic Seas during MWP 1b.

A minor peak in the > 63 μm curve at 8.2 ka (Fig. 35) indicates a short period of increased sea ice rafting. It correlates with a prominent, widespread cooling event (Alley et al., 1997) that has been linked to a meltwater-induced weakening of thermohaline circulation (Renssen et al., 2001). Small excursions to lighter values in the $\delta^{18}O$ and $\delta^{13}C$ records of core PS2837-5 (Nørgaard-Pedersen et al., 2003), indicative of reduced salinity, support this assumption. After the 8.2 ka event, sand contents remain on a low level during the Holocene. Slightly elevated sand contents in the uppermost centimeters of the core may be related to the Little Ice Age (15th–19th century AD; Matthes, 1939; Grove, 1988).

The Holocene Nd isotope record of fractions < 63 μm from core PS2837-5 is characterized by a trend towards more radiogenic ε_{Nd} values from -12.9 for sample 213 (9.7 ka) to -11.9 for sample 55 (2 ka). This trend is even more pronounced for the fractions > 63 μm, whose ε_{Nd} values change from -13.6 for sand sample 213 to -11.1 for the core-top sample (Fig. 35). Despite the higher analytical uncertainty, the trend for the > 63 μm fractions resembles that for the < 63 μm fractions, and is therefore assumed to be at least qualitatively correct. The same trend towards more radiogenic values is also recorded in the < 63 μm fractions of samples from core PS1533 (Fig. 36). According to Tütken et al. (2002), this trend reflects increasing proportions (up to 75 %) of Eurasian shelf material from the Kara/Laptev Sea area, transported as IRD via the Trans Polar Drift. This implies that 75 % of modern sedimentation at the location of core PS1533 is related to ice rafting. While this may be a possible explanation for core PS1533 (with Holocene linear sedimentation rates on the order of 2 cm·ka^{-1}, Nørgaard-Pedersen et al., 2003), it is difficult to reconcile with the sedimentary record of core PS2837-5, which has Holocene sedimentation rates around 20 cm·ka^{-1}. A more plausible explanation for core PS2837-5 is that the Nd isotopic trend is related to a change in Atlantic water advection into the Nordic Seas, which is known to have been higher than today during the early Holocene (Polyak and Mikhailov, 1996). The weakening of Atlantic inflow might have strengthened the relative contribution from Barents Sea outflow (East Spitsbergen Current and Bear Island Current), leading to increasingly radiogenic ε_{Nd} values for the current transported component of the WSC. An interpretation of

the same trend observed for the > 63 μm fractions is less straightforward. Since icebergs can be excluded as important IRD carriers during the Holocene, a gradual shift in sea ice rafted IRD provenance is necessary to explain the gradual shift in IRD Nd isotopic composition. Although speculative, a strengthening of the East Spitsbergen Current might have increased the proportion of eastern Svalbard/north-western Barents Sea derived IRD ('radiogenic' Mesozoic rocks) relative to western Svalbard derived IRD ('unradiogenic' pre-Old Red basement).

.   S   REE   HH-

The sequential leaching experiment with aliquots of sample 712 revealed, next to the detrital and seawater REE pools, a third pool of REE. The aim of this Chapter is to show that this is not a unique feature of this sample, but may indeed be a general feature of terrigenous sediments. The implication is that HH leaching, aiming at the isolation of a pure seawater signal from terrigenous sediments, is subject to previously unrecognized restrictions; particularly so if the 'weak leach' approach is used. The rationale behind the 'weak leach' approach is that a HH solution with a low concentration of hydroxylamine hydrochloride is unlikely to attack detrital minerals, but will release sufficient Nd from authigenic ferromanganese phases for mass spectrometric analysis. The general correctness of this assumption has been confirmed by dynamic-leaching experiments performed by Dubinin and Strekopytov (2001).

Aubert et al. (2001) studied the fractionation and migration of REE during weathering of granitic bedrock in the catchment area of a small river in the french Vosges mountains. They found that the suspended load of the river corresponds to the finest fraction of the soil in the catchment area, but that its shale-normalized REE pattern shows a distinct MREE enrichment more similar to apatite from the unweathered bedrock. Leaching of the suspended load with 1 mol·l^{-1} HCl at room temperature for 15 minutes produced REE patterns even closer to apatite. The authors explain the REE pattern of the suspended load with adsorption and/or coprecipitation of REE derived from the dissolution of phosphatic minerals such as apatite and/or monazite.

Hannigan and Sholkovitz (2001) produced similar MREE enriched patterns by leaching river-bank sediments (with flat shale-normalized REE patterns) with filtered lake water at solid to liquid ratios of 1 g : 50 ml. The leaching was performed at the water's natural pH 5, and also with the same water adjusted to pH 2. While REE were continuously released during 48 hours at both acidities, the amount of REE released at pH 2 was three to four orders of magnitude higher than at pH 5. They also explained the MREE enrichment with the dissolution of phosphatic minerals.

Alibo and Nozaki (1999) presented data for REE released from acidified (pH < 1.5) samples of filtered (0.04 μm) and unfiltered seawater from different depths of a surface-to-bottom profile close to Boso Peninsula, Japan. From the difference between filtered and unfiltered water from the same depth they calculated the REE contents of the 'acid-soluble particulate' (ASP) fraction. They assume that the ASP fraction contains REE adsorbed to particles and bound in biogenic carbonate, but may exclude REE in detrital minerals. The ASP fractions from intermediate depths have flat shale-normalized REE patterns. In contrast, the two deepest samples, from within 80 meters of the sea floor, have higher overall REE abundances, and MREE enriched patterns more similar to underlying sediments.

If these findings reflect general phenomena, then terrigenous marine sediments can be expected to contain a pool of REE that (1) will be released by acidic solutions, (2) is enriched in MREE relative to the bulk sediment, (3) is not derived from seawater, but originally was hosted in phosphatic minerals in the same source rocks as the bulk of the detrital minerals, and (4) has a Nd isotopic composition more radiogenic than the bulk sediment (same initial $^{143}Nd/^{144}Nd$ ratio, but higher Sm/Nd ratio).

Note that these points match the characteristics of EM C from the sequential leaching experiment (acetic acid-soluble, Sm/Nd ratio higher than the bulk sample, Sm/Nd and ε_{Nd} distinctly different from the seawater EM B, see Fig. 28). MREE enriched REE patterns are also found in all HH leachates from core PS2837-5 analyzed by ICP-MS (see Fig. 25). In two aspects, these leachates from core PS2837-5 are similar to Fe-Mn micronodules from the central Arctic Ocean presented in Winter et al. (1997): their REE contents are low compared to typical Fe-Mn nodules, and they have similar Sm/Nd ratios (0.2110-0.2468 for PS2837-5, 0.2069-0.2544 for the central Arctic micronodules). In other aspects, however, they are distinctly different from the central Arctic Ocean Fe-Mn micronodules, which, except for their low REE contents, have characteristics typical of other hydrogenous and diagenetic marine Fe-Mn oxides (Winter et al., 1997). They have shale-normalized Gd_N/Yb_N ratios between 1.12 and 1.77 (between 2.15 and 2.89 for PS2837-5), and strong positive Ce anomalies with Ce_N/Nd_N ratios (no La and Pr data given) between 1.33 and 2.76 (between 0.82 and 0.92 for core PS2837-5). The Nd isotopic compositions of HH leachates from core PS2837-5 (more radiogenic than bulk sediment, close downcore covariation with detrital fractions, see Fig. 26) are consistent with the hypothesis that the leachates represent a pool of REE that has the same source as the bulk of the detrital minerals, but a higher Sm/Nd ratio (hosted, for instance, in apatite).

The aim of the following paragraphs is to reveal a systematic relationship between these findings and particular experimental protocols for HH leaching. Applied to the sequential leaching experiment, the results from Alibo and Nozaki (1999), Hannigan and Sholkovitz (2001), and Aubert et al. (2001) provide a reasonable explanation for the observed sequence of events.

According to the proposed model, the untreated bulk sample contains three distinct pools of REE: (1) REE fixed in the crystal lattices of non-phosphatic minerals of the terrigenous fraction (EM A, only homogeneous when treated as an entity), (2) REE contained in authigenic Fe-Mn and phosphatic phases (EM B), and (3) REE fixed in the crystal lattices of terrigenous phosphatic minerals and/or REE adsorbed to particle surfaces, but derived from the same terrigenous phosphatic minerals (EM C).

A first 18 h leaching of an aliquot of the untreated bulk sample with 1.7 mol·l^{-1} acetic acid (pH ~2.5) yielded a mix of acid-soluble EM C and particulate EM A (due to insufficient separation of the supernatant from the solid residue). A second 18 h leaching of the same sample aliquot with 1.7 mol·l^{-1} acetic acid yielded a mix of acid-soluble EM C and acid-soluble EM B. This second acetic acid leaching was sufficient to remove all of EM C, so that the first 2 h leaching with 0.2 mol·l^{-1} HH (pH ~2.5) yielded almost pure EM B (acid-soluble and/or released by reduction of Fe-Mn phases) with a small contribution of EM A (again, probably due to insufficient separation of the supernatant from the solid residue). In contrast, a single 18 h leaching of a different aliquot with buffered 0.87 mol·l^{-1} acetic acid (pH ~5) apparently removed EM C only partly, so that the first 2 h leaching with 0.2 mol·l^{-1} HH yielded a mix of EM C and EM B. This first HH leaching then removed all acid-soluble EM C remaining after the acetic acid leaching, so that a second HH leaching, lasting for 5:45 h, yielded pure EM B. A third HH leaching of the same aliquot, lasting for 20 h, yielded a mix of EM B and a significant proportion of EM A. This suggests that prolonged leaching with HH does eventually attack the crystal lattices of detrital minerals, which is supported by the position of the solid residue of this aliquot beyond EM A (see Fig. 28).

Evidently, acidity is a key factor. A HH leaching will extract a pure EM B/seawater signal only if EM C is not present, i.e. has been removed by suitable pretreatment. Otherwise the leachate will always be a mix of EM B and acid-soluble EM C. The important point is that the ability of a HH solution to release adsorbed trace elements and to dissolve particulate phosphatic phases does not depend on the reducing power of the solution, i.e. the hydroxylamine hydrochloride concentration, but its acidity, which will not change significantly with the concentration of hydroxylamine hydrochloride. This, however, appears to have so far been ignored, as all applications of HH leaching found in the literature use acetic acid concentrations of 4.4 mol·l^{-1}, as originally proposed by Chester and Hughes (1967). This particularly affects the 'weak leach' approach; a 'weak' HH solution (with a low concentration of hydroxylamine hydrochloride) will release less trace elements from ferromanganese phases than a 'strong' HH solution, but both solutions will release the same amount of trace elements from particle surfaces or particulate phosphatic phases. The 'weak leach' approach appears to actually be counterproductive.

This has implications for published data based on HH leaching. Rutberg et al. (2000) and Piotrowski et al. (2004) presented a reconstruction of North Atlantic Deep Water ex-

port variability during the last glacial–interglacial cycle based on Nd isotopic compositions of authigenic Fe-Mn phases. The Fe-Mn phases were obtained by HH leaching of sediment samples from core RC11-83 from the southern Cape Basin in the southeast Atlantic, and are assumed to reflect the Nd isotopic composition of seawater. Both studies followed the 'weak leach' approach, using 0.45 mol·l^{-1} acetic acid buffered to pH 5 and HH with 0.02 mol·l^{-1} hydroxylamine hydrochloride in 4.4 mol·l^{-1} acetic acid.

To test whether or not their HH leachates reflect seawater isotopic composition, Rutberg et al. (2000) applied two tests. They measured the ^{87}Sr/^{86}Sr ratios of the leachates, and found them to be identical to the present-day global seawater ^{87}Sr/^{86}Sr ratio of ~0.709. This, however, is a proof of seawater origin for only the Sr in the leachate, and doesn't necessarily apply to other elements (as acknowledged by the authors). The second test utilized a correlation of Nd isotope ratios with dissolved SiO$_2$ content in deep Atlantic seawater. Rutberg et al. (2000) showed that their youngest Fe-Mn leachate from core RC11-83, when
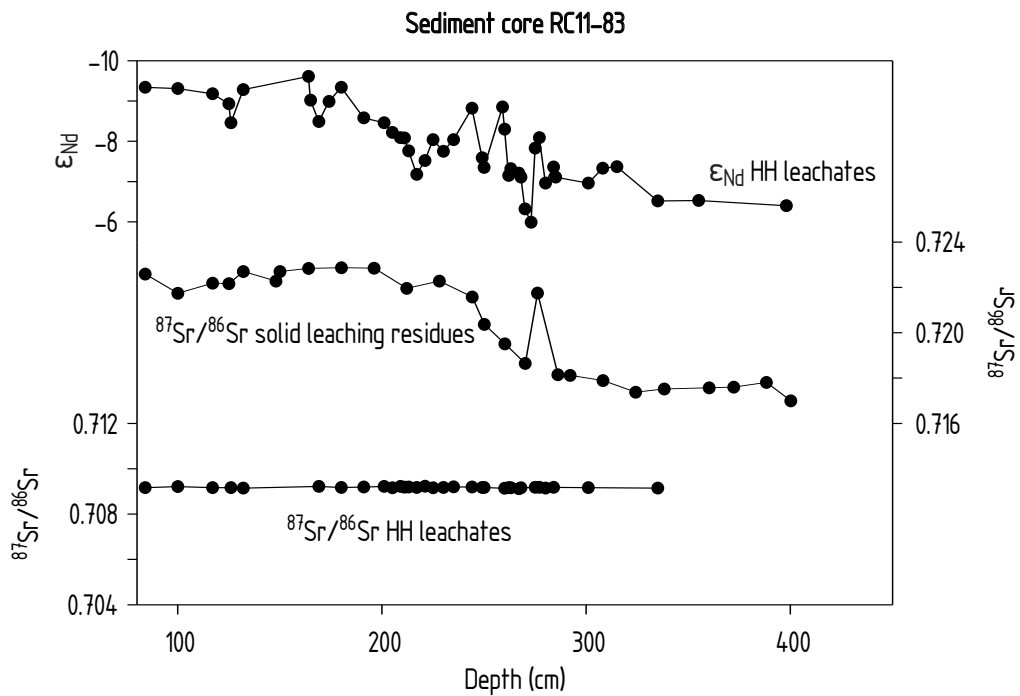
Figure 39: Downcore variation of ε_{Nd} values in HH leachates and ^{87}Sr/^{86}Sr ratios in HH leachates and solid leaching residues in sediment core RC11-83 from the southern Cape Basin in the southeast Atlantic. Note that the leachates have a uniform Sr isotopic composition identical to seawater (^{87}Sr/^{86}Sr = 0.709), but that the ε_{Nd} values of the leachates are inversely correlated with ^{87}Sr/^{86}Sr ratios of the solid leaching residues, indicating a close genetic relationship. R^2 for data pairs from identical depth is 0.8. Leachate data from Rutberg et al. (2000) and Piotrowski et al. (2004), solid residue data from Rutberg (2000).

plotted against the geographically nearest dissolved SiO_2 value from the literature, falls on the present-day Atlantic seawater dissolved $SiO_2-\varepsilon_{Nd}$ trend. They took this as evidence for a seawater origin of the Nd in the leachates. The dissolved $SiO_2-\varepsilon_{Nd}$ correlation, however, is not very well defined. Instead, it is a linearly elongated scatter of data points, approximately $2\,\varepsilon_{Nd}$ high for any given dissolved silica value, and approximately $30\,\mu mol \cdot kg^{-1}$ SiO_2 wide for any given ε_{Nd} value (see Fig. 2a in Rutberg et al., 2000). This may not be precise enough to unambiguously prove a seawater origin for the Nd in the leachates.

In fact, there is evidence that the same systematic relationship between the Nd isotopic compositions of HH leachates and detrital fractions found for core PS2837-5 also exists in core RC11-83. ε_{Nd} values for detrital fractions from core RC11-83 are not reported, but Rutberg (2000) presented $^{87}Sr/^{86}Sr$ ratios. Upper crustal rocks exposed to weathering typically have high Rb/Sr ratios but low Sm/Nd ratios, resulting in an inverse correlation of $^{87}Sr/^{86}Sr$ ratios with ε_{Nd} values. Such an inverse correlation is, for instance, well documented for detrital fractions from core PS1533 from the north-eastern Yermak Plateau (see Fig. 3 in Tütken et al., 2002). Fig. 39 reveals an inverse correlation of HH leachate ε_{Nd} with the $^{87}Sr/^{86}Sr$ ratios of the leaching residues in core RC11-83. It is therefore possible, if not likely, that the Nd isotopic compositions of the HH leachates from this core do not reflect seawater.

A different approach was used by Bayon et al. (2002), who presented results of HH leaching of sediment samples from core MD96-2086 from the northern Cape Basin. They used $1.7\,mol \cdot l^{-1}$ unbuffered acetic acid and HH with $1\,mol \cdot l^{-1}$ hydroxylamine hydrochloride in $4.4\,mol \cdot l^{-1}$ acetic acid at 90 °C. For their study, they analyzed the Nd isotopic compositions of the HH leachates, and both Nd and Sr isotopic compositions of the leaching residues (Fig. 40). In contrast to core RC11-83 (Fig. 39), the ε_{Nd} values of the leachates and the $^{87}Sr/^{86}Sr$ ratios of the residues are not correlated ($R^2 = 0.17$). However, ε_{Nd} values and
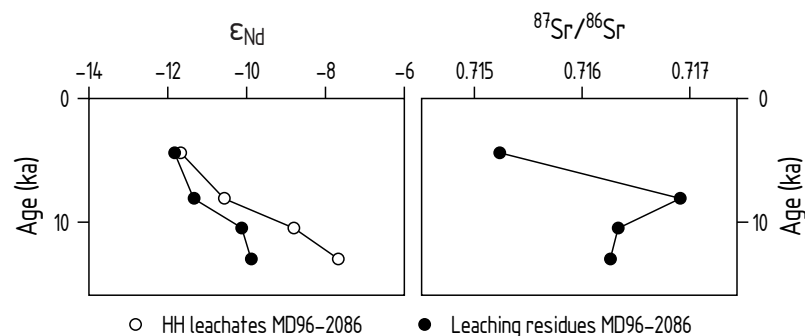
Figure 40 : Downcore variation of ε_{Nd} values and $^{87}Sr/^{86}Sr$ ratios in HH leachates and leaching residues in sediment core MD96-2086 (northern Cape Basin, southeast Atlantic). Data from Bayon et al. (2002).

^{87}Sr/^{86}Sr ratios of the residues do not show the expected inverse correlation ($R^2 = 0.16$). Instead, ε_{Nd} values of HH leachates and leaching residues show an excellent correlation ($R^2 = 0.98$), but not the near constant offset found for core PS2837-5.

To conclude, there is reason to believe that sediment leaching with HH does not yet provide a straightforward, easy-to-use method to extract a pure seawater signal. The reason is that the distribution of REE between different components of marine sediments is not yet understood well enough. The leaching procedure suited to produce meaningful results may differ from case to case, and may have to be established through extensive testing for each case individually.

C

The results of this study further unravel the Late Quaternary history of oceanographic conditions at the Yermak Plateau located in the Arctic Ocean-Atlantic gateway. The principal goal of this work was to reconstruct the provenance of sediments deposited on the western Yermak Plateau during the last 129 000 years covered by the studied sediment core PS2837-5. Samples from the core and from potential source areas were split into the grain-size fractions clay, fine silt, coarse silt, and sand, and analyzed for their Sm and Nd isotopic compositions. The rationale for analyzing distinct grain-size fractions was to monitor possible grain-size dependent differences in isotopic compositions. Such differences may arise from a combination of different sediment transport mechanisms and source areas.

The Sm–Nd isotope data suggest that, contrary to the general consensus, ice rafted detritus (IRD) deposited at the western Yermak Plateau under modern interglacial conditions was not derived from the shelf areas of the Kara- and Laptev Seas off the Siberian coast. Instead, the Nd isotopes indicate that the IRD and the suspended load of the WSC are of similar origin, and probably were derived from the Svalbard/Barents Sea area.

Regarding the Late Quaternary history of sedimentation at the western Yermak Plateau, it appears that the general modern pattern of oceanic circulation has existed for most of the last 129 000 years. Only during the Last Glacial Maximum, approximately 20 ka ago, there is a significant change in sediment provenance, as shown by the Sm–Nd isotope data. This change, however, was not caused by a reorganization of oceanic circulation. Instead, sedimentation at the core location was dominated by material derived from Scandinavia, which is located further upstream the WSC and its southern precursor, the Norwegian Atlantic Current. In at least one case, sediment was delivered from as far south as the North Sea.

A second avenue of investigation dealt with the implementation and application of a relatively novel approach for the reconstruction of seawater Nd isotopic composition with high temporal resolution. This approach utilizes authigenic Fe-Mn oxyhydroxides that are finely dispersed throughout the sediment column, mainly as coatings on foraminifers and detrital particles, and whose Nd isotopic composition is thought to faithfully record the isotopic composition of seawater. The Fe-Mn oxyhydroxides are extracted by leaching with a mixed acidic-reducing reagent of hydroxylamine-hydrochloride in acetic acid.

Using methods described in recently published studies, several samples from core PS2837-5 were processed and analyzed for their REE distributions and Nd isotopic compositions. Both REE and Nd isotope data indicate that the trace element contents of the leachates are at least partly derived from detrital phases, and thus do not yield a seawater signal: the

REE patterns of the leachates are enriched in the middle REE, which is atypical for Fe-Mn oxyhydroxides, and their Nd isotopic compositions show a close downcore covariation with the detrital fractions. This observation was further investigated by means of a sequential leaching experiment. Several aliquots of the same core sample were leached for variable durations with different concentrations of the leaching reagent. At intermediate steps throughout the process, leachates and solid residues were analyzed for their Sm–Nd isotopic compositions. The experiment revealed an insoluble, 'pure' detrital component, and two pools of REE that were released by leaching with the mixed acidic-reducing reagent. One of these presumably is the authigenic, seawater-derived component. The other pool of REE most likely was hosted in easily soluble phosphatic phases of detrital origin. Phosphatic phases, such as apatite, can account for the enrichment of the middle REE enrichment, and a detrital origin would explain the observed systematic relationship between the Nd isotopic compositions of leachates and detrital fractions. It can be concluded that the available techniques are not yet refined enough to reliably use the Nd isotopic composition of finely dispersed Fe-Mn oxyhydroxides as a proxy for paleoseawater composition.

The dominant problem appears to be associated with the acetic acid component of the leaching solution. This component was originally introduced by Chester and Hughes (1967) to increase the recovery of Fe and Mn towards a complete removal of all Fe-Mn phases from the sample. As a quantitative recovery is not necessary for Nd isotope analysis, simply dispensing with the acetic acid may be sufficient to obtain meaningful paleoseawater Nd isotopic compositions.

Table 10 : Sm and Nd abundances and isotopic compositions of size fractions of samples from sediment core PS2837-5.

Sample	Age (a)	MIS	Size fraction (μm)	wt %	Sm (μg·g^{-1})	Nd (μg·g^{-1})	Sm/Nd	^{147}Sm/^{144}Nd	^{143}Nd/^{144}Nd [†]	ε_{Nd}	T_{DM} (Ga)
PS2837-6, 1 sa	20	1	63-250		2.80	14.8	0.1892	0.1143	0.512 070 ± 12	-11.1	1.66
55 c	2000	1	< 2	50.5	7.11	37.9	0.1876	0.1133	0.512 032 ± 10	-11.8	1.70
55 c re.					6.93	36.9	0.1878	0.1136	0.512 022 ± 10	-12.0	1.72
55 fs			2-10	19.8	6.61	34.3	0.1927	0.1163	0.512 055 ± 10	-11.4	1.71
55 cs			10-63	29.1	5.00	25.5	0.1961	0.1188	0.512 002 ± 10	-12.4	1.84
55 sa			63-250	0.5	1.65	9.69	0.1703	0.1032	0.512 060 ± 11	-11.3	1.50
133 c	6660	1	< 2	50.4	6.87	37.0	0.1857	0.1122	0.512 022 ± 10	-12.0	1.69
133 fs			2-10	24.0	6.83	35.7	0.1913	0.1155	0.512 012 ± 12	-12.2	1.77
133 cs			10-63	25.0	5.25	27.2	0.1930	0.1168	0.511 998 ± 10	-12.5	1.81
133 sa			63-250	0.4	1.92	11.0	0.1745	0.1058	0.511 975 ± 11	-12.9	1.66
213 c	9670	1	< 2	46.2	7.23	39.3	0.1840	0.1112	0.511 980 ± 10	-12.8	1.74
213 fs			2-10	19.7	7.00	36.6	0.1913	0.1155	0.512 009 ± 11	-12.3	1.77
213 cs			10-63	33.1	5.20	26.9	0.1933	0.1169	0.511 948 ± 10	-13.5	1.89
213 sa			63-250	0.6	2.21	12.5	0.1768	0.1068	0.511 940 ± 11	-13.6	1.72
305 c	14 180	2	< 2	32.3	7.36	39.0	0.1887	0.1141	0.512 077 ± 13	-10.9	1.64
305 fs			2-10	16.0	7.04	37.0	0.1903	0.1150	0.512 069 ± 12	-11.1	1.67
305 cs			10-63	32.2	5.23	27.5	0.1902	0.1148	0.512 053 ± 12	-11.4	1.69
305 sa			63-250	18.7	3.38	17.9	0.1888	0.1143	0.512 090 ± 13	-10.7	1.63

Table 10 : ...continued

Sample	Age (a)	MIS	Size fraction (μm)	wt %	Sm (μg·g^{-1})	Nd (μg·g^{-1})	Sm/Nd	^{147}Sm/^{144}Nd	^{143}Nd/^{144}Nd†	ε_{Nd}	T_{DM} (Ga)
334-336 sa	14 450	2	63-250	⌀ 0.1	2.31	12.2	0.1893	0.1145	0.511 960 ± 12	-13.2	1.83
337 c	14 470	2	< 2	55.6	6.91	36.8	0.1878	0.1136	0.512 100 ± 09	-10.5	1.60
337 fs			2-10	25.5	7.23	37.0	0.1954	0.1182	0.512 116 ± 11	-10.2	1.65
337 cs			10-63	18.9	5.37	26.6	0.2019	0.1219	0.512 114 ± 10	-10.2	1.72
390 c	20 390	2	< 2	48.0	7.82	42.8	0.1827	0.1106	0.511 887 ± 10	-14.6	1.87
390 c re.					7.99	43.7	0.1828	0.1104	0.511 893 ± 11	-14.5	1.85
390 fs			2-10	15.0	6.78	35.5	0.1910	0.1156	0.511 925 ± 10	-13.9	1.90
390 cs			10-63	15.3	4.85	24.2	0.2004	0.1209	0.511 921 ± 10	-14.0	2.02
390 sa			63-250	17.8	1.39	7.31	0.1902	0.1154	0.511 946 ± 18	-13.5	1.86
408 sa	24 480	3	63-250	17.2	2.78	14.2	0.1958	0.1178	0.512 150 ± 13	-9.5	1.59
447 c	33 340	3	< 2	54.9	7.34	38.3	0.1916	0.1159	0.512 050 ± 12	-11.5	1.71
447 fs			2-10	20.8	6.33	33.4	0.1895	0.1148	0.512 050 ± 14	-11.5	1.69
447 cs			10-63	22.6	4.97	25.7	0.1934	0.1170	0.512 050 ± 11	-11.5	1.73
447 sa			63-250	1.4	1.58	8.59	0.1839	0.1111	0.512 101 ± 10	-10.5	1.56
487 c	42 430	3	< 2	43.9	8.45	43.3	0.1952	0.1180	0.512 046 ± 12	-11.5	1.76
487 fs			2-10	19.4	6.91	36.3	0.1904	0.1153	0.512 063 ± 10	-11.2	1.68
487 cs			10-63	33.2	5.00	25.5	0.1961	0.1185	0.512 012 ± 10	-12.2	1.82
487 sa			63-250	3.4	2.54	13.5	0.1881	0.1136	0.512 098 ± 13	-10.5	1.60
487 sa re.									0.512 061 ± 11	-11.3	

Table 10 : . . . continued

Sample	Age (a)	MIS	Size fraction (μm)	wt %	Sm (μg·g⁻¹)	Nd (μg·g⁻¹)	Sm/Nd	^{147}Sm/^{144}Nd	^{143}Nd/^{144}Nd [†]	ε_{Nd}	T_{DM} (Ga)
557 sa	58 330	3	63-250	0.1	2.84	15.5	0.1832	0.1108	0.511 991 ± 13	-12.6	1.72
558 c	58 560	3	< 2	49.9	7.39	39.5	0.1871	0.1132	0.512 034 ± 13	-11.8	1.69
558 fs			2-10	23.2	7.12	37.1	0.1919	0.1161	0.512 054 ± 11	-11.4	1.71
558 cs			10-63	26.8	5.07	26.1	0.1943	0.1173	0.512 042 ± 10	-11.6	1.75
601 sa	68 330	4	63-250	9.0	2.27	12.1	0.1876	0.1140	0.512 051 ± 13	-11.5	1.68
623 c	73 330	4	< 2	44.8	7.32	39.9	0.1835	0.1109	0.511 961 ± 10	-13.2	1.76
623 fs			2-10	16.6	6.44	33.7	0.1911	0.1156	0.511 981 ± 09	-12.8	1.81
623 cs			10-63	33.8	4.94	24.8	0.1992	0.1203	0.512 002 ± 11	-12.4	1.87
623 sa			63-250	4.5	2.13	11.2	0.1902	0.1148	0.512 103 ± 10	-10.4	1.61
623 sa re.					1.54	8.87	0.1736	0.1049	0.511 909 ± 11	-14.2	1.74
668 c	83 560	5	< 2	49.6	7.20	39.4	0.1827	0.1104	0.511 998 ± 10	-12.5	1.70
668 fs			2-10	22.5	7.10	37.1	0.1914	0.1155	0.511 986 ± 10	-12.7	1.81
668 cs			10-63	27.5	5.39	27.3	0.1974	0.1193	0.511 946 ± 10	-13.5	1.94
668 cs re.					5.65	28.7	0.1969	0.1189	0.511 980 ± 11	-12.8	1.88
668 sa			63-250	0.4	1.65	9.83	0.1679	0.1015	0.512 007 ± 10	-12.3	1.55
712 c	93 550	5	< 2	46.0	7.13	39.0	0.1828	0.1106	0.511 979 ± 10	-12.9	1.73
712 fs			2-10	23.6	7.02	37.0	0.1897	0.1148	0.511 980 ± 10	-12.8	1.80
712 cs			10-63	28.3	5.68	29.4	0.1932	0.1170	0.511 983 ± 09	-12.8	1.84
712 sa			63-250	1.3	2.70	16.0	0.1688	0.1022	0.511 977 ± 11	-12.9	1.60

Table 10 : . . . continued

Sample	Age (a)	MIS	Size fraction (μm)	wt %	Sm (μg·g^{-1})	Nd (μg·g^{-1})	Sm/Nd	^{147}Sm/^{144}Nd	^{143}Nd/^{144}Nd †	ε_{Nd}	T$_{DM}$ (Ga)
789 c	111 050	5	< 2	40.6	7.74	41.7	0.1856	0.1121	0.512 008 ± 09	-12.3	1.71
789 fs			2-10	15.1	7.06	36.9	0.1913	0.1156	0.512 001 ± 08	-12.4	1.78
789 cs			10-63	37.6	5.05	25.9	0.1950	0.1179	0.511 971 ± 09	-13.0	1.87
789 sa			63-250	5.1	2.72	14.9	0.1826	0.1107	0.511 976 ± 12	-12.9	1.74
846 c	124 000	5	< 2	33.4	7.66	41.5	0.1846	0.1116	0.512 005 ± 10	-12.3	1.71
846 fs			2-10	14.4	6.56	34.2	0.1918	0.1158	0.512 028 ± 13	-11.9	1.75
846 cs			10-63	49.2	5.04	25.6	0.1969	0.1191	0.511 994 ± 12	-12.6	1.86
846 sa			63-250	1.9	3.65	20.1	0.1807	0.1090	0.511 980 ± 10	-12.8	1.70
868 c	129 000	5	< 2	44.0	7.35	40.2	0.1828	0.1107	0.512 035 ± 10	-11.8	1.65
868 fs			2-10	19.0	6.75	34.8	0.1940	0.1172	0.512 046 ± 10	-11.5	1.74
868 cs			10-63	35.3	5.21	26.1	0.1996	0.1204	0.512 027 ± 12	-11.9	1.83
868 sa			63-250	1.5	2.44	13.9	0.1755	0.1058	0.511 995 ± 11	-12.5	1.63

c = clay, fs = fine silt, cs = coarse silt, sa = sand; re. = replicates obtained from separate sample aliquots. MIS = Marine Isotope Stages after Martinson et al. (1987). † Within-run precision (2σ$_m$) refers to the last significant digits.

Table 11 : Sm and Nd abundances and isotopic compositions of modern samples from potential source areas of sediments in the Arctic Ocean.

Sample	Geographical location	Size fraction (μm)	wt %	Sm (μg·g^{-1})	Nd (μg·g^{-1})	Sm/Nd	^{147}Sm/^{144}Nd	^{143}Nd/^{144}Nd [†]	ε_{Nd}	T_{DM} (Ga)
Lena River delta, river bed surface sediment										
L17 cs	72° 23′ N, 126° 53′ E	10-63	13.5	6.87	39.4	0.1744	0.1055	0.511 862 ± 09	-15.1	1.81
L17 sa		63-250	55.1	3.01	17.5	0.1720	0.1039	0.511 873 ± 10	-14.9	1.77
L18	72° 16′ N, 127° 52′ E	250-500		1.85	11.8	0.1568	0.0949	0.511 787 ± 18	-16.6	1.75
L20	72° 01′ N, 129° 08′ E	250-500						0.511 820 ± 14	-16.0	
L21		225-500						0.511 781 ± 11	-16.7	
L22 c	72° 21′ N, 126° 32′ E	< 2	8.7	11.2	59.8	0.1880	0.1137	0.511 865 ± 11	-15.1	1.96
L22 fs		2-10	14.8	9.26	50.2	0.1845	0.1115	0.511 876 ± 11	-14.9	1.90
L22 cs		10-63	39.4	6.65	36.4	0.1827	0.1103	0.511 887 ± 11	-14.6	1.86
L22 sa		63-250	37.1	3.95	22.8	0.1732	0.1048	0.511 842 ± 12	-15.5	1.83
Ob River estuary, river bed surface sediment										
BP01/72 c	70° 51.06′ N, 73° 43.06′ E	< 2	19.5	6.15	30.8	0.1997	0.1206	0.512 281 ± 11	-7.0	1.42
BP01/72 c re.			19.5					0.512 273 ± 26	-7.1	
BP01/72 sil		2-63	26.4	6.24	32.7	0.1908	0.1153	0.512 172 ± 12	-9.1	1.52
BP01/72 sa		63-250	54.1	1.57	8.64	0.1817	0.1098	0.512 194 ± 11	-8.7	1.40
Yenisei River estuary, river bed surface sediment										
BP00/15 c	72° 02.99′ N, 81° 36.16′ E	< 2	9.0	7.16	34.4	0.2081	0.1257	0.512 304 ± 13	-6.5	1.47
BP00/15 sil		2-63	85.7	3.77	18.0	0.2094	0.1266	0.512 314 ± 10	-6.3	1.46
BP00/15 sa		63-250	5.3	2.35	11.3	0.2080	0.1258	0.512 320 ± 12	-6.2	1.44

Table 11 : ...continued

Sample	Geographical location	Size fraction (μm)	wt %	Sm (μg·g^{-1})	Nd (μg·g^{-1})	Sm/Nd	^{147}Sm/^{144}Nd	^{143}Nd/^{144}Nd [†]	ε_{Nd}	T_{DM} (Ga)
Kongsfjorden (west Spitsbergen), beach deposit										
WoA	78° 57.80′ N, 11° 24.30′ E	< 63	100	6.09	32.6	0.1868	0.1128	0.511 732 ± 12	-17.7	2.14
WoA re.								0.511 727 ± 13	-17.8	
WoF	79° 00.55′ N, 11° 57.24′ E	< 500	39.2	3.05	15.8	0.1930	0.1168	0.511 876 ± 13	-14.9	2.00
WoF re.								0.511 888 ± 13	-14.6	
WoG	79° 08.71′ N, 11° 35.72′ E	< 500	28.0	1.63	8.76	0.1861	0.1128	0.511 840 ± 12	-15.6	1.98
WoG re.								0.511 862 ± 13	-15.1	
Isfjorden (west Spitsbergen), beach deposit										
WoC	78° 16.54′ N, 13° 55.39′ E	< 63	100	7.88	40.2	0.1960	0.1186	0.511 987 ± 12	-12.7	1.86
WoC re.								0.512 000 ± 12	-12.4	
WoD	78° 23.06′ N, 14° 24.96′ E	< 63	100	8.68	47.0	0.1847	0.1116	0.511 929 ± 12	-13.8	1.82
WoD re.								0.511 949 ± 14	-13.4	
WoE	78° 04.84′ N, 14° 00.15′ E	< 63	100	7.82	41.3	0.1893	0.1145	0.511 966 ± 12	-13.1	1.82
WoE re.								0.511 986 ± 10	-12.7	

Table 11 : ...continued

Sample	Geographical location	Size fraction (μm)	wt %	Sm (μg·g⁻¹)	Nd (μg·g⁻¹)	Sm/Nd	^{147}Sm/^{144}Nd	^{143}Nd/^{144}Nd [†]	ε_{Nd}	T_{DM} (Ga)
Fram Strait sea ice IRD										
Ice 80-30	80° 30´ N, 02° E	bulk						0.512 166 ± 15	-9.2	
K3-1 c	79° 11.97´ N, 02° 40.34´ E	< 2	9.3	4.55	25.8	0.1764	0.1066	0.512 063 ± 13	-11.2	1.55
K3-1 cs		10-63	74.4	6.12	33.5	0.1827	0.1105	0.512 021 ± 14	-12.0	1.67
K5-2 c	78° 57.99´ N, 00° 39.28´ E	< 2	14.8	2.52	11.6	0.2172	0.1318	0.512 331 ± 13	-6.0	1.53
K5-2 fs		2-10	18.4	5.03	25.9	0.1942	0.1175	0.512 223 ± 13	-8.1	1.47
K5-2 cs		10-63	63.9	5.07	26.6	0.1906	0.1152	0.512 142 ± 14	-9.7	1.56
K5-2 sa		> 63	2.9	2.82	14.3	0.1972	0.1193	0.512 304 ± 14	-6.5	1.37
K6-1	79° 02.06´ N, 02° 02.31´ W	bulk		6.48	34.5	0.1878	0.1136	0.511 982 ± 13	-12.8	1.78
K6-2	78° 46.93´ N, 02° 00.10´ W	bulk			24.7			0.512 286 ± 12	-6.9	

c = clay, fs = fine silt, cs = coarse silt, sil = silt, sa = sand; re. = replicates obtained from separate sample aliquots. [†] Within-run precision (2σ$_m$) refers to the last significant digits.

Table 12 : REE concentrations (μg·g^{-1}) in the HH-leachable fractions, leaching residues, and corresponding bulk samples from sediment core PS2837-5, determined by ICP-MS in Bristol. Continued on next page.

	HH-leachable fraction						
	213	213/2	390	623	623/2	668	789
La	46.3	47.0	43.4	73.8	72.2	50.4	48.8
Ce	115	120	108	197	191	127	140
Pr	13.8	14.3	12.5	21.9	21.5	15.5	15.9
Nd	59.0	62.0	52.6	91.5	88.9	66.3	68.1
Sm	12.9	15.3	11.1	20.1	21.1	16.1	15.6
Eu	2.97	3.16	2.35	4.38	4.07	3.49	3.58
Gd	13.1	14.2	10.6	19.5	18.2	15.5	15.4
Tb	1.83	1.83	1.51	2.70	2.58	2.18	2.33
Dy	10.0	9.92	8.42	14.6	13.2	12.1	11.6
Ho	1.69	1.70	1.43	2.48	2.16	2.15	1.92
Er	4.23	4.17	3.85	6.33	5.60	5.55	4.99
Tm	0.533	0.524	0.504	0.771	0.648	0.697	0.579
Yb	2.74	3.29	2.98	4.70	3.94	4.23	3.41
Lu	0.349	0.365	0.433	0.655	0.536	0.62	0.482
ΣREE	284	298	260	460	446	322	333
La$_N$/Yb$_N$	1.25	1.05	1.08	1.16	1.35	0.88	1.06
La$_N$/Sm$_N$	0.52	0.45	0.57	0.53	0.50	0.45	0.45
Ce/Ce*	1.05	1.07	1.07	1.13	1.12	1.05	1.16
wt %	10.2	7.8	15.4	8.8	12.5	11.8	9.1

Subscript 'N' denotes PAAS normalization. PAAS values are from McLennan (1989).

Ce/Ce* = Ce$_N$/(La$_N$·Pr$_N$)$^{1/2}$. wt % = maximum estimate for the mass of leachable fraction relative to original aliquot mass, based on weight loss during leaching.

Table 12 : . . . continued

	Leaching residues						
	213	213/2	390	623	623/2	668	789
La	24.0	32.0	17.2	27.7	28.4	19.2	30.3
Ce	48.9	64.7	38.0	56.7	57.3	41.5	61.6
Pr	6.00	7.14	4.62	6.65	6.43	5.07	7.16
Nd	22.1	25.3	17.1	24.1	22.7	18.7	25.5
Sm	3.98	4.26	3.04	4.25	3.73	3.26	4.44
Eu	0.863	0.837	0.653	0.886	0.732	0.714	0.936
Gd	3.30	3.19	2.63	3.47	2.94	2.76	3.69
Tb	0.457	0.477	0.393	0.494	0.440	0.415	0.500
Dy	2.80	2.82	2.39	2.94	2.75	2.56	2.97
Ho	0.544	0.556	0.481	0.588	0.562	0.542	0.580
Er	1.71	1.85	1.48	1.77	1.77	1.71	1.83
Tm	0.268	0.281	0.225	0.265	0.291	0.266	0.272
Yb	1.81	2.15	1.62	1.90	1.92	1.91	1.96
Lu	0.274	0.314	0.234	0.286	0.284	0.279	0.278
ΣREE	117	146	90	132	130	99	142
La_N/Yb_N	0.98	1.10	0.78	1.08	1.09	0.74	1.14
La_N/Sm_N	0.88	1.09	0.82	0.95	1.11	0.86	0.99
$Ce/Ce^\star$	0.94	0.99	0.98	0.96	0.98	0.97	0.96
wt %	89.8	92.2	84.6	91.2	87.5	88.2	90.9

wt % = mass of leaching residue relative to original aliquot mass.

Table 12 : ...continued

	Untreated bulk samples						
	213	213 re.	390	623	623 re.	668	789
La	33.3	33.4	35.8	34.9	34.4	38.3	33.7
Ce	68.3	69.9	74.9	74.2	74.2	80.5	72.8
Pr	8.05	8.15	8.68	8.57	8.49	9.39	8.32
Nd	31.1	31.2	32.6	32.2	31.8	35.0	31.1
Sm	6.10	6.27	6.13	5.95	6.11	6.45	5.88
Eu	1.28	1.26	1.27	1.25	1.28	1.37	1.27
Gd	4.96	5.11	5.19	5.18	5.05	5.59	4.93
Tb	0.669	0.661	0.656	0.686	0.688	0.769	0.671
Dy	3.69	3.82	4.03	3.85	3.78	4.22	3.71
Ho	0.706	0.699	0.712	0.716	0.706	0.772	0.702
Er	2.02	2.04	2.08	2.00	1.96	2.27	1.88
Tm	0.300	0.308	0.289	0.301	0.268	0.326	0.268
Yb	1.81	1.98	2.02	1.96	1.90	2.05	1.76
Lu	0.269	0.281	0.281	0.291	0.268	0.295	0.265
ΣREE	163	165	175	172	171	187	167
La_N/Yb_N	1.36	1.25	1.31	1.31	1.34	1.38	1.41
La_N/Sm_N	0.79	0.77	0.85	0.85	0.82	0.86	0.83
$Ce/Ce^\star$	0.96	0.98	0.98	0.99	1.00	0.98	1.00

re. = repeated measurement of the same sample solution.

Table 13: Nd isotopic compositions of the HH-leachable fractions of bulk
samples from sediment core PS2837-5.

Sample	Age (a)	MIS	^{143}Nd/^{144}Nd [†]	ε_{Nd}
133	6660	1	0.512 080 ± 10	-10.9
213	9670	1	0.512 070 ± 11	-11.1
337	14 470	2	0.512 149 ± 11	-9.5
374	17 420	2	0.512 103 ± 11	-10.4
390	20 390	2	0.511 974 ± 12	-13.0
447	33 340	3	0.512 159 ± 11	-9.3
601	68 330	4	0.512 080 ± 10	-10.9
623	73 330	4	0.512 054 ± 09	-11.4
789	111050	5	0.512 089 ± 12	-10.7

MIS = Marine Isotope Stages after **Martinson** et al. (1987). [†] Within-run
precision ($2\sigma_m$) refers to the last significant digits.

Table 14: Results for the sequential leaching experiment with aliquots of the untreated bulk sam-
ple PS2837-5/712. Sm and Nd abundances are given as per cent relative to the original
aliquot instead of concentrations, because meaningful leachate weights could not be
determined.

Sample	Residual mass (%)	Sm recovery (%)	Nd recovery (%)	Sm/Nd	^{143}Nd/^{144}Nd [†]	ε_{Nd}
Untreated bulk sample: 6.52 µg·g^{-1} Sm, 35.0 µg·g^{-1} Nd				0.1863	0.512 016 ± 13	-12.1
#2 solid residue	89	93	95	0.1820	0.512 004 ± 16	-12.4
#3 solid residue	86	74	82	0.1678	0.511 984 ± 13	-12.8
#4/1st HH		12	8	0.2749	0.512 140 ± 13	-9.7
#4/2nd HH		7	5	0.2509	0.512 172 ± 20	-9.1
#4/3rd HH		4	3	0.2283	0.512 101 ± 22	-10.5
#4 solid residue	86	69	78	0.1640	0.511 971 ± 13	-13.0
#6/1st HOAc		13	9	0.2483	0.512 032 ± 15	-11.8
#6/2nd HOAc		6	4	0.2866	0.512 120 ± 24	-10.1
#6/1st HH		10	8	0.2404	0.512 154 ± 31	-9.4
#6 solid residue	87	78	85	0.1699	0.511 995 ± 13	-12.5

Residual mass is relative to original aliquot. Sm and Nd recovery are relative to original aliquot,
based on concentrations determined for the untreated bulk sample. [†] Within-run precision ($2\sigma_m$)
refers to the last significant digits.
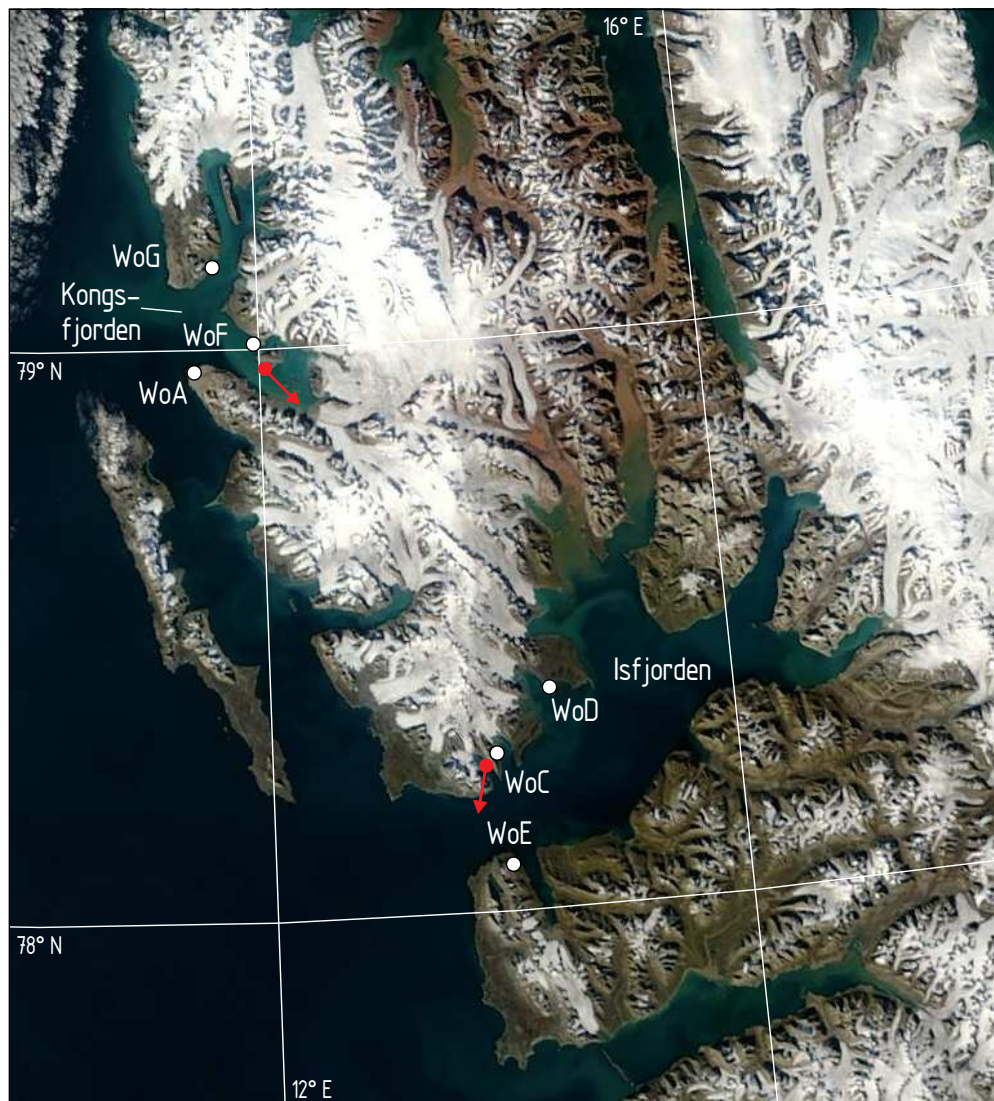
Figure 41 : Satellite image of western Spitsbergen (part of a larger image showing the entire Svalbard archipelago). White dots indicate sampling sites of Spitsbergen beach deposits. Red dots and arrows indicate place and direction of view of photographs of Kongsfjorden (Fig. 42, p. 98) and Isfjorden (Fig. 43, p. 98). Original image courtesy of MODIS Rapid Response Project at NASA/GSFC (2003/239 - 08/27, 13:00 UTC, Satellite Terra. Pixel size 250 m. Center of image 79° N, 20° E).

Figure 42 : Inner part of Kongsfjorden as seen from Blomstrand Halvøya, looking south-east. Terminus of the Kronebreen glacier in the distance. Photograph by Olivier Paris.

Figure 43: View south across Protektorfjellet and Isfjorden. Kapp Linné in the distance. Photograph by Nils Berglund.

Figure 44 : Sampling site of the Fram Strait IRD sample K3-1. Photograph by
Christoph Kierdorf.

Expedition:	ARK-XVIII/1, *RV Polarstern*
Station Nr.:	3-1
Date:	2002/08/08
Latitude:	79° 11.97´ N
Longitude:	02° 40.34´ E
Description:	white, partly dirty multi-year sea ice; dimensions: ~60 m $\times$ 55 m, average thickness > 1 m; surface: 55 % snow, 0 % ice, 5 % pressure ridges, 35 % meltwater ponds, 5 % sediment (frozen in)
Source:	Christoph Kierdorf, personal communication

Figure 45 : Sampling site of the Fram Strait IRD sample K5-2. Photograph by
Christoph Kierdorf.

Expedition: ARK-XVIII/1, *RV Polarstern*
Station Nr.:   5-2
Date: 2002/08/12
Latitude: 78° 57.99´ N
Longitude: 00° 39.28´ E
Description: white multi-year sea ice; dimensions: ~40 m ×25 m, average
                thickness > 3 m; surface: 64 % snow, 0 % ice, 1 % pressure ridges,
                30 % meltwater ponds, 5 % sediment (surficial)
Source: Christoph Kierdorf, personal communication

Figure 46 : Sampling site of the Fram Strait IRD sample K6-1. Photograph by
Christoph Kierdorf.

Expedition: ARK-XVIII/1, *RV Polarstern*
Station Nr.:   6-1
Date: 2002/08/13
Latitude: 79° 02.06´ N
Longitude: 02° 02.31´ W
Description: dirty multi-year sea ice, multiple cracks; dimensions: ~50 m ×30 m,
                 average thickness > 1.5 m; surface: 78 % snow, 0 % ice, 2 % pressure
                 ridges, 10 % meltwater ponds, 10 % sediment (surficial)
Source: Christoph Kierdorf, personal communication

Figure 47 : Sampling site of the Fram Strait IRD sample K6-2. Photograph by
Christoph Kierdorf.

Expedition: ARK-XVIII/1, *RV Polarstern*
Station Nr.:   6-2
Date: 2002/08/13
Latitude: 78° 46.93´ N
Longitude: 02° 00.10´ W
Description: light blue–greenish multi-year sea ice; dimensions: ~7 km ×3.5 km,
                 average thickness > 3 m; surface: 84 % snow, 0 % ice, 5 % pressure ridges,
                 10 % meltwater ponds, 1 % sediment (surficial)
Source: Christoph Kierdorf, personal communication

Redrawn from Stein and Fahl (1997).

Giant Box core PS2837–6 Recovery 0.49 m	Yermak Plateau 81° 14.0´ N, 02° 25.0´ E	ARK–XIII/2 Water depth: 1027 m

Lithology	Description
	0–5 cm: dark brown, silty clay, gradual boundary, bioturbated
	5–7 cm: dark brown, clayey silty mud, sharp boundary (oxidized layer)
	7–9 cm: dark grayish brown, silty clay, gradual boundary
	9–49 cm: dark olive gray, silty clay, homogenous

Depth in core (m)

0

1
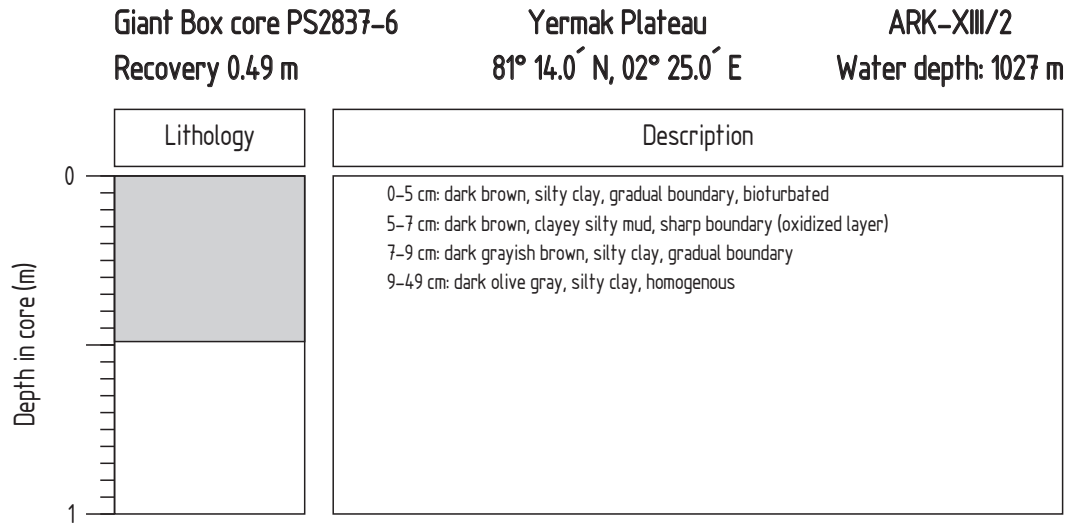
Kastenlot core PS2837–5
Recovery 8.76 m

Yermak Plateau
81° 13.99´ N, 02° 22.85´ E

ARK–XIII/2
Water depth: 1042 m

Lithology	Description

Depth in core (m)

0

1

2

3

4

Uppermost 9 cm of the core are destroyed, correlation with PS2837–6

9–207 cm: dark olive gray silty–clay, homogenous, gradual lower boundary

207–258 cm: dark olive gray silty–clay, homogenous with numerous black sulphide spots (1mm to 10mm), lower boundary gradual

258–278 cm: dark olive gray silty–clay, homogenous, gradual lower boundary

278–326 cm: dark olive gray silty–clay, homogenous with numerous black sulphide spots (1mm to 10mm), lower boundary gradual

326–354 cm: dark olive gray silty–clay, homogenous with few black sulphide spots (1mm to 3mm), lower boundary gradual

354–386 cm: dark olive gray silty–clay, homogenous with numerous black sulphide spots (1mm to 10mm), lower boundary gradual

386–405 cm: gray, sandy–silty–clayey mud, yellowish–reddish spots of limonite (402.5 cm), sharp boundaries. Sediments are coarser than overlying sediments, abundant foraminifers

405–409.5 cm: olive, clayey–sandy silt, "cottage–cheese" structure, mottling, sharp boundaries

412 cm: dropstone (black sandstone)

409.5–416 cm: very dark gray, sandy–clayey silt, homogenous, sharp boundaries

416–453 cm: colour banding: olive gray, dark yellowish brown, brown, sandy–clayey silty mud, rare specks of sulphides, sharp boundaries

Kastenlot core PS2837–5	Yermak Plateau	ARK–XIII/2
Recovery 8.76 m	81° 13.99´ N, 02° 22.85´ E	Water depth: 1042 m

Lithology	Description

Depth in core (m)

453–564 cm: dark olive gray silty–clay, homogenous, gradual boundary

564–611 cm: dark olive gray (s.a.), silty–clay with small specks and spots of sulphides, sharp boundary

611–632 cm: colour banding: olive gray, dark yellowish brown, sandy–clayey–silty mud, sharp boundaries

632–653 cm: dark olive gray, silty–clay with a few amount of sand, homogenous, gradual boundary, black spots appear in underlying deposits

653–700 cm: dark olive gray (s.a.), silty–clay, black sulphides (5–15 mm thick), boundaries are gradual

700–782 cm: olive gray, silty–clay interbedding with lenses (5–15 mm thick) of black sulphides, gradual boundary

782–828 cm: olive gray (s.a.), silty–clay with a few amount of sand. The layer contains much less spots and lenses of black sulphides than overlying and underlying deposits, gradual boundaries

828–876 cm: olive gray (s.a.), silty–clay interbedding with thin (5–10 mm) and thick (20–30 mm) lenses of black sulphides

The whole intervall of 632–876 cm shows one sequence of deposits with various amounts of sulphides

R

Aagaard K. and Carmack E.C. (1989). The role of sea ice and other fresh water in the arctic circulation. *Journal of Geophysical Research* 94 (C10), 14485–14489.

Alibo D.S. and Nozaki Y. (1999). Rare earth elements in seawater: Particle association, shale-normalization, and Ce oxidation. *Geochimica et Cosmochimica Acta* 63 (3/4), 363–372.

Alley R., Mayewski P.A., Sowers T., Stuiver M., Taylor K.C., and Clark P.U. (1997). Holocene climate instability: a prominent widespread event 8200 yr ago. *Geology* 25, 483–486.

Alley R.B. (2000). The Two-Mile Time Machine: ice cores, abrupt climate change, and our future. Princeton University Press.

AMAP (1998). AMAP Assessment Report: Arctic Pollution Issues. Arctic Monitoring and Assessment Programme (AMAP). Oslo, Norway.

Andersen E.S., Dokken T.M., Elverhøi A., Solheim A., and Fossen I. (1996). Late Quaternary sedimentation and glacial history of the western Svalbard continental margin. *Marine Geology* 133, 123–156.

Anderson L.G., Björk G., Holby O., Jones E.P., Kattner G., Koltermann K.P., Liljeblad B., Lindegren R., Rudels B., and J.Swift (1994). Water masses and circulation in the Eurasian Basin: results from the Oden91 North Pole Expedition. *Journal of Geophysical Research* 99 (C 2), 3273–3283.

Arndt N., Lehnert K., and Vasil'ev Y. (1995). Meimechites: highly magnesian lithosphere-contaminated alkaline magmas from deep subcontinental mantle. *Lithos* 34, 41–59.

Aubert D., Stille P., and Probst A. (2001). REE fractionation during granite weathering and removal by waters and suspended loads: Sr and Nd isotopic evidence. *Geochimica et Cosmochimica Acta* 3, 387–406.

Baumann M. (1990). Coccoliths in sediments of the Eastern Arctic Basin. In Bleil U. and Thiede J. (Eds.), Geological History of the Polar Oceans: Arctic versus Antarctic. NATO ASI Series C, Vol. 308. Kluwer Academic Publishers, Dordrecht, 437–445.

Bayon G., German C.R., Boella R.M., Milton J.A., Taylor R.N., and Nesbitt R.W. (2002). An improved method for extracting marine sediment fractions and its application to Sr and Nd isotopic analysis. *Chemical Geology* 187 (3-4), 179–199.

Bayon G., German C.R., Burton K.W., Nesbitt R.W., and Rogers N. (2004). Sedimentary Fe-Mn oxyhydroxides as paleoceanographic archives and the role of aeolian flux in regulating oceanic dissolved REE. *Earth and Planetary Science Letters* 224 (3-4), 477–492.

Bayon G., German C.R., Nesbitt R.W., Bertrand P., and Schneider R.R. (2003). Increased input of circumpolar deep water-borne detritus to the glacial SE Atlantic Ocean. *Geochemistry Geophysics Geosystems* 4 (3), 1025, doi:10.1029/2002GC000371.

Benson L., Barber D., Andrews J.T., Taylor H., and Lamothe P. (2003). Rare-earth elements and Nd and Pb isotopes as source indicators for Labrador Sea clay-size sediments during Heinrich event 2. *Quaternary Science Reviews* 22, 881–889.

Berner H. and Wefer G. (1994). Clay-mineral flux in the Fram Strait and Norwegian Sea. *Marine Geology* 116, 327–345.

Bianchi G.G. and McCave I.N. (1999). Holocene periodicity in North Atlantic climate and deep-ocean flow south of Iceland. *Nature* 397, 515–517.

Birgel D. and Hass H.C. (2004). Oceanic and atmospheric variations during the last deglaciation in the Fram Strait (Arctic Ocean): a coupled high-resolution organic-geochemical and sedimentological study. *Quaternary Science Reviews* 23, 29–47.

Biscaye P.E., Grousset F.E., Revel M., Van der Gaast S., Zielinski G.A., Vaars A., and Kukla G. (1997). Asian provenance of glacial dust (stage 2) in the Greenland Ice Sheet Project 2 Ice Core, Summit, Greenland. *Journal of Geophysical Research* 102 (C 12), 26765–26781.

Björck S., Walker M.J.C., Cwynar L.C., Johnsen S., Knudsen K.-L., Lowe J.J., Wohlfarth B., and Intimate Members (1998). An event stratigraphy for the Last Termination in the North Atlantic region based on the Greenland Ice-core record: a proposal by the INTIMATE group. *Journal of Quaternary Science* 13, 283–292.

Blackwell P.G., Buck C.E., and Reimer P.J. (2006). Important features of the new radiocarbon calibration curves. *Quaternary Science Reviews* 25, 408–413.

Broecker W.S. (1991). The great ocean conveyor. *Oceanography* 4, 79–89.

Burton K.W., Ling H.-F., and O'Nions R.K. (1997). Closure of the Central American Isthmus and its effect on deep-water formation in the North Atlantic. *Nature* 386, 382–385.

Burton K.W. and Vance D. (2000). Glacial–interglacial variations in the neodymium isotope composition of seawater in the Bay of Bengal recorded by planktonic foraminifera. *Earth and Planetary Science Letters* 176, 425–441.

Chao T.T. and Zhou L. (1983). Extraction techniques for selective dissolution of amorphous iron oxides from soils and sediments. *Soil Science Society of America Journal* 47 (2), 225–232.

Chester R. and Hughes M.J. (1967). A chemical technique for the separation of ferromanganese minerals, carbonate minerals and adsorbed trace elements for pelagic sediments. *Chemical Geology* 2, 249–262.

Cronin T.M. (1999). Principles of Paleoclimatology. Columbia University Press.

Dallmann W.K. (Ed.) (1999). Lithostratigraphic Lexicon of Svalbard. Norsk Polarinstitutt, Tromsø, Norway.

Darby D.A. (2003). Sources of sediment found in sea ice from the western Arctic Ocean, new insights into processes of entrainment and drift patterns. *Journal of Geophysical Research* 108 (C8), 3257, doi: 10.1029/2002JC001350.

De Bievre P.J. and Debus G.H. (1965). Optimal Conditions for Mass Spectrometric Quantitative Determinations by Isotope Dilution. *European Atomic Energy Community — EURATOM* Report EUR 2219.e.

DePaolo D.J. and Wasserburg G.J. (1976). Nd isotopic variations and petrogenetic models. *Geophysical Research Letters* 3, 249–252.

Dethleff D. (1995). Die Laptevsee – eine Schlüsselregion für den Fremdstoffeintrag in das arktische Meereis. Doctoral Thesis, Christian-Albrechts-Universität, Kiel, Germany.

Dickin A.P. (1995). *Radiogenic Isotope Geology*. Cambridge University Press.

Dokken T.M. and Hald M. (1996). Rapid climatic shifts during isotope stages 2–4 in the polar North Atlantic. *Geology* 27, 599–602.

Dowdeswell J.A., Elverhøi A., and Spielhagen R.F. (1998). Glacimarine sedimentary processes and facies on the Polar North Atlantic margins. *Quaternary Science Reviews* 17, 243–272.

Dubinin A.V. and Strekopytov S.V. (2001). Behavior of Rare Earth Elements during Leaching of the Oceanic Sediments. *Geochemistry International* 39 (7), 692–701.

Dulski P. (2001). Reference materials for geochemical studies: New analytical data by ICP-MS and critical discussion of reference values. *Geostandards Newsletter: The Journal of Geostandards and Geoanalysis* 25, 87–125.

Eicken H., Kolatschek J., Freitag J., Lindemann F., Kassens H., and Dimitrenko I. (2000). A key source area and constraints on entrainment for basin-scale sediment transport by Arctic sea ice. *Geophysical Research Letters* 27 (13), 1919–1922.

Eicken H., Reimnitz E., Alexandrov T., Martin T., Kassens H., and Viehoff T. (1997). Sea-ice export processes in the Laptev Sea and their importance for sediment export. *Continental Shelf Research* 17, 205–233.

Eisenhauer A., Meyer H., Rachold V., Tütken T., Wiegand B., Hansen B.T., Spielhagen R.F., Lindemann F., and Kassens H. (1999). Grain size separation and sediment mixing in Arctic ocean sediments: evidence from strontium isotope systematic. *Chemical Geology* 158, 173–188.

Elverhøi A., Andersen E.S., Dokken T., Hebbeln D., Spielhagen R.F., Svendsen J.I., Sørflaten M., Rørnes A., Hald M., and Forsberg C. (1995). The Growth and Decay of the Late Weichselian Ice Sheet in Western Svalbard and Adjacent Areas Based on Provenance Studies of Marine Sediments. *Quaternary Research* 44, 303–316.

Fairbanks R.G. (1989). A 17 000-year glacio-eustatic sea level record: influence of glacial melting rates on the Younger Dryas event and deep-ocean circulation. *Nature* 342, 637–642.

Fairbanks R.G., Mortlock R.A., Chiu T.-C., Cao L., Kaplan A., Guilderson T.P., Fairbanks T.W., Bloom A.L., Grootes P.M., and Nadeau M.-J. (2005). Radiocarbon calibration curve spanning 0 to 50,000 years BP based on paired ^{230}Th/ ^{234}U/ ^{238}U and ^{14}C dates on pristine corals. *Quaternary Science Reviews* 24, 1781–1796.

Farmer G.L. and Barber D. (2003). Provenance of Late Quaternary ice-proximal sediments in the North Atlantic: Nd, Sr and Pb isotopic evidence. *Earth and Planetary Science Letters* 209, 227–243.

Frank M., Whiteley N., Kasten S., and Hein J.R. (2002). North Atlantic DeepWater export to the Southern Ocean over the past 14 Myr: Evidence from Nd and Pb isotopes in ferromanganese crusts. *Paleoceanography* 17 (2), 10.1029/2000PA000606.

Fütterer D.K. (Ed.) (1992). ARCTIC '91: The expedition ARK-VIII/3 of RV Polarstern in 1991. *Reports on Polar Research* 107.

Goldstein S.J. and Jacobsen S.B. (1988). Nd and Sr isotopic systematics of river water suspended material: implications for crustal evolution. *Earth and Planetary Science Letters* 87, 249–265.

Goldstein S.L., O'Nions R.K., and Hamilton P.J. (1984). A Sm-Nd isotopic study of atmospheric dusts and particulates from major river systems. *Earth and Planetary Science Letters* 70, 221–236.

Govindaraju K. (1995). 1995 working values with confidence limits for twenty-six CRPG, ANRT, and IWG-GIT geostandards. *Geostandards Newsletter: The Journal of Geostandards and Geoanalysis* 19 (Special Issue), 32 pp.

Grantz A., Johnson L., and Sweeney J.F. (Eds.) (1990). The Arctic Ocean Region. The Geological Society of America.

Gromet L.P., Dymek R.F., Haskin L.A., and Korotev R.L. (1984). The North American shale composite: its compilation, major and trace element characteristics. *Geochimica et Cosmochimica Acta* 48, 2469–2482.

Grootes P.M., Stuiver M., White J.W.C., Johnson S., and Jouzel J. (1993). Comparison of oxygen isotope records from the GISP2 and GRIP Greenland ice cores. *Nature* 366, 552–554.

Grove J.M. (1988). The Little Ice Age. Methuen, London.

Hald M., Dokken T.M., and Mikalsen G. (2001). Abrupt climatic change during the last interglacial–glacial cycle in the polar North Atlantic. *Marine Geology* 176, 121–137.

Haley B.A. and Klinkhammer G.P. (2002). Development of a flowthrough system for cleaning and dissolving foraminiferal tests. *Chemical Geology* 185, 51–69.

Hall G.E.M., Vaive J.E., Beer R., and Hoashi M. (1996). Selective leaches revisited, with emphasis on the amorphous Fe oxyhydroxide phase extraction. *Journal of Geochemical Exploration* 56, 59–78.

Hannigan R. E. and Sholkovitz E.R. (2001). The development of middle rare earth element enrichment in freshwaters: weathering of phosphate minerals. *Chemical Geology* 175, 495–508.

Hass C. (2000). Grain size composition of sediment core PS2837-5, PANGAEA, data set #57519 (DOI registration in progress). *http://www.pangea.de/PangaVista*.

Hass H.C. (2002). A method to reduce the influence of ice-rafted debris on a grain size record from northern Fram Strait, Arctic Ocean. *Polar Research* 21 (2), 299–306.

Hawkesworth C.J. and Kemp A.I.S. (2006). Evolution of the continental crust. *Nature* 443, 811–817.

Hebbeln D. (2000). Flux of ice-rafted detritus from sea ice in the Fram Strait. *Deep-Sea Research II* 47, 1773–1790.

Hebbeln D. and Wefer G. (1997). Late Quaternary paleoceanography in the Fram Strait. *Paleoceanography* 12 (1), 65–78.

Hughen K., Lehman S., Southon J., Overpeck J., Marchal O., Herring C., and Turnbull J. (2004a). [14]C Activity and Global Carbon Cycle Changes over the Past 50,000 Years. *Science* 303, 202–207.

Hughen K.A., Baillie M.G.L., Bard E., Bayliss A., Beck J.W., Bertrand C., Blackwell P.G., Buck C.E., Burr G., Cutler K.B., Damon P.E., Edwards R.L., Fairbanks R.G., Friedrich M., Guilderson T.P., Kromer B., McCormac F.G., Manning S., Bronk Ramsey C., Reimer P.J., Reimer R.W., Remmele S., Southon J.R., Stuiver M., Talamo S., Taylor F.W., van der Pflicht J., and Weyhenmeyer C.E. (2004b). Marine04 marine radiocarbon age calibration, 0-26 cal kyr BP. *Radiocarbon* 46 (3), 1059–1086.

Jacobsen S.B. and Wasserburg G.J. (1980). Sm-Nd isotopic evolution of chondrites. *Earth and Planetary Science Letters* 50, 139–155.

Jochum K.P. and Jenner G. (1994). Trace element analysis of Geological Survey of Japan silicate reference materials: Comparison of SSMS with ICP-MS data and a critical discussion of compiled values. *Fresenius Journal of Analytical Chemistry* 350, 310–318.

Johannessen O.M. (1986). Brief overview of the physical oceanography. In Hurdle B.G. (Ed.), The Nordic Seas,. Springer, New York, 103–127.

Johnson G.L. (**1990**). Morphology and plate tectonics: The modern polar oceans. In Bleil U. and Thiede J., editors, *Geological History of the Polar Oceans* C308 11–28. NATO ASI Series Dordrecht/ Boston/ London (Kluwer Academic Press) (**1990**).

Jones E.P., Rudels B., and Anderson L.G. (1995). Deep waters of the Arctic Ocean: origins and circulation. *Deep Sea Research I* 42 (5), 737–760.

Knies J., Kleiber H.-P., Matthiessen J., Müller C., and Nowaczyk N. (2001). Marine ice-rafted debris records constrain maximum extent of Saalian and Weichselian ice-sheets along the northern Eurasian margin. *Global and Planetary Change* 31, 45–64.

Knies J., Nowaczyk N., Müller C., Vogt C., and Stein R. (2000). A multiproxy approach to reconstruct the environmental changes along the Eurasian continental margin over the last 150 000 years. *Marine Geology* 163, 317–344.

Krause G. and Schauer U. (Eds.) (2001). The Expeditions ARKTIS XVI/1 and ARKTIS XV/2 of the Research Vessel "Polarstern" in 2000. *Reports on Polar and Marine Research* 389.

Laberg J.S. and Vorren T.O. (1995). Late Weichselian submarine debris flow deposits on the Bear Island Trough Mouth Fan. *Marine Geology* 127, 45–72.

Laberg J.S. and Vorren T.O. (1996). The Middle and Late Pleistocene evolution of the Bear Island Trough Mouth Fan. *Global and Planetary Change* 12, 309–330.

Laberg J.S. and Vorren T.O. (2000). Flow behaviour of the submarine glacigenic debris flows on the Bear Island Trough Mouth Fan, western Barents Sea. *Sedimentology* 47, 1105–1117.

Lacan F. and Jeandel C. (2001). Tracing Papua New Guinea imprint on the central Equatorial Pacific Ocean using neodymium isotopic compositions and Rare Earth Element patterns. *Earth and Planetary Science Letters* 186, 497–512.

Lacan F. and Jeandel C. (2004). Denmark Strait water circulation traced by heterogeneity in neodymium isotopic compositions. *Deep-Sea Research I* 51, 71–82.

Lacan F. and Jeandel C. (2005). Neodymium isotopes as a new tool for quantifying exchange fluxes at the continent-ocean interface. *Earth and Planetary Science Letters* 232, 245–257.

Landvik J.Y., Bondevik S., Elverhøi A., Fjeldskaar W., J.Mangerud , Salvigsen O., Siegert M.J., Svendsen J.I., and Vorren T.O. (1998). The Last Glacial Maximum of Svalbard and the Barents Sea area: ice sheet extent and configuration. *Quaternary Science Reviews* 17, 43–75.

Laskar J. (1990). The chaotic motion of the solar system: a numerical estimate of the size of the chaotic zones. *Icarus* 88, 266–291.

Lemke P. (Ed.) (2003). The Expedition ARKTIS XVIII/1 a, b of the Research Vessel "Polarstern" in 2002. *Reports on Polar and Marine Research* 446.

Levitan M.A., Musatov E.E., and Burtman M.V. (2002a). History of Sedimentation on the Yermak Plateau during the Recent 190 ka: Communication 1. Lithology and Mineralogy of Middle Pleistocene–Holocene Sediments. *Lithology and Mineral Resources* 37 (6), 481–492.

Levitan M.A., Musatov E.E., and Burtman M.V. (2002b). History of Sedimentation on the Yermak Plateau during the Recent 190 ka: Communication 2. Paleoceanographic Interpretation. *Lithology and Mineral Resources* 37 (6), 493–502.

Lloyd J.M., Kroon D., Boulton G.S., Laban C., and Fallick A. (1996). Ice rafting history from the Spitsbergen ice cap over the last 200 kyr. *Marine Geology* 131, 103–121.

Mangerud J., Dokken T., Hebbeln D., Heggen B., Ingólfsson Ó., Landvik J.Y., Mejdahl V., Svendsen J.I., and Vorren T.O. (1998). Fluctuations of the Svalbard–Barents Sea Ice Sheet during the last 150 000 years. *Quaternary Science Reviews* 17, 11–42.

Mangerud J., Larsen E., Longva O., and Sønstegaard E. (1979). Glacial history of western Norway 15,000–10,000 B.P. *Boreas* 8, 179–187.

Martinson D.G., Pisias N.G., Hays N.D., Imbrie J., Moore T.C., and Shackleton N.J. (1987). Age dating and the orbital theory of the ice ages: development of a high-resolution 0 to 300,000 year chronostratigraphy. *Quaternary Research* 27, 1–29.

Matthes F.E. (1939). Report of Committee on Glaciers, April 1939. *Transactions American Geophysical Union* 20, 518–523.

McCave I.N., Manighetti B., and Beveridge N.A.S. (1995a). Circulation in the glacial North Atlantic inferred from grain-size measurements. *Nature* 374, 149–152.

McCave I.N., Manighetti B., and Robinson S.G. (1995b). Sortable silt and fine sediment size/composition slicing: Parameters for paleocurrent speed and paleoceanography. *Paleoceanography* 10 (3), 593–610.

McLennan S.M. (1989). Rare earth elements in sedimentary rocks: influence of provenance and sedimentary processes. In Lipin B.R. and McCay G.A. (Eds.), Geochemistry and mineralogy of rare earth elements. *Reviews in Mineralogy* 21, 169–200.

Mørk M.B.E. (1999). Compositional Variations and Provenance of Triassic Sandstones From the Barents Shelf. *Journal of Sedimentary Research* 69 (3), 690–710.

Nance W.B. and Taylor S.R. (1976). Rare earth patterns and crustal evolution - I. Australian post-Archean sedimentary rocks. *Geochimica et Cosmochimica Acta* 40, 1539–1551.

Nørgaard-Pedersen N. (2002). Age model of sediment core PS2837-5, PANGAEA, doi:10.1594/PANGAEA.66867. *http://www.pangea.de/PangaVista*.

Nørgaard-Pedersen N., Spielhagen R.F., Erlenkeuser H., Grootes P.M., Heinemeier J., and Knies J. (2003). Arctic Ocean during the Last Glacial Maximum: Atlantic and polar domains of surface water mass distribution and ice cover. *Paleoceanography* 18 (3), 1063, doi: 10.1029/2002PA000781.

Nørgaard-Pedersen N., Spielhagen R.F., Thiede J., and Kassens H. (1998). Central Arctic surface ocean environment during the past 80 000 years. *Paleoceanography* 13, 193–204.

Nürnberg D., Wollenburg I., Dethleff D., Eicken H., Kassens H., Letzig T., Reimnitz E., and Thiede J. (1994). Sediments in Arctic sea ice: implications for entrainment, transport, and release. *Marine Geology* 104, 185–214.

O'Nions R.K., Carter S.R., Cohen R.S., Evensen N.M., and Hamilton P.J. (1978). Pb, Nd, and Sr isotopes in oceanic ferromanganese deposits and ocean floor basalts. *Nature* 273, 435–438.

Palmer M.R. (1985). Rare earth elements in foraminifera. *Earth and Planetary Science Letters* 73, 285–298.

Pfirman S., Wollenburg I., Thiede J., and Lange M.A. (1989). Lithogenic sediment on Arctic pack ice: potential aeolian flux and contributions to deep sea sediments. In Sarnthein M. and Leinen M. (Eds.), Paleoclimatology and Paleometeorology: Modern and Past Pattern of Global Atmospheric Transport, pp. 463–493. Kluwer Academic Publishers, Dordrecht.

Pfirman S.L., Colony R., Nürnberg D., Eicken H., and Rigor I. (1997). Reconstructing the origin and trajectory of drifting Arctic sea ice. *Journal of Geophysical Research* 102, 12 575–12 586.

Phillips R.L. and Grantz A. (2001). Regional variations in provenance and abundance of ice-rafted clasts in Arctic Ocean sediments: implications for the configuration of late Quaternary oceanic and atmospheric circulation in the Arctic. *Marine Geology* 172, 91–115.

Piotrowski A., Goldstein S.L., Hemming S.R., and Fairbanks R.G. (2004). Intensification and variability of ocean thermohaline circulation through the last deglaciation. *Earth and Planetary Science Letters* 225, 205–220.

Pirrung M., Fütterer D., Grobe H., Matthiessen J., and Niessen F. (2002). Magnetic susceptibility and ice-rafted debris in surface sediments of the Nordic Seas: implications for Isotope Stage 3 oscillations. *Geo-Marine Letters* 22, 1–11.

Polyak L. and Mikhailov V. (1996). Post-glacial environments of the southeastern Barents Sea: foraminiferal evidence. In Andrews J.T., Austin W.E.N., Bergsten H., and Jennings A.E. (Eds.), Late Quaternary Palaeoceanography of the North Atlantic Margins. *Geological Society Special Publication* No. 111, 323–339.

Rachold V., Hermel J., and Korotaev V.N. (1995). Expedition to the Lena River in July/August 1994. In Kassens H. (Ed.), Laptev Sea System: Expeditions in 1994. *Reports on Polar Research* 182, 181–195.

Raczek I., Jochum K.P., and Hofmann A.W. (2003). Neodymium and Strontium Isotope Data for USGS Reference Materials BCR-1,BCR-2, BHVO-1, BHVO-2, AGV-1, AGV-2, GSP-1, GSP-2 and Eight MPI-DING Reference Glasses. *Geostandards Newsletter* 27 (2), 173–179.

Raczek I., Stoll B., Hofmann A.W., and Jochum K.P. (2001). High-Precision trace element data for the USGS reference materials BCR-1, BCR-2, BHVO-1, BHVO-2, AGV-1, AGV-2, DTS-1, DTS-2, GSP-1, and GSP-2 by ID-TIMS and MIC-SSMS. *Geostandards Newsletter* 25 (1), 77–86.

Rahmstorf S. (2002). Ocean circulation and climate during the past 120,000 years. *Nature* 419, 207–214.

Reimnitz E., Dethleff D., and Nürnberg D. (1994). Contrasts in Arctic shelf sea-ice regimes and some implications: Beaufort Sea versus Laptev Sea. *Marine Geology* 119, 215–225.

Renssen H., Goose H., Fichefet T., and Campin J.-M. (2001). The 8.2 kyr BP event simulated by a global atmosphere-sea-ice-ocean model. *Geophysical Research Letters* 28, 1567–1570.

Renssen H. and Isarin R.F.B. (2001). The two major warming phases of the last deglaciation at ∼14.7 and 11.5 ka cal BP in Europe: climate reconstructions and AGCM experiments. *Global and Planetary Change* 30, 117–153.

Revel M., Sinko J.A., and Grousset F.E. (1996). Sr and Nd isotopes as tracers of North Atlantic lithic particles: Paleoclimatic implications. *Paleoceanography* 11 (1), 95–113.

Richard P., Shimizu N., and Allegre C.J. (1976). ^{143}Nd/^{146}Nd, a natural tracer: an application to oceanic basalts. *Earth and Planetary Science Letters* 31, 269–278.

Rigor I. (1992). Arctic Ocean buoy program. *Argos Newsletter* 44, 1–3.

Roddick J.C., Sullivan R.W., and Dudás F.Ö. (1992). Precise calibration of tracer compositions for Sm-Nd isotopic studies. In: Radiogenic Age and Isotopic Studies: Report 5. *Geological Survey of Canada, Paper* 91-2, 191–200.

Rudels B., Friedrich H.J., and Quadfasel D. (1999). The Arctic Circumpolar Boundary Current. *Deep-Sea Research II* 46, 1023–1062.

Rudels B., Jones E.P., Anderson L.G., and Kattner G. (1994). On the intermediate depth waters of the Arctic Ocean. In Johannessen O.M., Muench R.D., and Overland J.E. (Eds.), The Polar Oceans and their Role in Shaping the Global Environment: The Nansen Centennial Volume. American Geophysical Union. *Geophysical Monograph* 85, 33–46.

Rutberg R.L. (2000). The Application of Sr and Nd Radiogenic Isotopes to South Atlantic Paleoceanography. PhD Thesis, Columbia University, New York, New York, USA.

Rutberg R.L., Hemming S.R., and Goldstein S.L. (2000). Reduced North Atlantic Deep Water flux to the glacial Southern Ocean inferred from neodymium isotope ratios. *Nature* 405, 935–938.

Sarnthein M., Gersonde R., Niebler S., Pflaumann U., Spielhagen R.F., Thiede J., Wefer G., and Weinelt W. (2003). Overview of Glacial Atlantic Ocean Mapping (GLAMAP 2000). *Paleoceanography* 18 (2), 1030, doi:10.1029/2002PA000769.

Schlichtholz P. and Houssais M.N. (1999). An inverse modeling study in Fram Strait. Part I: dynamics and circulation. *Deep-Sea Research II* 46, 1083–1135.

Sharma M., Basu-Asish R., and Nesterenko G.V. (1992). Temporal Sr-, Nd-, and Pb-isotopic variations in the Siberian flood basalts, implications for the plume-source characteristics. *Earth and Planetary Science Letters* 113, 365–381.

Sholkovitz E.R. (1990). Rare-earth elements in marine sediments and geochemical standards. *Chemical Geology* 88, 333–347.

Sholkowitz E.R., Landing W.M., and Lewis B.L. (1994). Ocean particle chemistry: the fractionation of rare earth elements between suspended particles and seawater. *Geochimica et Cosmochimica Acta* 58, 1567–1579.

Siegert M.J. and Dowdeswell J.A. (2002). Late Weichselian iceberg, surface-melt and sediment production from the Eurasian Ice Sheet: results from numerical ice-sheet modelling. *Marine Geology* 188, 109–127.

Spielhagen R.F. (1991). Die Eisdrift in der Framstraße während der letzten 200.000 Jahre. *GEOMAR Report* 4.

Spielhagen R.F., Baumann K.H., Erlenkeuser H., Nowaczyk N.R., Nørgaard-Pedersen N., Vogt C., and Weiel D. (2004). Arctic Ocean deep-sea record of northern Eurasian ice sheet history. *Quaternary Science Reviews* 23, 1455–1483.

Stein R. and Fahl K. (Eds.) (1997). Scientific Cruise Report of the Arctic Expedition ARK-XIII/2 of RV "Polarstern" in 1997. *Reports on Polar Research* 255.

Stein R. and Stepanets O. (Eds.) (2001). The German-Russian project on Siberian river run-off (SIRRO): scientific cruise report of the Kara-Sea expedition "SIRRO 2000" of RV "AkademikBoris Petrov" and first results. *Reports on Polar and Marine Research* 393.

Stein R. and Stepanets O. (Eds.) (2002). Scientific cruise report of the Kara-Sea expedition 2001 of RV "Akademik Boris Petrov": the German-Russian project on Siberian river run-off (SIRRO) and the EU project "ESTABLISH". *Reports on Polar and Marine Research* 419.

Stuiver M. and Reimer P.J. (1993). Extended ^{14}C database and revised CALIB radiocarbon calibration program. *Radiocarbon* 35, 215–230.

Stuiver M., Reimer P.J., Bard E., Beck J.W., Burr G.S., Hughen K.A., Kromer B., McCormac G., van der Pflicht J., and Spurk M. (1998). INTCAL 98 Radiocarbon age calibration, 24,000-0 cal BP. *Radiocarbon* 40, 1041–1083.

Svendsen J.I., Alexanderson H., Astakhov V.I., Demidov I., Dowdeswell J.A., Funder S., Gataullin V., Henriksen M., Houmark-Nielsen C. Hjortand M., Hubberten H.W., In-gólfsson Ó., Kjær M. Jakobssonand K.H., Larsen E., Lokrantz H., Lunkka J.P., Mangerud A. Lysåand J., Matiouchkov A., Murray A., Möller P., Nikolskaya F. Niessenand O., Polyak L., Saarnisto M., Siegert C., M.J.Siegert , Spielhagen R.F., and Stein R. (2004). Late Quaternary ice sheet history of northern Eurasia. *Quaternary Science Reviews* 23 (11–13), 1229–1271.

Tachikawa K., Athias V., and Jeandel C. (2003). Neodymium budget in the modern ocean and paleoceanographic implications. *Journal of Geophysical Research* 108 (C8), 3254, doi:10.1029/1999JC000285.

Tessier A., Campbell P.G.C., and Bisson M. (1979). Sequential extraction procedure for the speciation of particulate trace metals. *Analytical Chemistry* 51, 845–851.

Thorndike A.F. (1986). Kinematics of sea ice. In: Untersteiner N. (Ed.), Geophysics of sea ice. NATO ASI Series B, Vol. 146, pp. 489–550. Plenum Press, New York.

Tütken T., Eisenhauer A., Wiegand B., and Hansen B.T. (2002). Glacial–interglacial cycles in Sr and Nd isotopic composition of Arctic marine sediments triggered by the Svalbard/Barents Sea ice sheet. *Marine Geology* 182, 351–372.

Vance D. and Burton K. (1999). Neodymium isotopes in planktonic foraminifera: a record of the response of continental weathering and ocean circulation rates to climate change. *Earth and Planetary Science Letters* 173, 365–379.

Vinje T., Nordlund N., and Kvambekk Å. (1998). Monitoring ice thickness in Fram Strait. *Journal of Geophysical Research* 103 (C 5), 10437–10449.

Voelker A.H.L., Sarnthein M., Grootes P. M., Erlenkeuser H., Laj C., Mazaud A., Nadeau M.-J., and Schleicher M. (1998). Correlation of marine ^{14}C ages from the Nordic Seas

with the GISP2 isotope record: Implications for ^{14}C calibration beyond 25 ka BP. *Radiocarbon* 40 (1), 517–534.

Vogelsang E. and Sarnthein M. (2003). Age control of sediment core PS2837-5, PANGAEA, doi:10.1594/PANGAEA.104834. *http://www.pangea.de/PangaVista*.

Vogt C. (1997). Regional and temporal variations of mineral assemblages in Arctic Ocean sediments as climatic indicator during glacial/interglacial changes. *Reports on Polar Research* 251.

Vogt C., Knies J., Spielhagen R.F., and Stein R. (2001). Detailed mineralogical evidence for two nearly identical glacial/interglacial cycles and Atlantic water advection to the Arctic Ocean during the last 90,000 years. *Global and Planetary Change* 31, 23–44.

Vorren T.O., Hald M., and Lebesbye E. (1988). Late Cenozoic environment in the Barents Sea. *Paleoceanography* 3, 601–612.

Weaver A.J., Saenko O.A., Clark P.U., and Mitrovica J.X. (2003). Meltwater Pulse 1A from Antarctica as a Trigger of the Bølling-Allerød Warm Interval. *Science* 299, 1709–1713.

Weldeab S., Emeis K.-C., Hemleben C., Vennemann T.W., and Schulz H. (2002). Sr and Nd isotope composition of Late Pleistocene sapropels and nonsapropelic sediments from the Eastern Mediterranean Sea: Implications for detrital influx and climatic conditions in the source areas. *Geochimica et Cosmochimica Acta* 66, 3585–3598.

Winter B.L., Johnson C.L., and Clark D.L. (1997). Geochemical constraints on the formation of Late Cenozoic ferromanganese micronodules from the central Arctic Ocean. *Marine Geology* 138, 149–169.

Wollenburg I. (1993). Sediment transport by Arctic Sea Ice: the recent load of lithogenic and biogenic material. *Reports on Polar Research* 127.

Wollenburg J.E., Knies J., and Mackensen A. (2004). High-resolution paleoproductivity fluctuations during the past 24 kyr as indicated by benthic foraminifera in the marginal Arctic Ocean. *Palaeogeography, Palaeoclimatology, Palaeoecology* 204, 209–238.

Wooden J.L., Czamanske G.K., Fedorenko V.A., Arndt N.T., Chauvel C., Bouse R.M., King B.S.W., Knight R.J., and Siems D.F. (1993). Isotopic and trace-element constraints on mantle and crustal contributions to Siberian continental flood basalts, Noril'sk area, Siberia. *Geochimica et Cosmochimica Acta* 57, 3677–3704.

Additional sources

Bryson B. (2002). *Troublesome Words.* 3rd edition. Penguin Books Ltd, London.

Strunk Jr. W. and White E.B. (1999). *The Elements of Style.* 4th edition. Longman Publishers.

The New Oxford Dictionary of English (2001). Corrected edition. Oxford University Press.

A

C   V

Persönliche Daten:

Wolfgang Schmitt, *28.06.1973 in München, wohnhaft in München Maxvorstadt

Mutter Doris Schmitt, geb. Hartmann, *11.05.1941, Diplomübersetzerin

Vater Ulrich Schmitt, *20.11.1938, † 07.05.1990, Elektroingenieur

Bruder Reiner Schmitt, *13.05.1971, Studienrat

Schulbildung:

1979-1983	Besuch der Grundschule an der Forellenstraße, München
1983-1992	Besuch des Michaeli-Gymnasiums, München
Juli 1992	Erwerb der allgemeinen Hochschulreife

Weiterer Werdegang:

Okt. 1992 – Dez. 1993	Zivildienst in der Sozialstation Berg am Laim, München
Okt. 1993 – Sept. 1994	Diplomstudiengang Mathematik an der Ludwig-Maximilians-Universität München
Sept. 1994 – Juni 1995	Berufsausbildung zum Maschinenbaumechaniker bei Fa. Retco Maschinenbau, Aschheim bei München
Okt. 1995 – März 2002	Diplomstudiengang Geologie/Paläontologie an der Ludwig-Maximilians-Universität München
Dez. 2001	Erwerb des Diploms in Geologie/Paläontologie
März 2002 – Mai 2004	Wissenschaftlicher Angestellter am Department für Geo- und Umweltwissenschaften, Sektion Mineralogie, Petrologie und Geochemie, der Ludwig-Maximilians-Universität München
April 2002 – Sept. 2004	Promotionsstudiengang Geologie an der Ludwig-Maximilians-Universität München